Order Number 9410179

Dependence of the ionospheric convection pattern on the conductivity and the southward IMF

Shue, Jih-Hong, Ph.D.

University of Alaska Fairbanks, 1993

U·M·I
300 N. Zeeb Rd.
Ann Arbor, MI 48106

DEPENDENCE OF THE IONOSPHERIC CONVECTION PATTERN ON THE CONDUCTIVITY AND THE SOUTHWARD IMF

A

THESIS

Presented to the Faculty of the University of Alaska Fairbanks
in Partial Fulfillment of the Requirements
for the Degree of

DOCTOR OF PHILOSOPHY

By

Jih-Hong Shue, B.S., M.S.

Fairbanks, Alaska

September 1993

DEPENDENCE OF THE IONOSPHERIC CONVECTION PATTERN ON THE CONDUCTIVITY AND THE SOUTHWARD IMF

By

Jih-Hong Shue

RECOMMENDED:

Prof. S.-I. Akasofu

Prof. N. N. Biswas

Prof. M. H. Rees

Prof. D. R. Weimer

Prof. J. R. Kan, Chairman, Advisory Committee

Prof. J. L. Morack, Head, Physics Department

APPROVED:

J. L. Morack, Interim Dean, College of Natural Sciences

E. Murphy, Chancellor's Faculty Assoc., Graduate Studies

7/28/93

Date

ABSTRACT

Electric field measurements from the DE-2 satellite were used to determine the location of the convection reversal boundary and the potential around this boundary under a combination of interplanetary magnetic field (IMF) and auroral electrojet conditions. The electric potential is obtained by the integration of the electric fields. The convection reversal boundary is defined in this study as where the potential has its absolute maximum and minimum values. The data were sorted into 18 categories according to two levels of the negative IMF B_z, three ranges of IMF B_y, and two substorm phases. The data were fit with both continuous and discontinuous boundaries to get a functional representation of boundary potentials and locations.

A simple model is constructed by solving the Laplace's equation in order to illustrate the obtained boundary potentials and locations. The results show that the enhanced electric field in the midnight sector is associated with an intense westward electrojet current. It can also be seen that the convection reversal boundary is found to be discontinuous near midnight. The discontinuous convection reversal boundary on the dayside is related to the merging near dayside cusp region. The discontinuous convection reversal boundary on the nightside is related to the conductivity enhancement. The intrusion of the dawn cell into the dusk cell is due to nonuniformity of the Hall conductivity in the ionosphere.

Another model is constructed by solving the current continuity equation with field-aligned current and nonuniform conductivity added. It can be found that a secondary convection reversal, which is detached from the dusk-cell convection reversal, appears in the evening-midnight sector within the polar cap when the IMF B_y is positive and the conductivity is nonuniform. This convection reversal is attributed to be created by the $\mathbf{B} \times \mathbf{V}$ dynamo. Also, the inclusion of the region 2 field-aligned current leads to an enhancement of the electric field in the region between the region 1 and region 2 currents.

TABLE OF CONTENTS

LIST OF FIGURES

LIST OF TABLES

ACKNOWLEDGMENTS

I would like to first express my special thanks to Prof. Joseph R. Kan, chairman of my advisory committee, for his continuing advise, support, and encouragement. He has pointed me in a right direction during the completion of the thesis. I learned a lot from him. Another special thanks go to Prof. Daniel R. Weimer for his continuing discussion, support, and patience. I also learned a lot from him.

Deep thanks go to the members of my advisory committee; Profs. Syun-I. Akasofu, Nirendra N. Biswas, and Manfred H. Rees, for their suggestions and reviews of my thesis. Also, I would like to thank all my friends and colleagues; Zhiwei Ma, Qilong Min, Baolian Xu, and Wei Sun, for their help. In particular, Ms. Jeanne Hume deserves special thanks for helping me improve the english.

This work was supported by NSF grant ATM90-14148 under the Atmospheric Science Section. I thank Prof. Nelson Maynard for providing the DE-2 VEFI data. I am grateful for the use of the IMP-8 magnetometer data provided by principal investigator Ronald Lepping. These data were supplied on magnetic tape by the NASA National Space Science Data Center. The *AE* index is compiled and distributed by the World Data Center C2 for geomagnetism at Kyoto University.

CHAPTER 1

Introduction

This thesis is divided into six chapters. Chapter 1 introduces the background and motivation of the thesis, including the overview of the ionospheric convection, the review of the previous models, and the objective of the thesis. Chapter 2 introduces the DE-2 mission and Vector Electric Field Instrument (VEFI) measurement, and shows how to obtain the potential and location of the convection reversal boundary from each VEFI measurement. Normalization of the potential measurements, using the AU index, is discussed. Chapter 3 deals with the sorting of the VEFI measurements and the observational determination of the boundary potentials and locations. The other two data sets; interplanetary magnetic field (IMF) from IMP-8 or ISEE-3 satellites and geomagnetic indices (AL and AU), have been used to group the DE-2 VEFI measurements under various combinations of the IMF and geomagnetic activity. Fourier series were used to fit the data points to periodic functions. Chapter 4 shows the reproduction of the ionospheric convection patterns. A simple model for only solving the Laplace equation is used to illustrate the fitting boundary potentials and locations. Another model for solving inhomogeneous current continuity equation is also introduced. The results in Chapter 3 were used as the boundary conditions of the model. The resulting convection patterns were shown at the end of this chapter. Chapter 5 is the discussion of the resulting convection patterns and the comparison with the other models. Finally, the conclusion is developed in Chapter 6.

1.1 Overview of the Ionospheric Connection

The coupling between the solar wind, magnetosphere and ionosphere is an important subject in the field of solar-terrestrial physics. The physics of the interaction process are complicated. The solar wind carrying the interplanetary magnetic field flows in the interplanetary space and impinges on the earth's dipole magnetic field. *Dungey* [1961] postulated an open magnetosphere in which the southward IMF reconnected with the earth's dipole magnetic field. Part of the solar wind energy directly transmits into the ionosphere along the open flux tubes. The other parts of solar wind energy are stored in the magnetotail and start releasing into the ionosphere at the onset of substorms. The ionospheric convection on the dayside mainly responds to IMF on a time scale of about 10-20 minutes. The ionospheric convection on the nightside is less directly related with the IMF, which has a 30-60 minute time lag after the IMF turns southward. The ionospheric convection is changed in response to these two kinds of energy inputs. The other "viscous-like" interaction, which occurs at the lower latitude boundary layer and transfers the momentum from the magnetosheath, also have the effect on the ionospheric convection. But the voltage generated by this interaction is small in comparison with the voltage generated by the dayside and nightside reconnection.

The ionospheric convection for the southward IMF is mainly anti-sunward in the polar cap and the flow is returned sunward at lower latitudes on both dawn and dusk sides. We call this a "two-cell" convection pattern. The regions of sunward and anti-sunward are separated by well-defined convection reversals near dawn and dusk. The anti-sunward flow is constricted to a narrow region on the dayside which was called a "throat" by *Reiff et al.* [1978]. The flow also appears to be constricted in another narrow region at midnight, near the poleward side of the Harang discontinuity.

The DE-2 satellite has provided a large number of electric field measurements at all local times. Each electric field measurement represents a signature of some portion of the ionospheric convection. These measurements show that the ionospheric convection is highly dependent on IMF, auroral electrojet, and ionospheric conductivity. The relationships among the southward IMF, the auroral electrojet, the ionospheric conductivity, and the ionospheric convection will be discussed separately in the following subsections.

1.1.1 Relationship Between Southward IMF and Ionospheric Convection

Many observations have indicated that IMF controls the ionospheric convection. The relationship between ionospheric convection and IMF has been studied by *Heppner* [1977], *Foster* [1983], *Clauer et al* [1984], *Foster* [1984], *Reiff and Burch* [1985], *de la Beaujardière et al.* [1985], *Foster et al.* [1986], *Holt et al.* [1987], *Heppner and Maynard* [1987], and *Lu et al.* [1989]. They used a large number of satellite measurements or radar scans and have shown that two-cell convection is associated with southward IMF and the orientation of the convection appears to be directly related to the variation of IMF. The IMF B_y has opposite effects in the northern and southern hemispheres. The convection patterns are the same for the northern hemisphere with a positive B_y as for the southern hemisphere with a negative B_y. Geometry of the convection pattern is usually characterized by one small cell and one large cell. The large cell is almost circular and the small cell is crescent-shaped. The dawn cell is generally thought to be larger than the dusk cell when $B_y < 0$. When B_y is very small, these two cells are located approximately either side of noon-midnight meridian, which are equal in size. The feature of eastward/westward flow can be seen on the dayside, which is associated with negative/positive IMF B_y. This can be interpreted as a direct coupling between the solar wind and dayside ionosphere [*Clauer et al.*, 1984]. *Reiff and Burch* [1985] propose a

qualitative model to generalize the B_y effect on ionospheric convection. Their model is based on the antiparallel merging hypothesis of *Crooker* [1979]. Locations of the merging region are different with B_y direction. The merging associated electric field can drive a eastward or a westward flow on the dayside.

The polar cap potential and size become larger when the B_z component gets larger. Several relationships between the solar wind and polar cap potential have been studied by the observational data [*Reiff et al.*, 1981; *Doyle and Burch*, 1983; *Wygant et al.*, 1983; *Reiff and Luhmann*, 1986; *Bargatze et al.*, 1986]. They used various combinations of the solar wind parameters (solar wind velocity and interplanetary magnetic field). They have tested different coupling functions and have shown that the polar cap potential is proportional to the combination of southward B_z and solar wind velocity. The interpretation is that the larger southward B_z and solar wind velocity increase the merging rate, then generate more electric fields mapped down to the ionosphere. *Siscoe and Huang* [1985] used an ideal model and stated that dayside and nightside merging maintains long-term flux of the polar cap. They have shown that the polar cap inflates in response to increasing dayside merging during the southward IMF and deflates when the merging in the tail exceeds the dayside merging. *Meng and Makita* [1986] used averaged electron precipitation data to determine the size of the polar cap and found that the polar cap size varies with the IMF and substorm activity. The polar cap area is increasing when IMF is southward. The polar cap size is decreasing when the substorm activity begins to subside. *Frank and Craven* [1988] used the imaging data of auroral oval and indicated that the polar cap area was found to expand when IMF turns southward and contracts after the onset of substorm. *Lockwood et al.* [1990] further concluded that the flow driven by the dayside merging is associated with the expanding polar cap. A larger southward B_z increases the dayside merging flux, and the polar cap size gets bigger.

1.1.2 Relationship Between Auroral Electrojet and Ionospheric Convection

The ionospheric convection is not only influenced by the IMF directly, but also by the reconnection in the tail. *Lockwood et al.* [1990] concluded that the ionospheric electric field cannot generally be regarded as a simple mapping of the solar wind electric field along open magnetic flux tubes. It must be the sum of the dayside merging and nightside reconnection, which generates voltage gaps on the polar cap boundary. The dayside merging generates a potential gap on the dayside, which drives the convection of plasma into the polar cap region. Similarly, the nightside reconnection generates a potential gap near midnight, which drives the plasma out of the polar cap region.

The difference between the cases with and without substorms is near the location of Harang discontinuity, which is defined as the boundary between eastward and westward electrojets or, as the boundary between the region of southward and northward electric field [*Maynard*, 1974]. The intensity of westward electrojet is enhanced as substorms occur. The electrojet current system can be divided into two classifications according to the signatures which are obtained with a series of magnetometer measurements. These two classifications are commonly denoted as DP 1 and DP 2 systems. DP 2 system increases and decreases slowly during an isolated substorm, with two electrojets centered in the morning and evening sectors. DP 1 system increases suddenly at the onset of the expansion phase, with a dominant electrojet centered near midnight [*Clauer and Kamide*, 1985]. Another feature of substorms is that the westward electrojet intrudes deeply into the premidnight sector during the substorms [*Kamide*, 1991] and a westward electric field is generated [*Lockwood et al.*, 1990].

The magnetic configuration becomes dipolarized when substorms occur. Substorms can be used to remove the magnetic flux from the polar cap, causing the decrease of polar cap size [*Siscoe*, 1982]. The relationship between polar cap potential, size, and substorms have been

studied by *Bargatze et al.* [1985], *Weimer et al.* [1990a], *Siscoe*, [1991], and *Weimer et al.* [1992]. They have shown that the polar cap potential and size are associated with substorm activity. *Weimer et al.* [1990a] have shown that the westward and eastward electrojet are roughly proportional to the dawn and dusk cell potentials, and substorms occur only when the polar cap potential exceeds a threshold of approximately 60 kV. *Weimer et al.* [1992] studied the polar cap size and potential during substorms. They have shown that the polar cap potential starts to increase at 1.5 hours before onset and starts to decline at 1.5 hours after onset, and the size of polar cap also decreases at the time of onset.

1.1.3 Relationship Between Conductivity and Ionospheric Convection

Several sources can cause an increase in conductivity: solar illumination, upward field-aligned current, and precipitating particles [*Strobel et al.*, 1980; *Vickrey et al.*, 1981; *Wallis and Budzinski*, 1981; *Robinson and Vondrak*, 1984; *Robinson et al.*, 1985; *Fuller-Rowell and Evans*, 1987; *Hardy et al.*, 1987; *Rasmussen et al.*, 1988]. *Smiddy et al.* [1980] found that the ionospheric conductivity is high in the auroral zones and sunlit polar cap. The effect of low and high energy precipitating electrons also plays an important role on conductivity when the ionosphere is not sunlit [*Robinson and Vondrak*, 1984]. *Newell and Meng* [1988] have shown the ion/electron energy flux is larger in the summer hemisphere than that in the winter hemisphere.

The ionospheric convection is mainly driven by the electric fields from the solar wind and the magnetosphere, which is transmitted along highly conducting magnetic field lines. The ionospheric conductivity change in space can result in the divergence of the current. The polarization charges are created and the polarization electric fields build up very quickly, and then change the electric field pattern. [*Moses et al.*, 1987; *Kan et al.*, 1988; *Marklund et*

al., 1988; *Blomberg and Marklund*, 1988]. *de la Beaujardière et al.* [1991a,1991b] binned and averaged the data of Sondrestrom incoherent scatter radar to study the seasonal effect of convection electric fields. It was found that the large-scale convection significantly changes with seasons. The changes include the overall shape of the convection pattern, the electric field intensity, and the total dawn-dusk potential across the polar cap. *Weimer et al.* [1992] have shown that AE/Φ_{pc} ratio is nearly constant before and after substorms, but decreases slightly during the substorm growth phase and increases greatly during the expansion phase. These increases are most likely due to a higher conductivity and westward electric field within the electrojet during the expansion, which causes the AE to increase without a corresponding change in the polar cap potential.

Precipitation from the inner edge of the plasma sheet creates a density maximum in the auroral oval, which leads to Hall and Pedersen conductivity maximum [*Coroniti and Kennel*, 1972]. This conductivity maximum may cause the polar cap electric field to rotate clockwise [*Nopper and Carovillano*, 1979; *Yasuhara et al.*, 1983], and distortion of convection pattern [*Kan and Kamide*, 1985; *Kan et al.*, 1988].

1.2 Review of Previous Models

Various ionospheric convection models have been presented. Some models have been deduced from observation, others are derived mathematically. *Heelis et al.* [1982] constructed a purely mathematical expression that allows the large-scale global convection characteristics in the ionosphere to be reproduced. This model has a circular convection reversal boundary which is equipotential except on the convergent zones on the dayside and nightside. The variables in this expression are the dayside "throat" and nightside Harang discontinuity. *Hairston and*

Heelis [1990] used DE-2 measurements of ion drift which lie within 3 hours MLT of dawn-dusk line to model high-latitude ionospheric convection in relation to the IMF. This model has removed the assumptions of *Heelis et al.* [1982], allowing an asymmetric distribution of potential within the polar cap. The parameters describing the asymmetry of convection are the location and magnitude of potential maxima and minima, and the location of zero-potential line. *Sojka et al.* [1986] also developed a mathematical model which is a derivative of the model of *Heelis et al.* [1982], but included a K_p dependence.

Heppner and Maynard [1987] empirically studied the electric field measurements from the DE-2 satellite in all the magnetic local time zones. Their objective was to attempt to represent highly variable global distribution with a minimum of characteristic distribution. The passes were grouped according to the orientation of the IMF, but only one range of K_p value ($3^+ \leq K_p \leq 4^-$). Their model has shown that the convection pattern is strongly dependent on IMF B_y. The models of *Heppner and Maynard* [1987] are not flexible, and are constructed in picture form. Some of these limitations were eliminated by *Rich and Maynard* [1989], who derived analytical representations of the Heppner-Maynard patterns. Some flexibilities were added to allow for the changing of the size of the polar cap and the potential drop according to the K_p index. But K_p, a 3-hour index, does not well indicate substorm activity. Note that the time scale of expansion phase of substorm is about 30 minutes.

As discussed by *Lockwood* [1991], the averaged data tend to smooth out the shear convection reversal to reproduce the rotational convection reversal. The models do not reflect properly the dynamic property of polar cap convection since these are steady state. Previous mathematical models have shear convection reversal. A mathematical model which has rotation convection reversal was introduced by *Siscoe and Huang* [1985]. Their model has magnetic flux entering the polar cap on the dayside through a merging gap. The polar cap grows in size while there is no magnetic reconnection in the tail. This model was expanded further by *Moses*

et al. [1987]. They presented a time-dependent ionospheric convection model to simulate the ionospheric flow. This model considers the day-night conductivity gradient and IMF B_y effect on the geometry of the dayside gap. The model consists of a spiral boundary with a gap on it. A potential is applied on the gap and its local time variation of potential is linearly decreasing. It can be seen that the day-night conductivity gradient concentrates the electric field toward dawn. *Moses et al.* [1988] used simple model to simulate measured ionospheric flows from the DE-2 satellite. Roughly 35% of the passes cannot be modeled with a single narrow dayside gap. A nightside gap should be considered. *Moses et al.* [1989] considered a nightside gap in the model. 57% of 39 cases required the nightside gap generated by the nightside reconnection. The nightside reconnection probably occurs after substorm onset and continues throughout the recovery phase.

The expansion and contraction of the polar cap was best illustrated by *Lockwood et al.* [1990]. They have shown how the dynamics of the polar cap are controlled by a day merging potential and a nightside reconnection potential. If only dayside merging potential is present, the polar cap is expanding. The situation is identical to the picture of *Siscoe and Huang* [1985]. In the opposite extreme, the polar cap contracts when only nightside reconnection potential is present. There are non-zero values for both dayside merging potential and nightside reconnection potential in most cases. When these two potentials are equal, the polar cap convection is in a steady state and the convection reversal is shear rather than rotational. This situation is identical to the model of *Heelis et al.* [1982].

Lu et al. [1989] systematically studied the distribution of convection potential around the polar cap boundary under a variety of IMF conditions. The Laplace equation was solved with the assumptions of uniform conductivity and no field-aligned current within the polar cap. They have shown that the zero potential line which separated the dawn and dusk cells, shifts duskward as B_y changes from positive to negative. The results agree well with the data

in spite of the assumptions. The potential distribution was fit by arctangent and sinusoidal functions. They found that the arctangent fit was better than the sinusoidal fit, but their lack of data near noon and midnight prevented them from making a firm conclusion.

1.3 Objective of the Thesis

The objective of this thesis is to determine how the electric potentials are distributed around the convection reversal boundary, and how the boundary locations are shifted under various combinations of orientation and magnitude of IMF, and auroral electrojet activity. By using satellite measurements of the boundary condition, a simple model of the ionospheric convection pattern is constructed to show how the potential and the location of the convection reversal boundary change in different conditions. Ultimately, with a consideration of the nonuniform conductivity and region 2 field-aligned current, an improved model of ionospheric convection patterns is obtained by using these measurements. The development of an improved polar cap convection model, directed toward a more realistic and flexible representation, would be very worthwhile.

The ionospheric convection models have been very valuable in the study of the coupled solar wind-magnetosphere-ionosphere-thermosphere system. Models of the polar cap electric potential are essential in the study of the solar-terrestrial system. In particular, a model of the polar cap electric potential is often required as the input to some other calculations, for instance, the calculations of field-aligned current [*Foster et al.*, 1989; *Siscoe and Maynard*, 1991], and thermosphere-ionosphere global circulation model (TIGCM) [*Roble et al.*, 1988].

CHAPTER 2

Electric Field Measurements

As mentioned in Chapter 1, the objective of this thesis is to investigate the effects of southward IMF on the relationships among the auroral electrojet activity, the ionospheric conductivity, and the convection pattern in the polar ionosphere. Therefore, we need to have some instruments which are installed in satellites or in ground-based stations to monitor the variation of the physical parameters both in interplanetary space and in the ionosphere. Fortunately we have the polar orbiting DE-2 satellite which was used to measure electric fields in the ionosphere; IMP-8 and ISEE-3 located outside of the magnetosphere to measure the IMF, solar wind velocity and number density in the solar wind; and the geomagnetic indices (AL and AU) can detect the maximum density of electrojet current in the ionosphere for indicating the geomagnetic activity. In this chapter the electric field measurements from DE-2 satellite will be emphasized, which serves as the main data set of the thesis. The other two data sets will be discussed in the next chapter.

2.1 DE-2 Mission and VEFI measurements

For this investigation the data have been used from the DE-2 satellite which was launched in August of 1981, into a 300 to 1000 km high polar orbit and with a 98-minute orbital period. It reentered the atmosphere in March of 1983. The electric fields were measured by two identical orthogonal double probes with lengths of 22.4 m tip to tip. These two probes can measure the potentials between two points in space. The electric field can be obtained by dividing the potential difference by the distance between two probes. The original data rate

was 16 samples per second. Half-second average data were used in this study. Further details about the Vector Electric Field Instrument were given by *Maynard et al.* [1981].

Some uncertainty may occur from the interaction between the probes and local plasma, such as the charging of the satellite and contamination of probes. It may cause the measured electric field offset from the actual electric field. This is so called "contact potential," which is usually on the order of one to two mV/m. The contact potential difference can cause a small offset on the measured electric field, but it can also lead to a large error in the potentials when the data are integrated. Another offset was due to the motion of the satellite, creating an additional electric field $\mathbf{V_{sc}} \times \mathbf{B}$, where $\mathbf{V_{sc}}$ is the velocity of the satellite. The contribution from the motion of the satellite has been subtracted from the measured electric field. In this way the satellite reference frame has been transformed to a reference frame which is corotating with the earth. In this reference frame, the corotating plasmasphere should be at an approximately constant potential. But in the real measurements, the potential on the dawnside does not always match the potential on the duskside, which violates the assumption of perfectly corotating plasmasphere. The effect could be caused by the time-varying electric field during the period of each polar cap measurement, or imprecise knowledge of satellite's altitude and geomagnetic field, or intermittent penetration of the magnetospheric electric fields from subauroral plasmasphere. This offset can be either positive of negative. All of these offsets have been adjusted for every pass in order to minimize the errors. The adjustment was made in such a way that the potentials at both ends of each pass were equal.

There are also subauroral electric fields due to the S_q (solar) dynamo that peaks near the equator, where the dawn terminator is charged roughly 8 kV with respect to dusk terminator [*Kelly*, 1989]. The end-point matching of the low-latitude electric potentials actually helps to eliminate systematic dawn/dusk potential offsets that might possibly result from the solar dynamo.

2.2 Determination of Convection Reversal Boundary

Electric potentials are obtained from the integration of the electric fields

$$\Phi = -\int \mathbf{E} \cdot d\mathbf{r}. \tag{2.1}$$

The real electric field measurements are a function of time. The equation (2.1) needs to be rewritten by the change of variable

$$\Phi = -\int \mathbf{E} \cdot \mathbf{V_S} dt \tag{2.2}$$

where $\mathbf{V_S}$ is the velocity vector of the satellite. Or

$$\Phi = -\int (E_x V_x + E_y V_y + E_z V_z) dt \tag{2.3}$$

where the subscripts x, y and z denote the components in a corotating reference frame. The V_y and V_z are zero because velocity vector was defined along the x axis in this reference frame. Thus, the other electric field component E_y and the missing component E_z have no contribution on the relative potential difference which is obtained between two different points. Only the electric field component in the direction of motion of satellite matters. The equation (2.3) becomes

$$\Phi = -\int E_x V_x dt. \tag{2.4}$$

The upper part of Figure 2.1 shows an example of an electric field component in the direction of the satellite, E_x, across the polar cap. Each measurement of E_x is multiplied by the satellite's speed, times the half-second time step, then subtracted from the integrated sum.

An example of the electric potential, which is obtained by the integration of electric fields, is shown in the lower part of Figure 2.1. The potential is initialized to zero at the start of the integration. Also a constant electric field is added to make the potential equal to zero at the

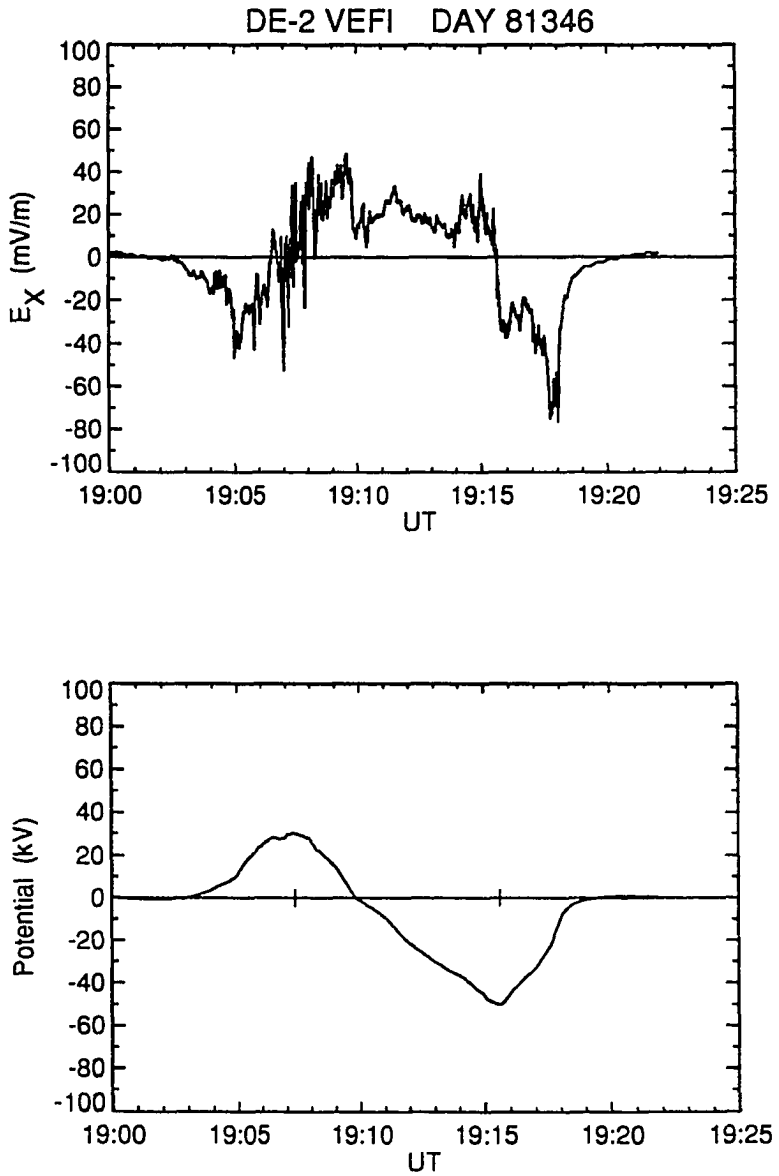

Figure 2.1 Example of the electric field measurement and derived integrated potential. The upper graph shows the electric field component measured along the direction of the satellite's motion on day 346 in 1982. The lower graph shows the electric potential integrated from the measured electric field. The vertical ticks on the horizontal axis represent the locations of the maximum and minimum potentials.

end of the pass. The integrated potential has the local maximum and minimum at the reversal of convection. To avoid ambiguities of irregularities or multiple electric field reversals, the convection reversal boundary is defined as where the potential distribution has its absolute maximum and minimum potentials. The location of the boundary is defined by the colatitude and MLT of maximum and minimum. Two potentials and two locations were obtained from each pass. All the information about the colatitude of convection reversal boundary, MLT and potential around the boundary are stored in a data file for further uses. The data file contains 7018 passes of electric field measurements over the north and south poles.

Another kind of boundary is defined according to the boundary of the open/closed magnetic field line. The correspondence between the field reversal and open/closed boundary has been discussed by *Heelis et al.* [1980]. The average reversal falls 1.5° equatorward of the open/closed boundary. The definition of open/close boundary is not used here.

A step has been taken to insure that the latitude and local time coordinates are used as accurately as possible. Depending on how the magnetic local time is defined and calculated, it is possible to obtain the differences of over an hour for a given point [*Baker and Wing*, 1989], and magnetic conjugate points in opposite hemispheres may not share the same local time. As the data in both hemispheres were mixed, we chose to use "corrected" geomagnetic coordinates. The corrected coordinates for a given location are obtained by tracing the geomagnetic field line from that point to the geomagnetic equator, using a standard reference model. The magnetic local time and equivalent dipolar latitude are calculated at that point. Thus, conjugate points in opposite hemispheres share the same coordinates. Corrected geomagnetic coordinates have been pre-calculated for certain epochs by *Gustafsson* [1984], and *Baker and Wing* [1989]. The international IGRF model for years 1981-1983 has been used for a direct field line tracing.

2.3 Normalization of Potentials on the Convection Reversal Boundary

Numerous measurements obtained under a variety of the random conditions were combined in order to determine the potential distribution around the boundary. In this way the scattering of the data will be larger and the results will be less confident if no adjustment is imposed on the data. Therefore, a normalization procedure has been used to adjust the measurements in each category at the same standard.

The justification for the normalization and methodology is illustrated in Figure 2.2. The upper row shows two different random measurements with a hypothetical function. For example, one measurement with the extreme potentials of -35 kV and 20 kV is obtained when the transpolar cap potential is 80 kV, but there is no way of knowing that the potential was indeed 80 kV. In another pass, a measurement with the extreme potentials of -55 kV and 30 kV at different location is obtained, but the actual transpolar cap potential may be 120 kV at that time due to an increased voltage in the solar wind. Note that the absolute values of the minimum and maximum of this hypothetical function need not to be the same. If the data were fit without the normalization, the combined function has larger residual errors, as shown on the lower-left side of Figure 2.2. However, if each measurement is normalized by Φ_{min}, the minimum potential of hypothetical function, then combine them, the curve fit is perfect, as shown on the lower-right side of Figure 2.2.

There are two possible candidates for normalizing the original data, Φ_{min} and Φ_{max}. The problem is that there is no way of knowing the value of Φ_{min} and Φ_{max}, but an estimation is obtained from the use of the auroral electrojet indices, AU and AL. *Weimer et al.* [1990a] correlated the AU and AL indices with the dusk and dawn cell potentials. They have shown that the westward and eastward electrojet currents are roughly proportional to the dawn and dusk cell potentials. But the correlation between AL and dawn cell potential is not as good

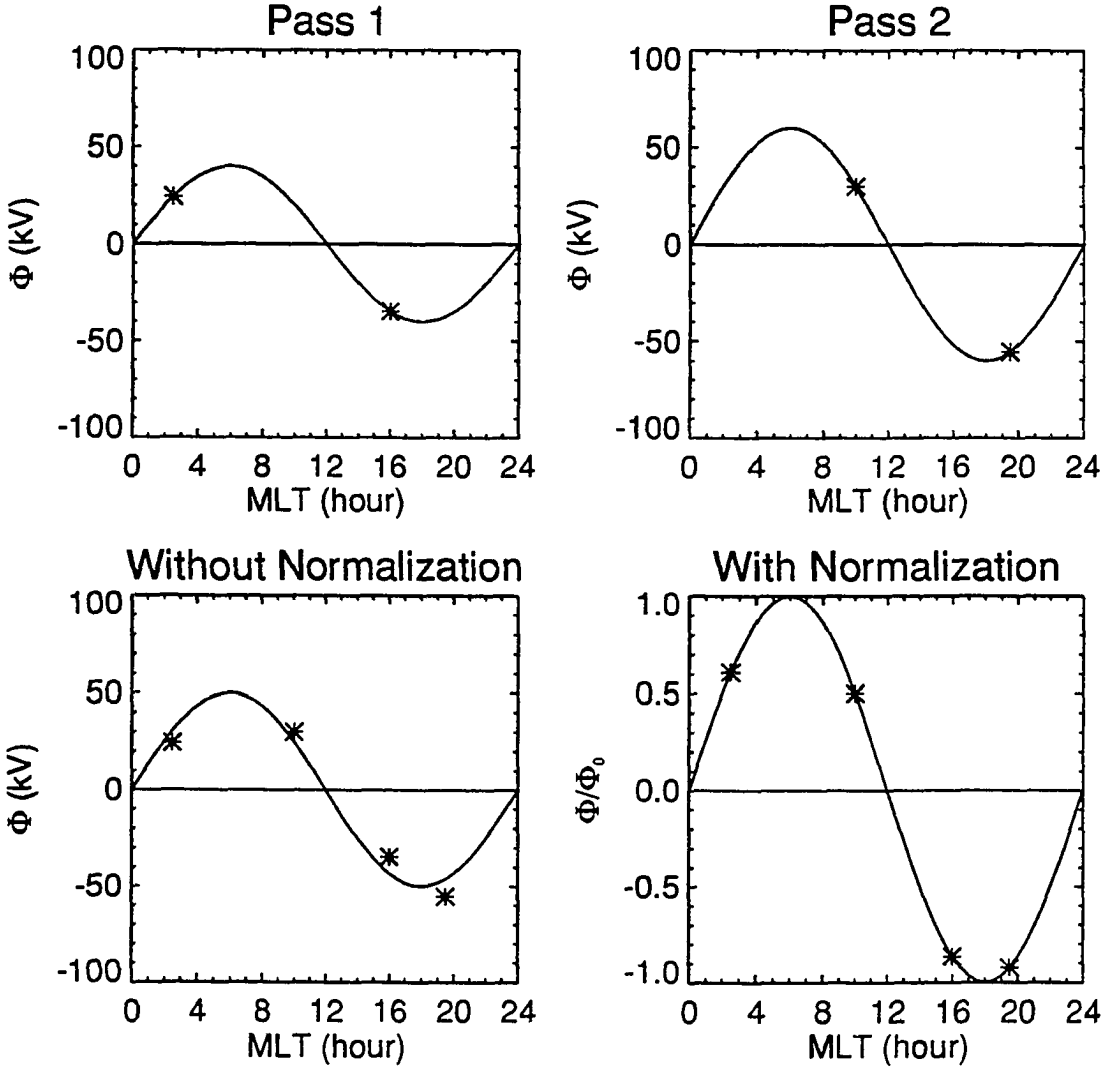

Figure 2.2 Comparison of the procedures with and without normalization. The upper row shows two different random measurements under different hypothetical potential functions. Combining these two measurements, the procedure without normalization results in larger residual errors, as shown in the lower row.

as the correlation between AU and dusk cell potential, as show in Figure 2.3. The reason is because the localized change in the convection pattern near the midnight can increase the westward electrojet and AL index during substorms. The relationship between AL and dawn cell potential seems to depend on whether a substorm is in progress.

It was also shown by *Weimer et al.* [1990a] that the ratio between AU and dusk cell potential varies with seasons due to the changes in the ionospheric conductivity by solar EUV radiation. The measured AU needs to be compensated for the time of year according to the formula [*Weimer et al.*, 1990b]

$$AU_C = AU_M\left\{1 + \left(\frac{AU_{MAX}}{AU_{MIN}} - 1\right)\sin^2\left[(d - 172)\frac{\pi}{365}\right]\right\} \tag{2.5}$$

where AU_C and AU_M are the corrected AU and measured AU, respectively, and d is the Julian day of year. AU_{MAX} is the average of AU between days 167-176 (summer) for 3 years (1981-1983) and AU_{MIN} is the average of days 350-359 (winter) during the same years. The ratio of AU_{MAX} to AU_{MIN} is about 1.96 according to the calculation. The equation (2.5) can be rewritten to

$$AU_C = AU_M\left\{1 + 0.96\sin^2\left[(d - 172)\frac{\pi}{365}\right]\right\}. \tag{2.6}$$

The purpose of using the relationship between AU index and dusk cell potential is to obtain a relative Φ_{min} simultaneously with the electric field measurement. However, the AU index is measured by the magnetometer stations in the northern hemisphere. Thus, the relationship between AU index and dusk cell potential depends on the conductivity and season in the northern hemisphere. Since Φ_{min} should be approximately the same in both hemispheres, the equation (2.6) is used without any phase shift of day-of-year if the electric field measurements are obtained in the southern hemisphere.

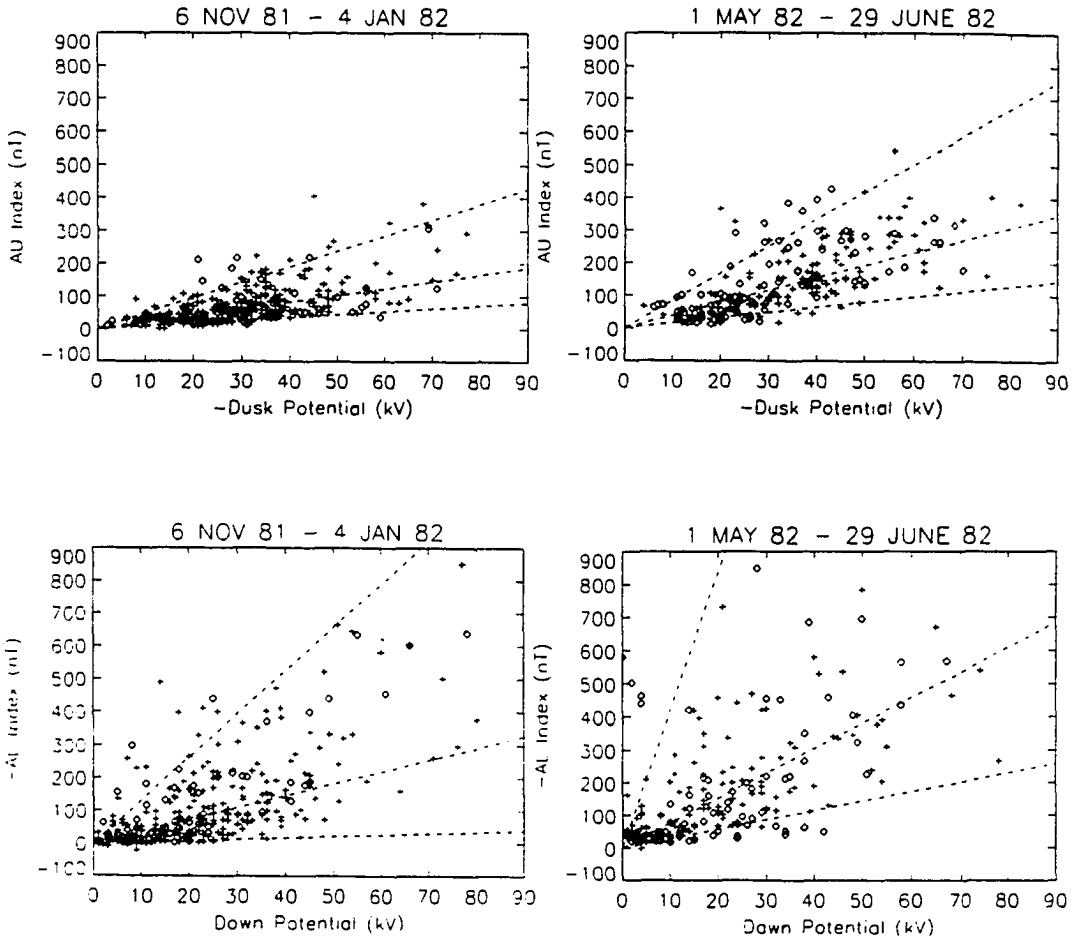

Figure 2.3 Scatter plots of AU index vs. $-$dusk potential and $-AL$ vs. dawn potential in different seasons. The plus symbols represent the data in the northern hemisphere and the diamond symbols represent the data in the southern hemisphere. The dashed lines are at constant slopes which bound 10%, 50%, and 90% of the data points [*Weimer et al.*, 1990a].

It is to be noted that in this study there is no need to know or assume a value for the proportionality constant between the AU_C and Φ_{min}. The normalized data are combined together to obtain the function of Φ/AU_C as a function of MLT. This function has the confusing units of kV/nT. But with a multiplication of the mean value of AU_C for each category, the resulting function has the desired units of kV, as the Φ_{min}/AU_C ratio is cancelled in the end.

CHAPTER 3

Observational Determination of Boundary Potentials and Locations

The investigation started with nearly all the VEFI data obtained during the DE-2 mission. But the data tapes contain numerous duplicate passes, and many more incomplete passes, which began or ended within the polar cap. Also there are some cases where the data are contaminated with transmission errors, gaps, or instrument calibration cycles. Several criteria have been imposed on the data in order to eliminate the bad or incomplete passes. For instance, both the starting and ending points were required to be below 58° invariant latitude. Only 5595 polar cap passes were left after elimination.

It is well known that the IMF and geomagnetic activity affect the pattern of the ionospheric convection and electric potential. Thus, the other two data sets, the IMF data from IMP-8 and ISEE-3 satellites, geomagnetic indices (AL and AU) from ground-based magnetometer stations, were used to group the passes of DE-2 satellite. In this chapter these two data sets will be discussed in the separate sections. A fitting procedure to best fit a periodic function in terms of MLT will be shown in the final section.

3.1 Grouping the Electric Field Measurements by Southward IMF

Since the objective of this study is to explore the relationship between the IMF and electric potential in the ionosphere, both the IMF and electric field measurements should be simultaneous. The IMP-8 spacecraft was launched on October 26, 1973, in an orbit of 30 to 40 R_E, where R_E is the radius of earth. The IMF data from IMP-8 are available with 5-minute resolution, which is distributed on tape by National Space Science Data Center (NSSDC).

There are numerous data gaps in IMF data of IMP-8. Thus, using 5-minute IMP-8 data alone left us with too few passes to complete this study. The ISEE-3 satellite provided reasonably continuous solar wind measurements from an orbit 200 to 260 R_E upstream of earth, which are shifted in time to correct for the time delay between the measurements and the solar wind's arrival at the earth. In this study 1-hour IMF data from the NSSDC's "OMNI" data base have been used. This data base combined IMP-8 and time-shifted ISEE-3 measurements [*Couzens and King*, 1986].

If the passes had well-defined maximum or minimum potentials, but no corresponding IMF, the passes were not used in this study. The ionospheric convection responds to the IMF on a time scale of about 10 to 20 minutes. Thus, the prior hour of IMF was used when the starting time of each polar measurement was in the first 15 minutes, otherwise the current hour of IMF was used. There are 2156 passes discarded due to the lack of corresponding IMF data, leaving 3439 passes.

This study primarily deals with how the two-cell convection pattern varies with IMF. The two-cell convection pattern is formed when the IMF is southward. Also the IMF B_y may change the orientation of the two-cell convection pattern. Therefore only IMF B_y and B_z were used. The data were sorted into 3 major groups based on the z component of IMF, $B_z > +1$, $-4 \leq B_z \leq +1$ and $B_z < -4$. The groups for $B_z > +1$ were not used because the two-cell convection pattern is not well-defined for northward IMF. The other two groups were further sorted into three subgroups according to the y component of IMF, $B_y \geq +4$, $-4 < B_y < +4$ and $B_y \leq -4$. Note that the convection patterns are reversed in response to B_y in opposite hemispheres, for example, the convection model BC of *Heppner and Maynard* [1987] is for the northern hemisphere with a positive B_y and for the southern hemisphere with a negative B_y. Thus, it is reasonable to combine together with the passes of northern hemisphere for $B_y > 0$ and the passes of southern hemisphere for $B_y < 0$, or with the passes of northern hemisphere

for $B_y < 0$ and the passes of southern hemisphere for $B_y > 0$. In this thesis, the sign of B_y is defined in the northern hemisphere. The measurements obtained in the southern hemisphere have been reversed before combining the measurements in the northern hemisphere. To verify this, each subgroup in group ($-4 < B_z < +1$) has been divided into two categories according to the hemisphere.

Ideally it is better to group the data with finer division, but the number of random measurements in each category should be sufficient for obtaining significant results. The number of passes in the subgroup ($-4 < B_y < +4$, $-4 \leq B_z \leq +1$) are more than 300 passes. This subgroup was grouped further into three subgroups based on finer B_y conditions ($-4 < B_y < -1$, $-1 \leq B_y \leq +1$, and $+1 < B_y < +4$).

3.2 Grouping the Electric Field Measurements by AU and AL Indices

The auroral electrojet indices (AL, AU, AE) were originally introduced by *Davis and Sugiura* [1966] as a measure of electrojet activity in the auroral zone. The electrojet indices are obtained from 10 to 12 ground-based magnetometer stations distributed in the auroral oval, superimposing the horizontal, northern component of geomagnetic variation H from all the stations. The lower envelope is called the AL index and higher envelope is called the AU index. The AU index is usually positive and the AL index is usually negative. Occasionally the AU index is a negative number and the AL is a positive number due to the contamination from the magnetospheric ring current and the zonal current in the ionosphere. The AL and AU indices are the measurement of maximum westward and eastward electrojet currents, respectively. The absolute difference between AL and AU indices is AE index, which indicates the total maximum current of eastward and westward electrojet. By definition the AE is always positive and independent of zonal current. The AE index is less obvious

than the AL and AU indices in physical meaning. Only the AL and AU indices were used in this study. Note that AL, AU, and AE indices are not a measurement of total electrojet currents, but are only related to the maximum density of the electrojet current. The AL, AU, and AE indices are calculated with a 1-minute time resolution and distributed by the World Data Center C2 for geomagnetism at Kyoto University. These indices have more advantages over the standard K_p index because the time resolution is 1 minute rather than 3 hours.

As mentioned in the introductory chapter, the electrojet system can be divided into intense electrojet (DP 1 system) and weak electrojet (DP 2 system) according to the signatures which are obtained with a global chain of magnetometers. The DP 2 system tends to be associated with direct-driven process. The DP 1 system is characterized by substorm unloading process. For each pass, whether the DP 1 or DP 2 system is dominant has been determined on the basis of the simultaneous AU and AL indices. The corresponding AU and AL indices are obtained by averaging the AU and AL 1-minute indices between the starting and ending times of each polar cap pass. Following a hint by *Kamide* [1991], Figure 3.1 is a diagram of averaged AU and AL variations from 55 isolated substorms. In order to divide the data into two additional categories with relatively intense and weak westward electrojets, corresponding to the DP 1 and DP 2 systems, a dividing line have been selected at $|AL| = 1.5 \cdot AU$. Figure 3.1 illustrates how this factor of 1.5 neatly divides the substorm chronology between the DP 1 and DP 2 systems. This factor makes an allowance for the times that have a DP 2 configuration but the absolute value of AL is slightly greater than AU due to the random noise. The grouping of the data between intense and weak electrojets was done by a computer which only compared the ratios of the absolute value of AL to AU. A two-cell convection may not be formed when the AU index is low. Only passes with $AU > 100$ nT were used. Only 1125 passes survived the data selection.

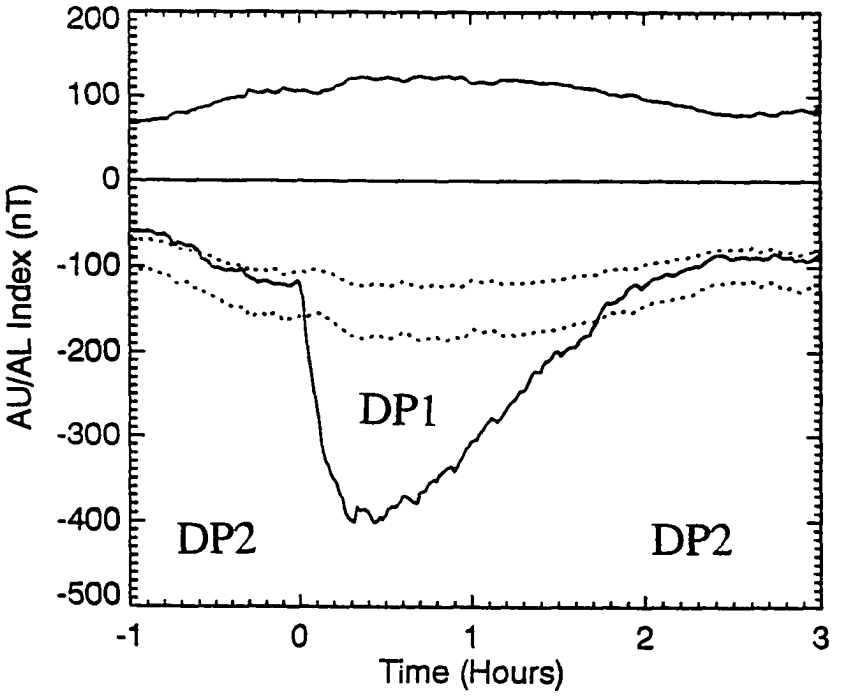

Figure 3.1 Evolution of auroral electrojet indices during substorm. The AU and AL (solid lines) are obtained by superposed epoch analysis of 55 isolated substorms. The upper and lower dotted lines show AU multiplied by a factor of -1 and -1.5, respectively. The divisions between the times when DP 1 and DP 2 current systems are assumed to be located where the AL index crosses the lower dotted line [*Weimer, 1993*].

3.3 Functional Representations of Boundary Potentials and Locations

At this point the measurements of the electric field have been divided into 18 categories based on the IMF B_y and B_z, and the ratio of absolute AL to AU. Note that the random measurements have not been grouped further with seasonal divisions because it ends up with insufficient data points in each category. In this section the data in each category have been plotted against MLT and a Fourier series was used to best fit them, in order to obtain functions of boundary potentials and boundary locations as a function of MLT.

3.3.1 A Procedure of Fourier fitting

Our objective is to obtain a mathematical function which best fits the random measurements. It is inappropriate to assume a particular function in advance. Thus, a flexible curve-fitting procedure is needed to work with any function. It is known that any periodic function can be represented with a Fourier series, a superposition of sine/cosine functions

$$f(MLT) = C_0 + \sum_{n=1}^{N} C_n \cos\left[\frac{n\pi}{12} MLT - \varphi_n\right]. \tag{3.1}$$

Since the data used in this study are randomly spaced, a conventional discrete Fourier transform (DFT) cannot be used. Instead, a least-squares fit of a cosine function have been used to determine each individual coefficient C_n and corresponding phase angle φ_n, starting with the lowest harmonic. After each term in the series was determined by the least-squares fit, the derived curve was subtracted from the data points. The residual errors were fit with the next higher-order harmonic. The approach of least-squares is to generate a function which has a minimum deviation between the experimental values and the values computed from it. The details of least-squares method are shown in Appendix A.

3.3.2 Functions to Represent the Boundary Potentials

The normalized potentials at the convection reversal boundary have been plotted against the MLT in each category, as shown in Figures 3.2 - 3.13. The plus symbols represent the points at a maximum potential and the diamond symbols represent the points at a minimum potential. The maximum potential points usually occur on the dawnside and the minimum potential points usually occur on the duskside, but occasionally the maximum potential points were found between 15 and 21 MLT and the minimum potential points were found between 2 and 8 MLT. These points might be attributed to the northward IMF, and were discarded, as the data did not conform to the model of the typical two-cell convection pattern.

The normalized potentials, f_p, were fit in a form which is identical to (3.1), but in different coefficient notations

$$f_p(MLT) = A_0 + \sum_{n=1}^{N} A_n \cos[\frac{n\pi}{12} MLT - \phi_n] \qquad (3.2)$$

where A_0, A_n, and ϕ_n are the coefficients to be determined by the approach mentioned in Subsection 3.3.1. The values of these coefficients are listed in Tables 3.1-3.3. It was found that the use of higher-order coefficients can lead to unrealistic, small-scale oscillation. starting with lowest harmonic, a termination of the series at $n = 3$ produced a satisfactory match between the series representation and the data points. The fitting curves are shown as the dash lines in Figures 3.2 - 3.13. From looking at the data points near noon or midnight, the potential distribution does not appear to be a continuous, single-value function. Thus, the same curve-fitting process has been repeated, but fitting the maximum and minimum potential separately. The values of these coefficients are listed in Tables 3.4-3.6. The results are shown as the solid lines in Figures 3.2 - 3.13.

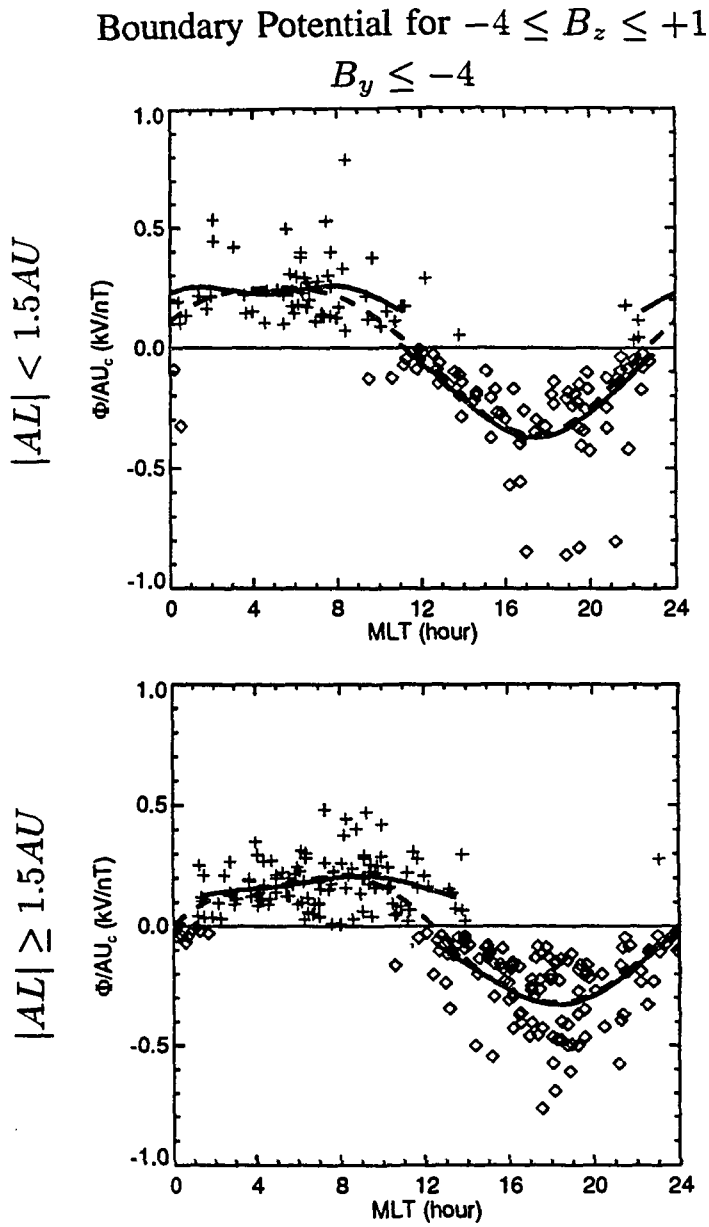

Figure 3.2 Normalized potential on the convection reversal boundary for the subgroup with $-4 \leq B_z \leq +1$ and $B_y \leq -4$. The upper graph shows the data points under an intense electrojet and the lower graph shows the data points under a weak electrojet. The plus symbols represent dawn/maximum potential points and the diamond symbols represent dusk/minimum potential points. These points were fit separately (solid lines) and together (dash lines).

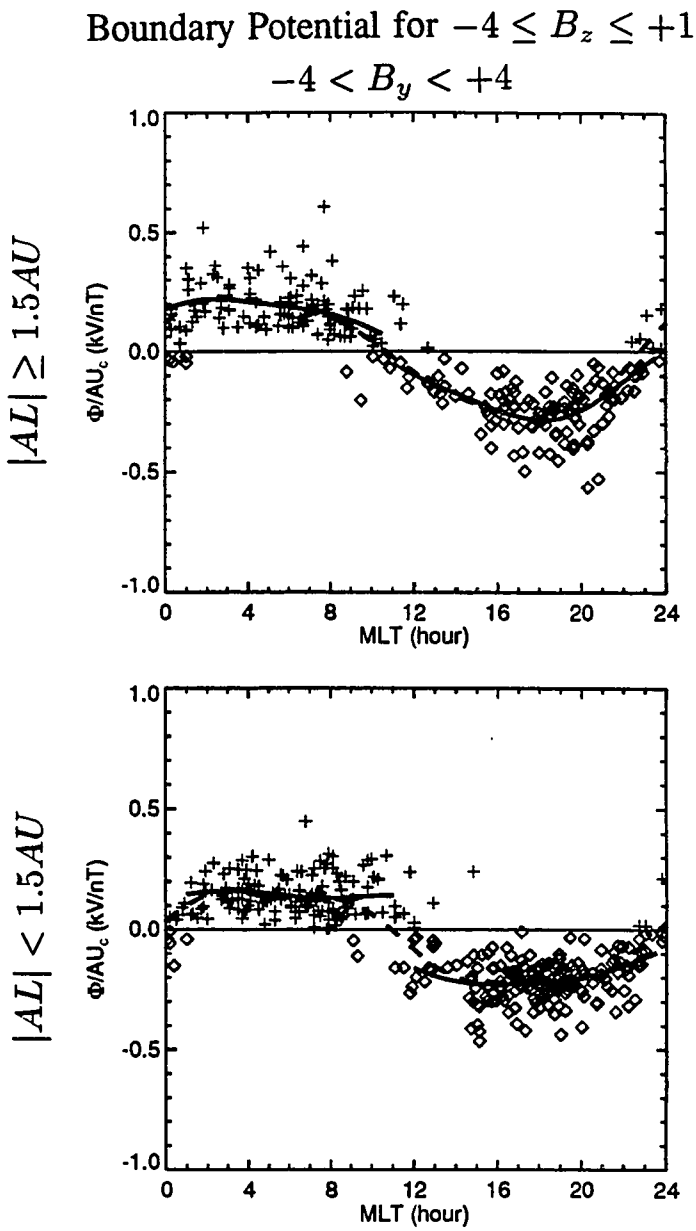

Figure 3.3 Normalized potential on the convection reversal boundary for the subgroup with $-4 \leq B_z \leq +1$ and $-4 < B_y < +4$. The representation of lines and symbols is the same as that in Figure 3.2.

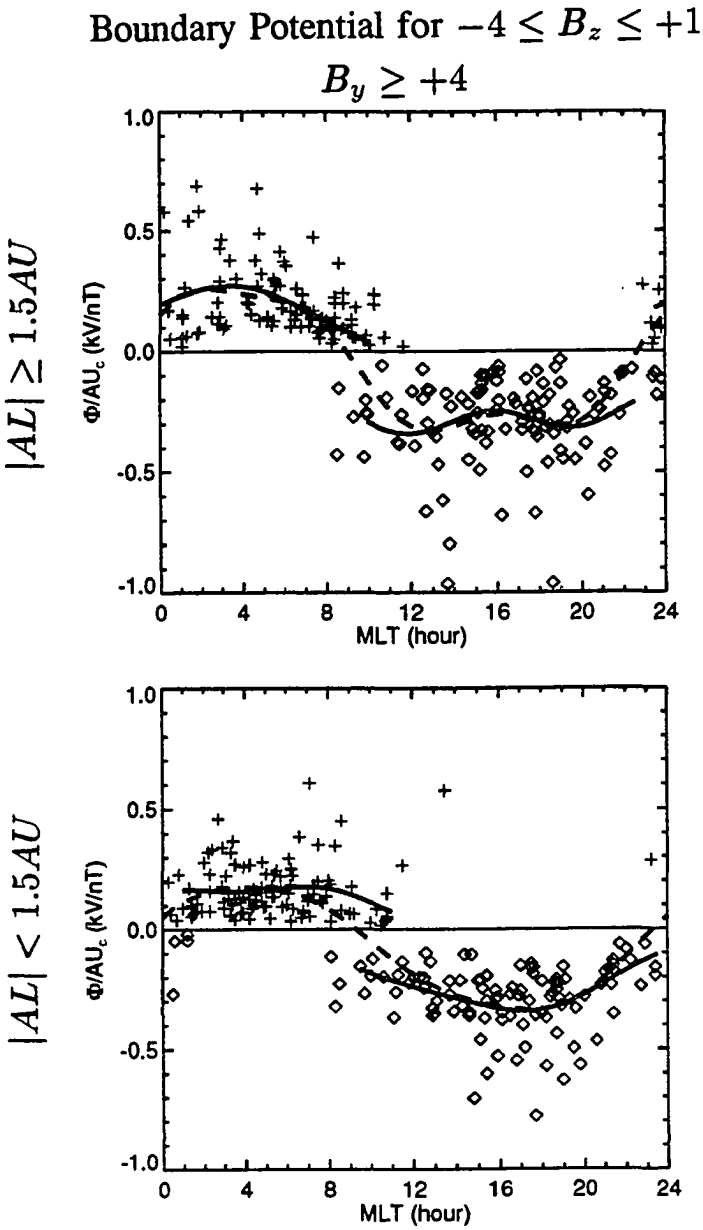

Figure 3.4 Normalized potential on the convection reversal boundary for the subgroup with $-4 \leq B_z \leq +1$ and $B_y \geq +4$. The representation of lines and symbols is the same as that in Figure 3.2.

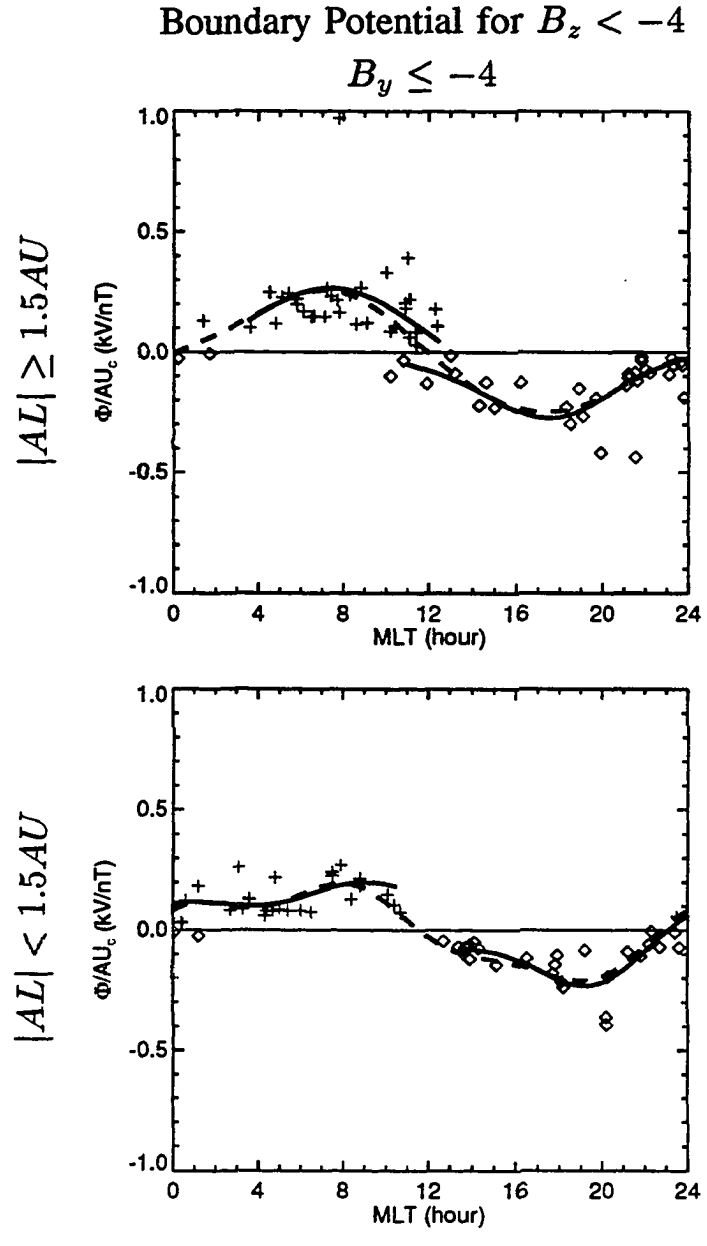

Figure 3.5 Normalized potential on the convection reversal boundary for the subgroup with $B_z < -4$ and $B_y \leq -4$. The representation of lines and symbols is the same as that in Figure 3.2.

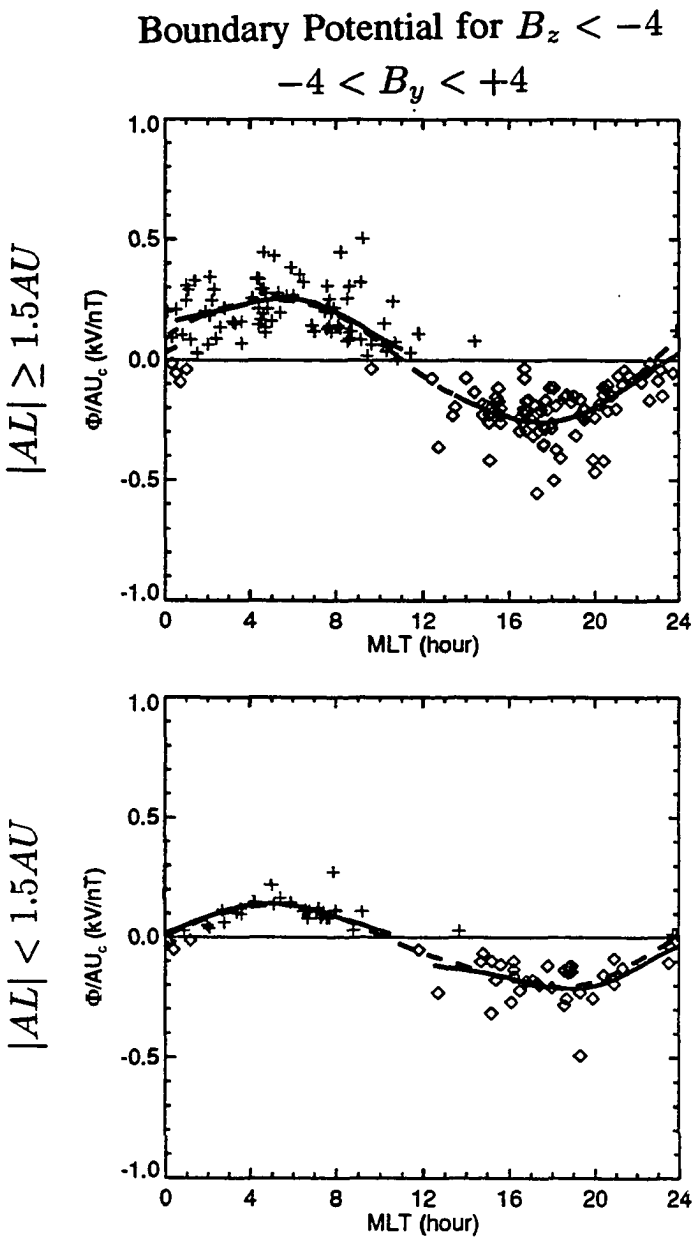

Figure 3.6 Normalized potential on the convection reversal boundary for the subgroup with $B_z < -4$ and $-4 < B_y < +4$. The representation of lines and symbols is the same as that in Figure 3.2.

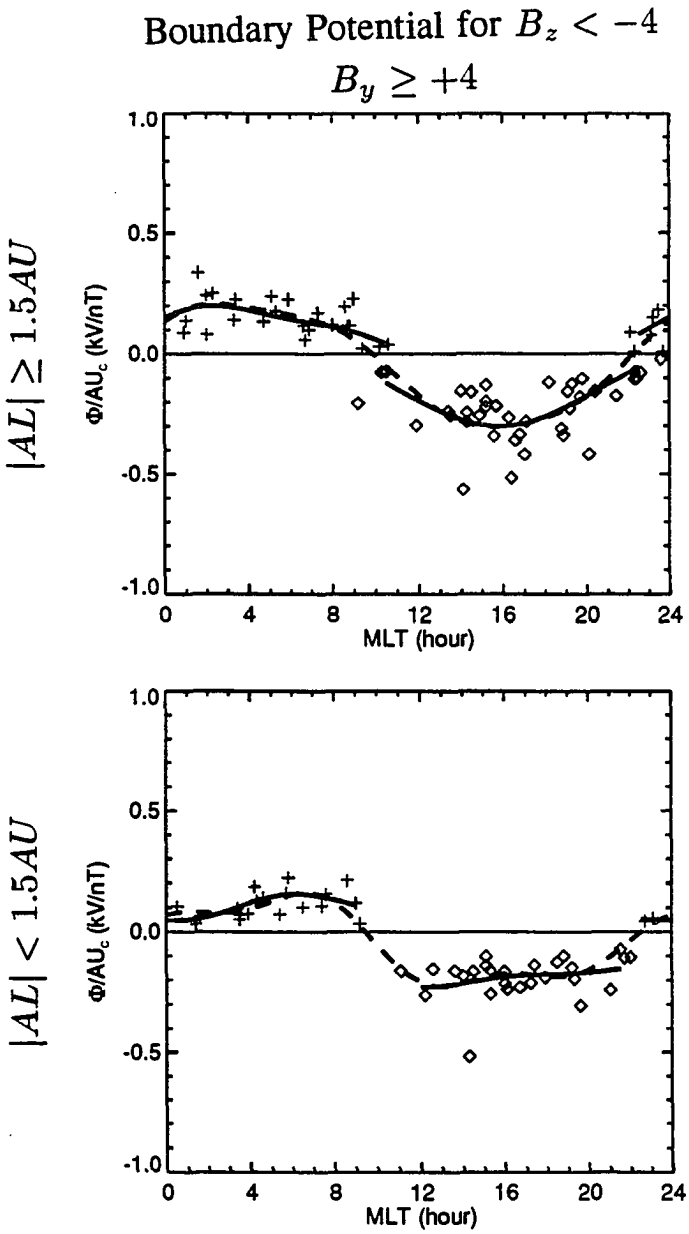

Figure 3.7 Normalized potential on the convection reversal boundary for the subgroup with $B_z < -4$ and $B_y \geq +4$. The representation of lines and symbols is the same as that in Figure 3.2.

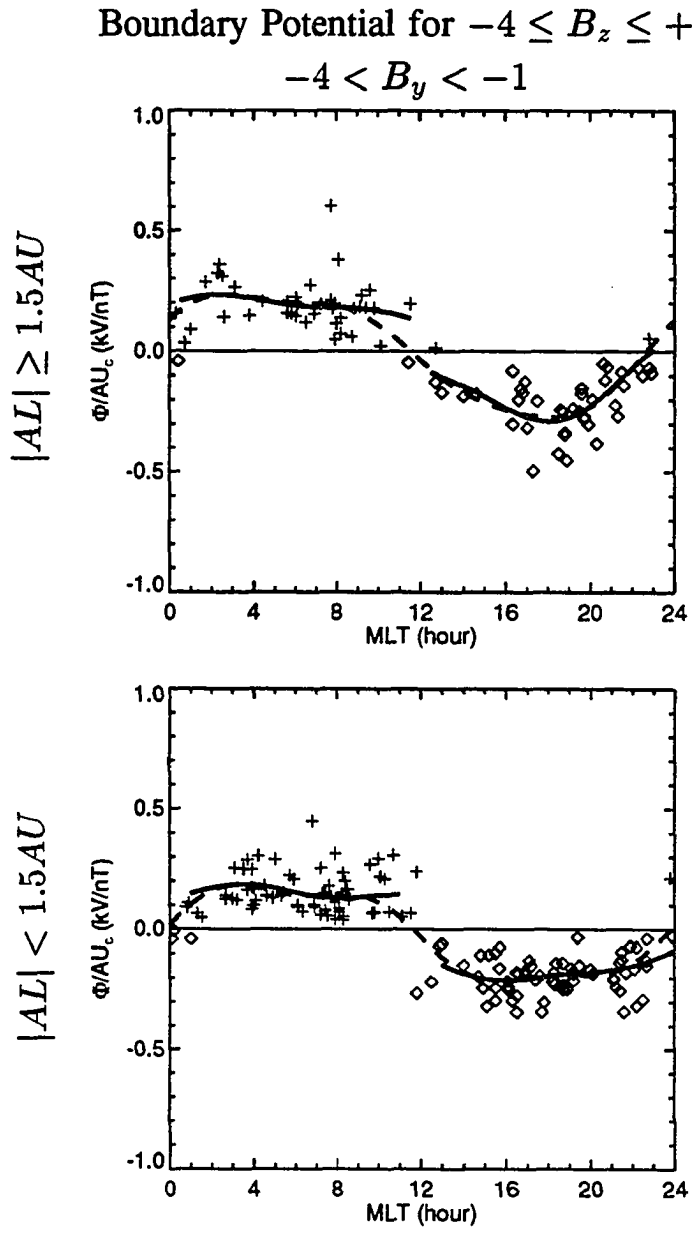

Figure 3.8 Normalized potential on the convection reversal boundary for the subgroup with $-4 \leq B_z \leq +1$ and $-4 < B_y < -1$. The representation of lines and symbols is the same as that in Figure 3.2.

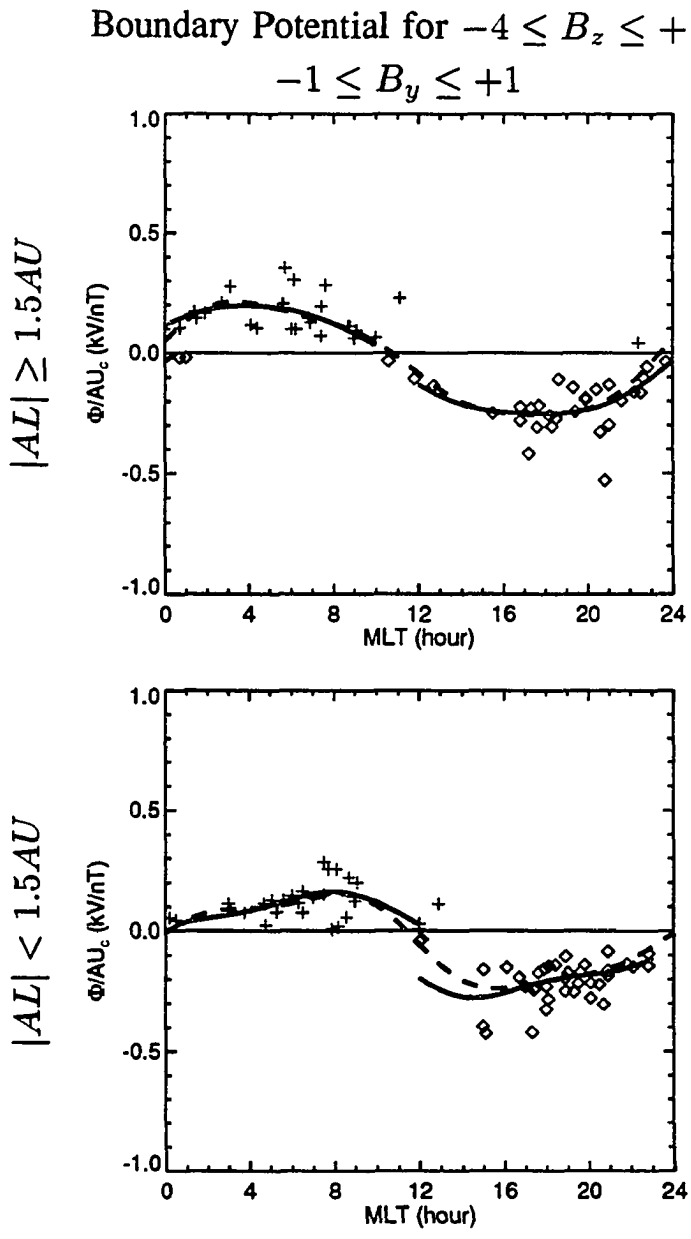

Figure 3.9 Normalized potential on the convection reversal boundary for the subgroup with $-4 \leq B_z \leq +1$ and $-1 \leq B_y \leq +1$. The representation of lines and symbols is the same as that in Figure 3.2.

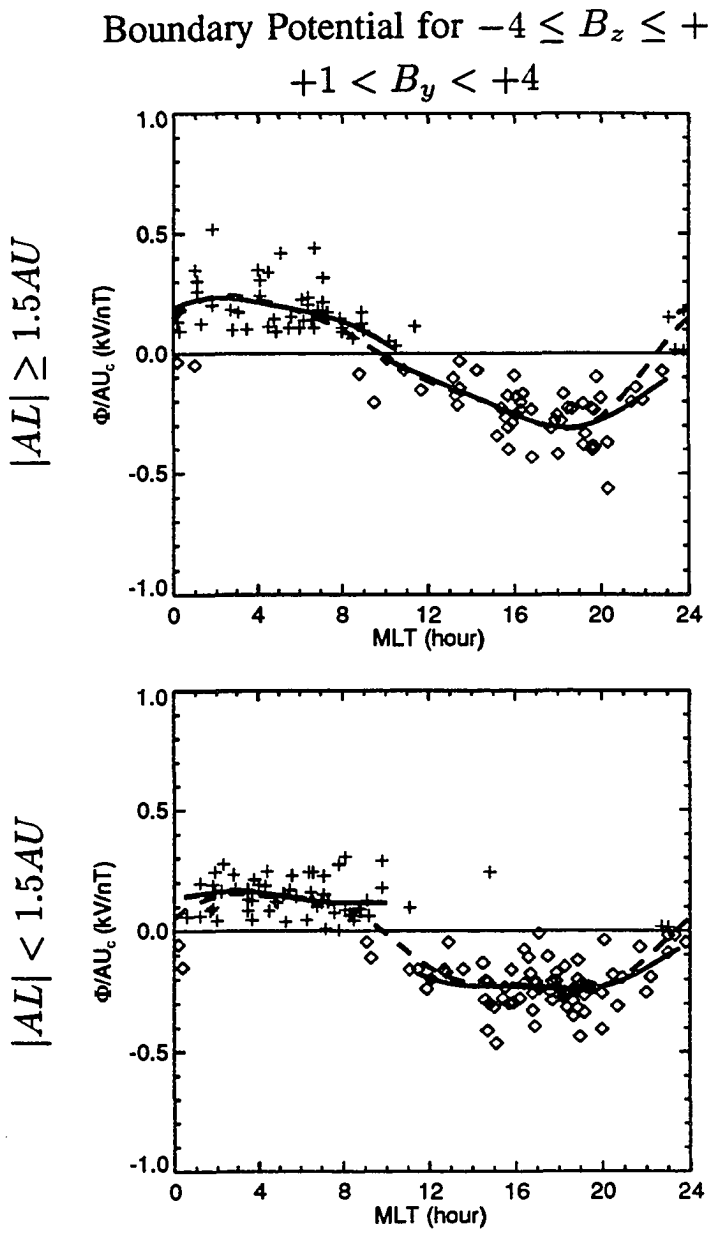

Figure 3.10 Normalized potential on the convection reversal boundary for the subgroup with $-4 \leq B_z \leq +1$ and $+1 < B_y < +4$. The representation of lines and symbols is the same as that in Figure 3.2.

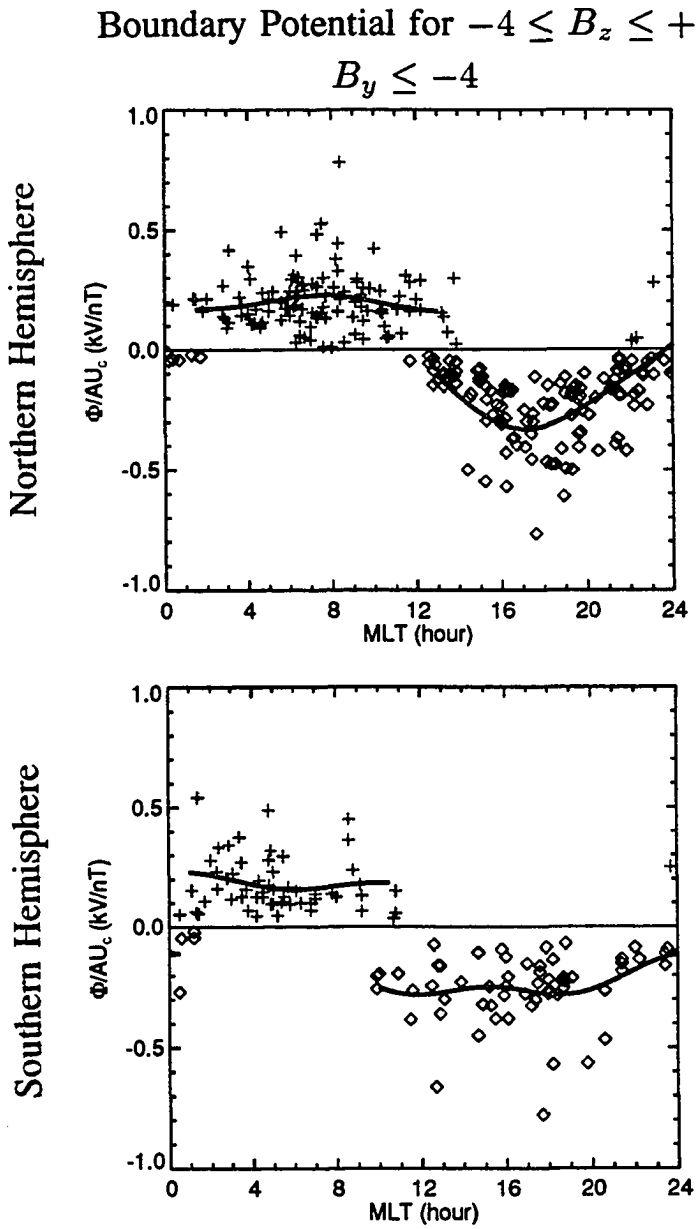

Figure 3.11 Normalized potential on the convection reversal boundary for the subgroup with $-4 \leq B_z \leq +1$ and $B_y \leq -4$. The upper graph shows the data points in the northern hemisphere and the lower graph shows the data points in the southern hemisphere. The plus symbols represent dawn/maximum potential points and the diamond symbols represent dusk/minimum potential points. These points were fit separately (solid lines).

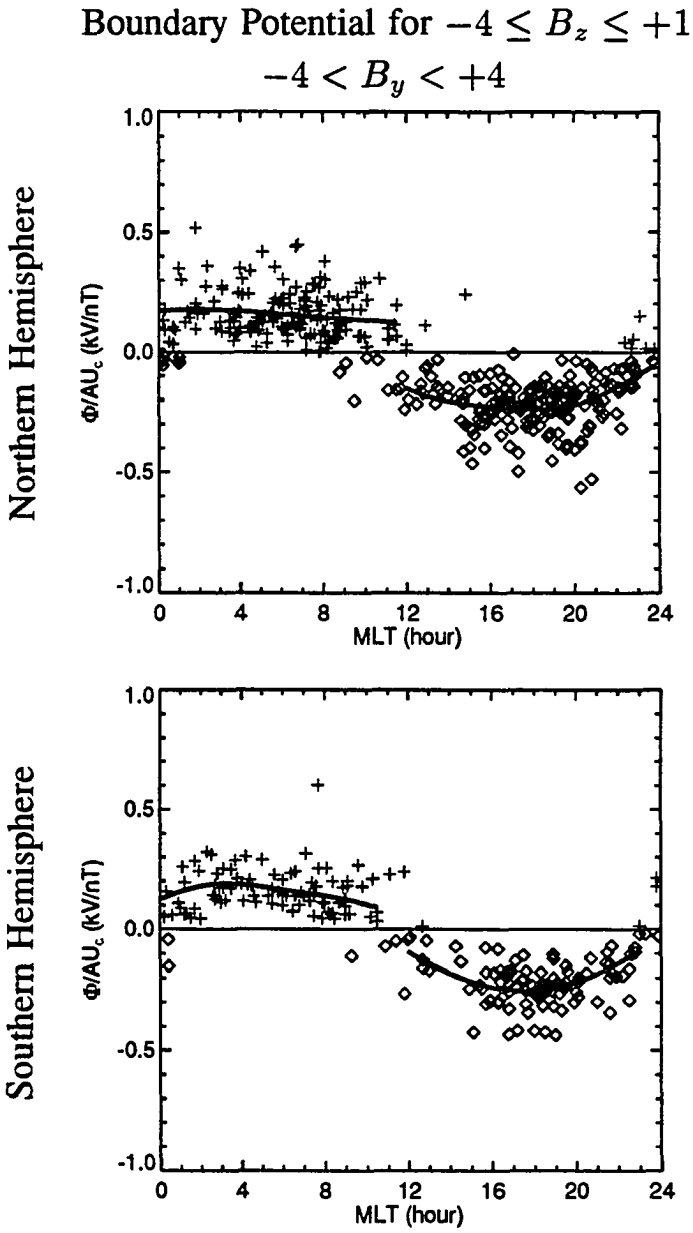

Figure 3.12 Normalized potential on the convection reversal boundary for the subgroup with $-4 \leq B_z \leq +1$ and $-4 < B_y < +4$. The representation of lines and symbols is the same as that in Figure 3.11.

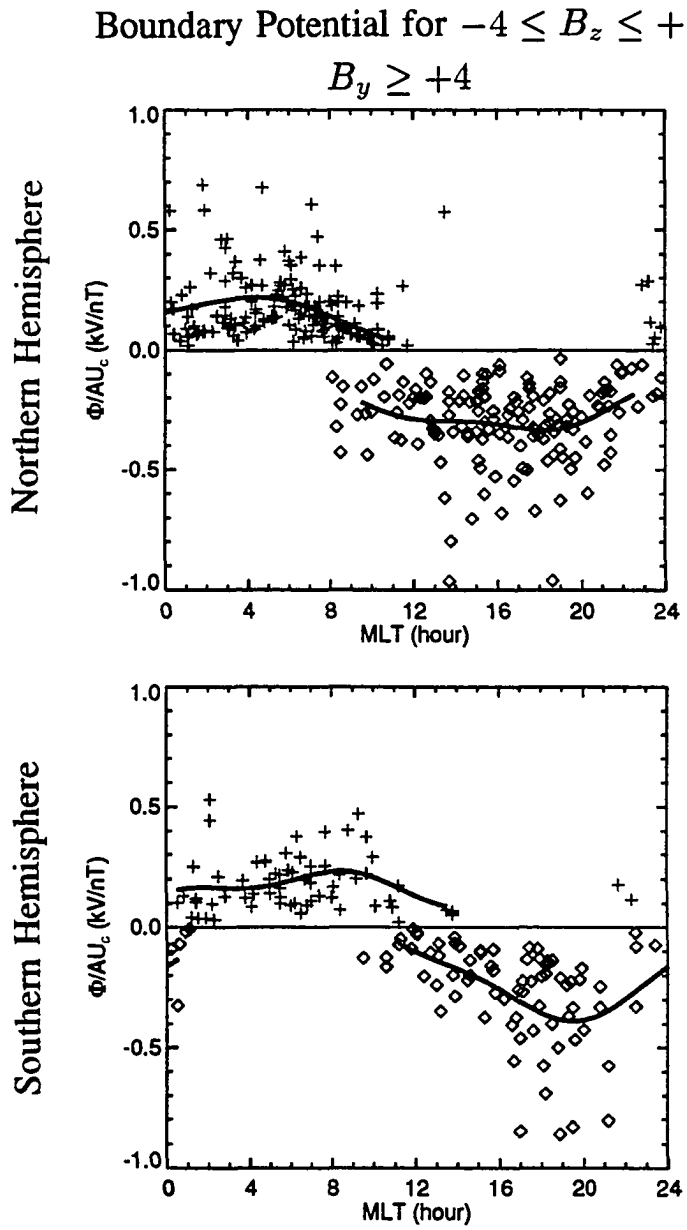

Figure 3.13 Normalized potential on the convection reversal boundary for the subgroup with $-4 \leq B_z \leq +1$ and $B_y \geq +4$. The representation of lines and symbols is the same as that in Figure 3.11.

Table 3.1 Information about continuous curve fits for the group with $-4 \leq B_z \leq +1$.

Categories	Number of Points	AU_{ave}(nT)	n	A_n(kV/nT)	ϕ_n(rad.)	B_n(deg.)	θ_n(rad.)
$B_y \leq$ -4	138	178	0	-0.013	-	16.340	-
-4 $\leq B_z \leq$ +1			1	0.307	1.482	3.478	-0.612
|AL| $\geq$ 1.5AU			2	0.048	-0.041	1.584	-0.252
			3	0.006	0.230	-	-
-4 < B_y < +4	242	191	0	-0.022	-	16.238	-
-4 $\leq B_z \leq$ +1			1	0.260	1.380	3.690	-0.116
|AL| $\geq$ 1.5AU			2	0.039	0.841	1.232	-0.268
			3	0.023	0.884	-	-
$B_y \geq$ +4	209	178	0	-0.052	-	15.498	-
-4 $\leq B_z \leq$ +1			1	0.309	1.109	3.062	0.337
|AL| $\geq$ 1.5AU			2	0.049	2.161	0.443	-2.827
			3	0.059	0.482	-	-
$B_y \leq$ -4	243	183	0	-0.029	-	14.970	-
-4 $\leq B_z \leq$ +1			1	0.267	1.776	4.748	-0.475
|AL| < 1.5AU			2	0.046	0.027	1.529	0.318
			3	0.014	1.498	-	-
-4 < B_y < +4	340	194	0	-0.032	-	15.204	-
-4 $\leq B_z \leq$ +1			1	0.208	1.486	3.651	-0.032
|AL| < 1.5AU			2	0.007	0.444	0.939	0.038
			3	0.034	1.559	-	-
$B_y \geq$ +4	210	178	0	-0.077	-	14.218	-
-4 $\leq B_z \leq$ +1			1	0.266	1.300	4.349	0.363
|AL| < 1.5AU			2	0.015	1.028	0.760	-0.188
			3	0.016	0.420	-	-

Table 3.2 Information about continuous curve fits for the group with $B_z < -4$.

Categories	Number of Points	AU_{ave}(nT)	n	A_n(kV/nT)	ϕ_n(rad.)	B_n(deg.)	θ_n(rad.)
$B_y \leq$ -4	68	275	0	0.008	-	18.751	-
$B_z <$ -4			1	0.239	1.732	4.220	-0.440
|AL| $\geq$ 1.5AU			2	0.038	-1.358	1.260	1.037
			3	0.009	-0.312	-	-
-4 $< B_y <$ +4	182	259	0	0.004	-	17.833	-
$B_z <$ -4			1	0.258	1.445	3.181	-0.103
|AL| $\geq$ 1.5AU			2	0.010	0.725	2.120	-0.679
			3	0.013	0.366	-	-
$B_y \geq$ +4	78	305	0	-0.031	-	17.492	-
$B_z <$ -4			1	0.264	1.157	2.277	0.638
|AL| $\geq$ 1.5AU			2	0.022	-0.359	2.080	-1.134
			3	0.020	1.014	-	-
$B_y \leq$ -4	54	392	0	-0.001	-	18.123	-
$B_z <$ -4			1	0.182	1.636	5.133	-0.774
|AL| < 1.5AU			2	0.030	-0.220	1.757	-0.071
			3	0.045	0.602	-	-
-4 $< B_y <$ +4	72	335	0	-0.031	-	16.484	-
$B_z <$ -4			1	0.167	1.541	5.200	0.205
|AL| < 1.5AU			2	0.013	1.639	2.147	-0.106
			3	0.009	-0.377	-	-
$B_y \geq$ +4	49	349	0	-0.040	-	17.043	-
$B_z <$ -4			1	0.183	1.183	5.022	0.240
|AL| < 1.5AU			2	0.030	-2.460	1.795	-1.060
			3	0.050	0.160	-	-

Table 3.3 Information about continuous curve fits for the subgroup with $-4 \leq B_z \leq +1$ and $-4 < B_y < +1$.

Categories	Number of Points	AU_{ave}(nT)	n	A_n(kV/nT)	ϕ_n(rad.)	B_n(deg.)	θ_n(rad.)
$-4 < B_y < -1$	83	194	0	-0.006	-	16.227	-
$-4 \leq B_z \leq +1$			1	0.261	1.455	4.104	-0.371
$\|AL\| \geq 1.5AU$			2	0.041	0.398	1.523	-0.662
			3	0.026	1.091	-	-
$-1 \leq B_y \leq +1$	57	194	0	-0.034	-	16.360	-
$-4 \leq B_z \leq +1$			1	0.243	1.438	3.794	0.106
$\|AL\| \geq 1.5AU$			2	0.023	1.244	1.406	-0.089
			3	0.024	1.753	-	-
$+1 < B_y < +4$	102	188	0	-0.028	-	16.193	-
$-4 \leq B_z \leq +1$			1	0.265	1.284	3.313	0.015
$\|AL\| \geq 1.5AU$			2	0.059	1.022	1.065	0.042
			3	0.025	0.283	-	-
$-4 < B_y < -1$	135	201	0	-0.017	-	15.790	-
$-4 \leq B_z \leq +1$			1	0.209	1.587	4.498	-3.398
$\|AL\| < 1.5AU$			2	0.009	0.616	0.942	0.436
			3	0.044	1.949	-	-
$-1 \leq B_y \leq +1$	66	191	0	-0.037	-	14.873	-
$-4 \leq B_z \leq +1$			1	0.191	1.613	3.009	0.156
$\|AL\| < 1.5AU$			2	0.035	-1.090	1.820	-0.458
			3	0.031	1.705	-	-
$+1 < B_y < +4$	139	189	0	-0.045	-	14.918	-
$-4 \leq B_z \leq +1$			1	0.215	1.348	3.451	0.299
$\|AL\| < 1.5AU$			2	0.016	1.736	0.459	-0.092
			3	0.031	0.880	-	-

Table 3.4 Information about discontinuous curve fits for the group with $-4 \leq B_z \leq +1$. The superscript (1) represent the minimum potential curve fits. The superscript (2) represent the maximum potential curve fits.

Categories	Number of Points		Boundary Interval		$AU_{ave}^{(1)}$	$AU_{ave}^{(2)}$	n	$A_n^{(1)}$	$\phi_n^{(1)}$	$B_n^{(1)}$	$\theta_n^{(1)}$	$A_n^{(2)}$	$\phi_n^{(2)}$	$B_n^{(2)}$	$\theta_n^{(2)}$
	$N^{(1)}$	$N^{(2)}$	$LT^{(1)}$	$LT^{(2)}$	(nT)	(nT)		(kV/nT)	(rad.)	(deg.)	(rad.)	(kV/nT)	(rad.)	(deg.)	(rad.)
$B_y \leq$ -4	74	64	11.2	22.3	175	183	0	-0.011	-	21.362	-	0.155	-	14.144	-
$-4 \leq B_z \leq +1$	(70)	(60)	22.8	11.2			1	0.341	1.507	6.098	0.859	0.108	1.423	2.693	-0.078
$\|AL\| \geq$ 1.5AU							2	0.010	0.695	0.375	1.216	0.013	0.013	0.431	-0.335
							3	0.014	-1.732	-	-	0.031	0.804	-	-
$-4 < B_y < +4$	125	117	11.4	23.8	190	193	0	-0.057	-	19.269	-	0.091	-	16.624	-
$-4 \leq B_z \leq +1$	(115)	(109)	23.7	10.5			1	0.222	1.521	5.609	0.690	0.131	1.110	2.151	-0.810
$\|AL\| \geq$ 1.5AU							2	0.013	1.289	0.818	1.329	0.006	-0.025	0.144	2.058
							3	0.013	-0.319	-	-	0.012	1.103	-	-
$B_y \geq +4$	106	103	9.9	23.7	187	170	0	-0.248	-	13.864	-	0.082	-	17.537	-
$-4 \leq B_z \leq +1$	(98)	(95)	22.4	10.1			1	0.061	0.859	3.454	-0.357	0.178	0.942	1.270	-0.755
$\|AL\| \geq$ 1.5AU							2	0.016	2.234	0.778	1.053	0.003	2.641	0.067	1.053
							3	0.043	0.195	-	-	0.007	-2.807	-	-
$B_y \leq$ -4	127	116	12.7	1.4	183	183	0	-0.033	-	19.813	-	0.124	-	12.132	-
$-4 \leq B_z \leq +1$	(117)	(108)	0.6	13.5			1	0.281	1.691	5.170	0.937	0.076	2.182	3.082	0.062
$\|AL\| <$ 1.5AU							2	0.008	1.353	0.162	1.903	0.005	-0.309	0.126	2.264
							3	0.012	-0.441	-	-	0.011	1.608	-	-
$-4 < B_y < +4$	187	153	12.1	0.8	192	197	0	-0.111	-	18.892	-	0.134	-	14.326	-
$-4 \leq B_z \leq +1$	(173)	(141)	23.3	11.1			1	0.123	1.388	5.616	0.091	0.013	1.315	3.076	0.180
$\|AL\| <$ 1.5AU							2	0.005	-2.924	0.558	1.597	0.005	1.325	0.123	-0.989
							3	0.009	1.474	-	-	0.009	2.873	-	-
$B_y \geq +4$	105	105	9.7	0.8	182	175	0	-1.178	-	13.695	-	0.087	-	18.499	-
$-4 \leq B_z \leq +1$	(97)	(97)	23.4	10.8			1	0.155	1.205	4.522	0.240	0.092	1.268	3.587	-1.048
$\|AL\| <$ 1.5AU							2	0.015	0.721	0.823	0.885	0.010	-1.007	0.211	1.855
							3	0.009	-1.021	-	-	0.018	0.487	-	-

Table 3.5 Information about discontinuous curve fits for the group with $B_z < -4$. The representation of superscript is the same as that in Table 3.4.

Categories	Number of Points		Boundary Interval		$AU_{ave}^{(1)}$	$AU_{ave}^{(2)}$	n	$A_n^{(1)}$	$\phi_n^{(1)}$	$B_n^{(1)}$	$\theta_n^{(1)}$	$A_n^{(2)}$	$\phi_n^{(2)}$	$B_n^{(2)}$	$\theta_n^{(2)}$
	$N^{(1)}$	$N^{(2)}$	$LT^{(1)}$	$LT^{(2)}$	(nT)	(nT)		(kV/nT)	(rad.)	(deg.)	(rad.)	(kV/nT)	(rad.)	(deg.)	(rad.)
$B_y \leq -4$	34	34	10.8	3.6	285	266	0	-0.050	-	22.072	-	-0.003	-	14.533	-
$B_z < -4$	(32)	(32)	0.2	12.3			1	0.179	1.506	3.267	0.823	0.261	2.048	3.117	0.829
$\|AL\| \geq 1.5AU$							2	0.012	0.252	0.978	1.280	0.004	-2.175	0.245	0.301
							3	0.024	-1.491	-	-	0.006	0.085	-	-
$-4 < B_y < +4$	93	89	13.4	0.5	260	258	0	-0.030	-	23.801	-	0.084	-	18.582	-
$B_z < -4$	(87)	(83)	0.3	11.2			1	0.220	1.470	8.397	1.000	0.164	1.299	2.173	-1.566
$\|AL\| \geq 1.5AU$							2	0.005	0.472	0.601	2.061	0.009	-1.928	0.133	1.110
							3	0.009	-0.801	-	-	0.016	-0.634	-	-
$B_y \geq +4$	41	37	10.3	22.3	298	314	0	-0.085	-	19.192	-	0.059	-	20.215	-
$B_z < -4$	(39)	(35)	22.6	10.6			1	0.208	1.141	5.763	0.670	0.136	1.088	3.894	-2.229
$\|AL\| \geq 1.5AU$							2	0.004	-2.235	0.883	0.726	0.010	0.483	0.563	3.023
							3	0.006	-2.605	-	-	0.015	1.476	-	-
$B_y \leq -4$	28	26	13.4	0.0	393	392	0	0.010	-	23.066	-	0.126	-	16.647	-
$B_z < -4$	(26)	(24)	0.0	10.4			1	0.211	1.662	5.614	0.733	0.045	2.665	3.846	-0.789
$\|AL\| < 1.5AU$							2	0.013	1.821	0.324	1.192	0.009	-0.823	0.181	-2.286
							3	0.043	0.160	-	-	0.022	0.963	-	-
$-4 < B_y < +4$	38	34	12.7	23.9	331	339	0	-0.070	-	22.792	-	-0.005	-	19.265	-
$B_z < -4$	(36)	(32)	0.4	10.4			1	0.127	1.521	10.228	1.013	0.139	1.478	3.777	-1.002
$\|AL\| < 1.5AU$							2	0.017	1.578	1.177	1.576	0.003	2.818	0.676	1.418
							3	0.015	0.083	-	-	0.008	-2.353	-	-
$B_y \geq +4$	27	22	12.2	22.7	357	338	0	-0.176	-	19.664	-	0.076	-	20.386	-
$B_z < -4$	(25)	(22)	21.7	9.2			1	0.042	0.138	7.983	0.608	0.057	1.906	2.564	-1.203
$\|AL\| < 1.5AU$							2	0.004	2.051	0.835	1.095	0.011	-1.447	0.026	2.841
							3	0.008	0.575	-	-	0.018	-1.376	-	-

Table 3.6 Information about discontinuous curve fits for the subgroup with $-4 \leq B_z \leq +1$ and $-4 < B_y < +1$. The representation of superscript is the same as that in Table 3.4.

Categories	Number of Points		Boundary Interval		$AU_{ave}^{(1)}$	$AU_{ave}^{(2)}$	n	$A_n^{(1)}$	$\phi_n^{(1)}$	$B_n^{(1)}$	$\theta_n^{(1)}$	$A_n^{(2)}$	$\phi_n^{(2)}$	$B_n^{(2)}$	$\theta_n^{(2)}$
	$N^{(1)}$	$N^{(2)}$	$LT^{(1)}$	$LT^{(2)}$	(nT)	(nT)		(kV/nT)	(rad.)	(deg.)	(rad.)	(kV/nT)	(rad.)	(deg.)	(rad.)
$-4 < B_y < -1$	41	42	12.7	0.3	195	193	0	-0.021	-	21.721	-	0.149	-	14.679	-
$-4 \leq B_z \leq +1$	(39)	(40)	22.9	11.5			1	0.251	1.484	2.291	0.861	0.068	1.209	2.027	-0.192
$\|AL\| \geq 1.5AU$							2	0.015	1.084	0.577	1.478	0.009	0.896	0.135	-2.860
							3	0.026	-0.656	-	-	0.015	1.764	-	-
$-1 \leq B_y \leq +1$	31	26	11.8	0.0	190	198	0	-0.083	-	21.535	-	0.024	-	16.604	-
$-4 \leq B_z \leq +1$	(29)	(24)	0.7	10.0			1	0.188	1.481	8.179	1.045	0.181	1.208	1.226	-0.901
$\|AL\| \geq 1.5AU$							2	0.011	1.942	2.007	1.597	0.003	0.057	0.209	1.341
							3	0.014	1.547	-	-	0.005	0.799	-	-
$+1 < B_y < +4$	53	49	10.1	23.4	186	190	0	-0.092	-	17.392	-	0.059	-	18.781	-
$-4 \leq B_z \leq +1$	(49)	(47)	22.8	10.5			1	0.196	1.617	4.078	0.451	0.177	1.028	3.349	-1.363
$\|AL\| \geq 1.5AU$							2	0.019	1.061	0.882	1.369	0.008	0.105	0.217	1.703
							3	0.012	-0.352	-	-	0.016	0.907	-	-
$-4 < B_y < -1$	70	65	12.9	0.9	200	203	0	-0.084	-	19.061	-	0.123	-	14.035	-
$-4 \leq B_z \leq +1$	(66)	(61)	0.1	11.1			1	0.132	1.587	3.832	0.681	0.039	1.484	3.987	-0.008
$\|AL\| < 1.5AU$							2	0.009	-2.517	0.174	2.177	0.011	1.313	0.245	-1.518
							3	0.015	2.449	-	-	0.017	3.105	-	-
$-1 \leq B_y \leq +1$	38	28	12.1	0.5	184	201	0	-0.094	-	21.111	-	0.019	-	15.798	-
$-4 \leq B_z \leq +1$	(36)	(26)	22.8	12.0			1	0.149	1.265	8.901	1.126	0.123	1.868	2.076	-0.701
$\|AL\| < 1.5AU$							2	0.021	-2.435	0.334	2.114	0.018	-1.207	0.301	-2.661
							3	0.022	1.906	-	-	0.015	0.786	-	-
$+1 < B_y < +4$	79	60	11.5	0.6	188	190	0	-0.118	-	16.339	-	0.122	-	16.940	-
$-4 \leq B_z \leq +1$	(73)	(56)	23.3	9.8			1	0.137	1.291	4.986	0.572	0.027	0.937	2.294	-0.631
$\|AL\| < 1.5AU$							2	0.012	1.842	1.500	1.543	0.006	1.480	0.140	1.361
							3	0.019	0.722	-	-	0.009	2.780	-	-

3.3.3 Functions to Represent the Boundary Locations

Various models of ionospheric convection have been presented in the past. Most of the models considered the convection reversal to be circular and continuous. Very few models [*Moses et al.*, 1987; *Heppner and Maynard*, 1987] addressed the discontinuous convection reversals, which allow a gap near noon or midnight. In this thesis the variation of the location of the convection reversals is emphasized. The location of convection reversal boundary has been determined observationally and also plotted against the MLT, as shown in Figures 3.14 - 3.25. Similarly, the plus and diamond symbols represent the location of maximum and minimum potentials, respectively. Very few maximum points were found near the equatorward of the cusp region (between the latitude 60° and 70°). These points belong to an additional convection reversal, which is separated from the dawn-cell convection reversal. These points were not used for the fitting of the boundary location, as these points are not concerned with the primary convection reversals. This additional convection reversal might be related to the conductivity enhancement due to the precipitation of particles from lower latitude boundary layer.

From comparing the colatitude of the minimum potential points near premidnight both in categories ($B_y \geq +4$) and in categories ($B_y \leq -4$), more scattering was found in categories ($B_y \geq +4$), and the data points seem to be separated into two convection reversals. One of the convection reversals goes equatorward, extending it across the noon-midnight meridian, the other goes poleward, but it is shorter. In this study only absolute maximum and minimum potentials were used when there are multiple reversals in the measurement. This may result in the missing of some local maximum or minimum potentials. Thus, it is inappropriate to fit the data into two branches now. This work will be left until all the local maximum and minimum potentials are determined in the future.

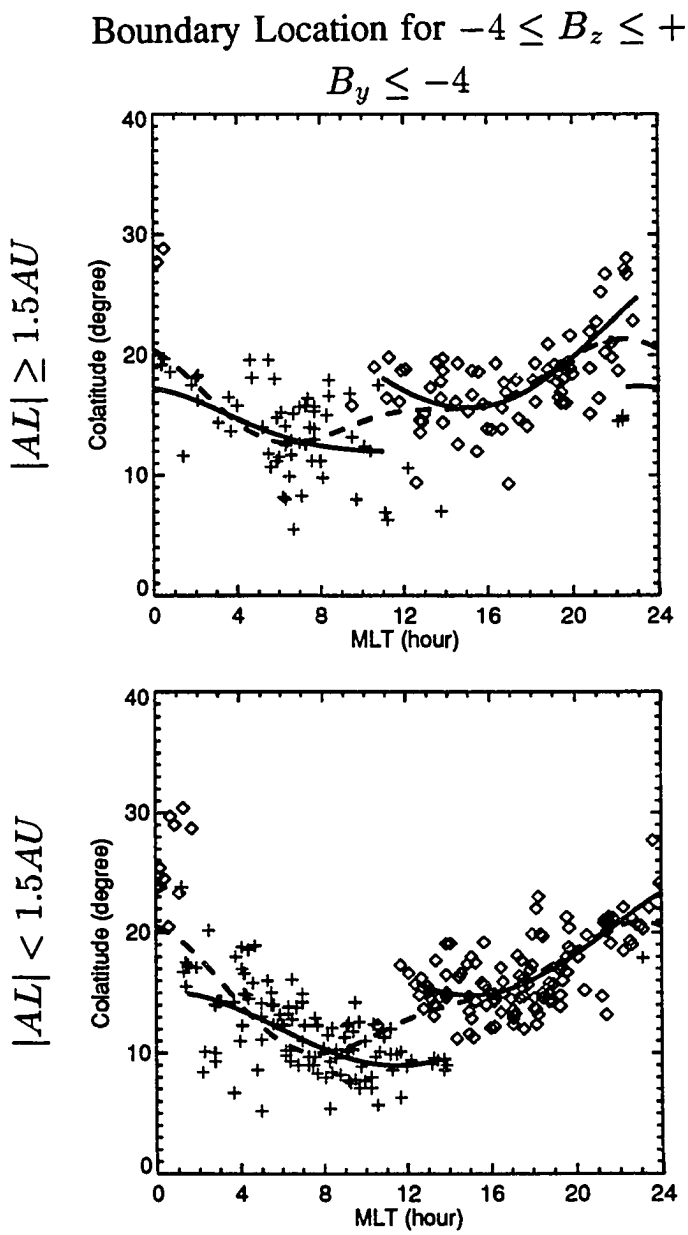

Figure 3.14 Location of the convection reversal boundary for the subgroup with $-4 \leq B_z \leq +1$ and $B_y \leq -4$. The upper graph shows the data points under an intense electrojet and the lower graph shows the data points under a weak electrojet. The plus symbols represent dawn/maximum potential points and the diamond symbols represent dusk/minimum potential points. These points were fit separately (solid lines) and together (dash lines).

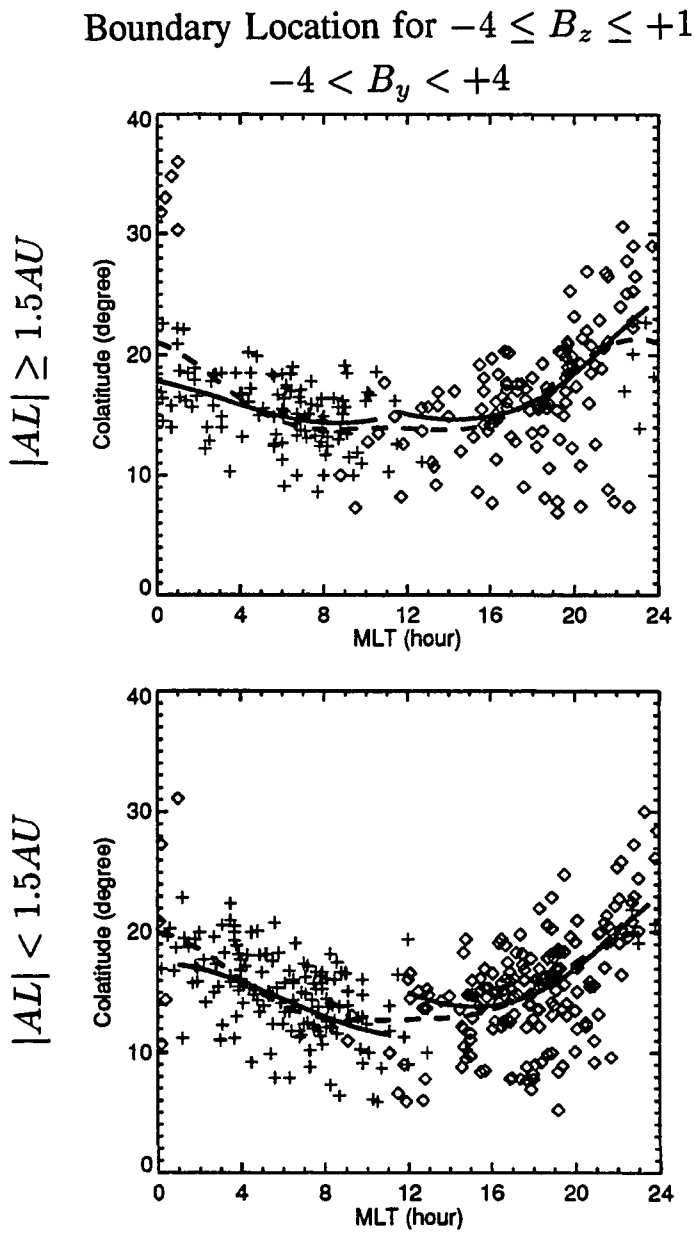

Figure 3.15 Location of the convection reversal boundary for the subgroup with $-4 \leq B_z \leq +1$ and $-4 < B_y < +4$. The representation of lines and symbols is the same as that in Figure 3.14.

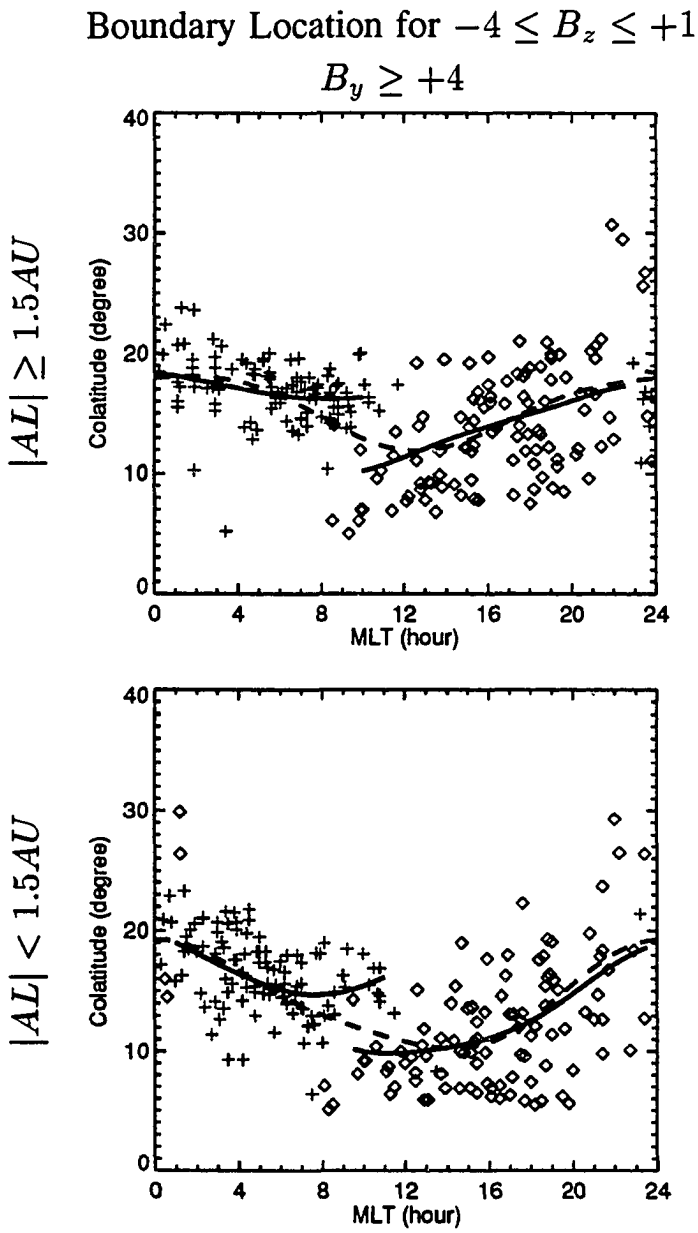

Figure 3.16 Location of the convection reversal boundary for the subgroup with $-4 \leq B_z \leq +1$ and $B_y \geq +4$. The representation of lines and symbols is the same as that in Figure 3.14.

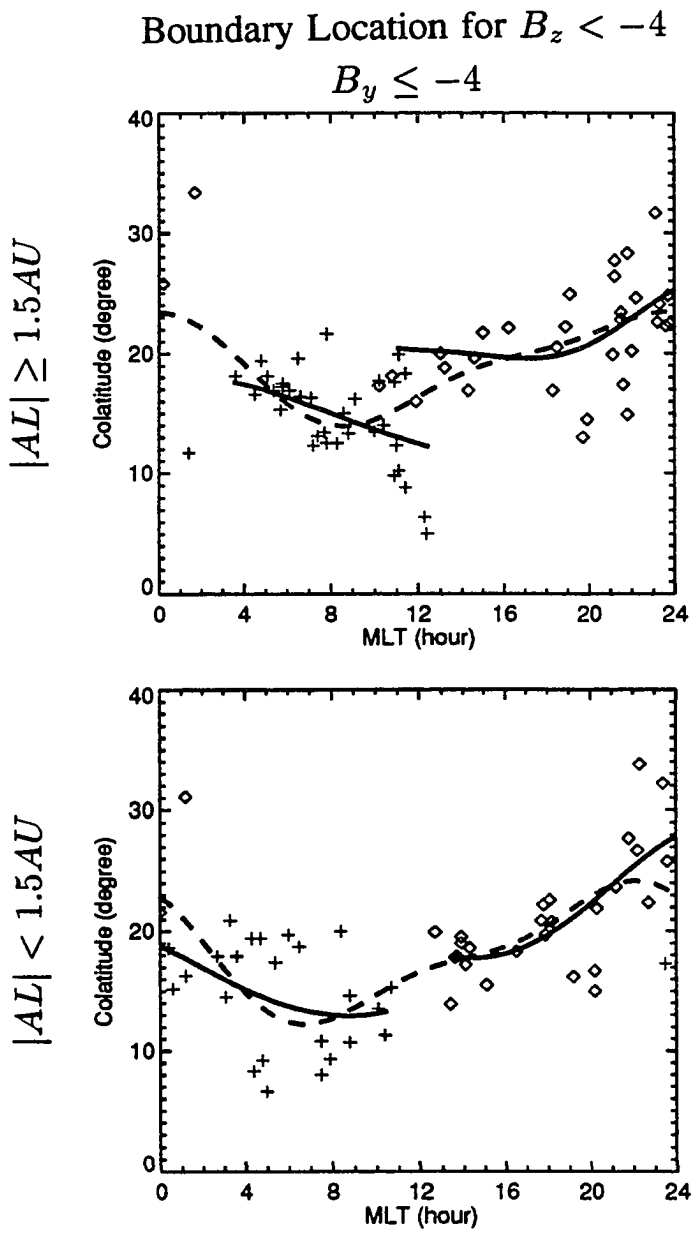

Figure 3.17 Location of the convection reversal boundary for the subgroup with $B_z < -4$ and $B_y \leq -4$. The representation of lines and symbols is the same as that in Figure 3.14.

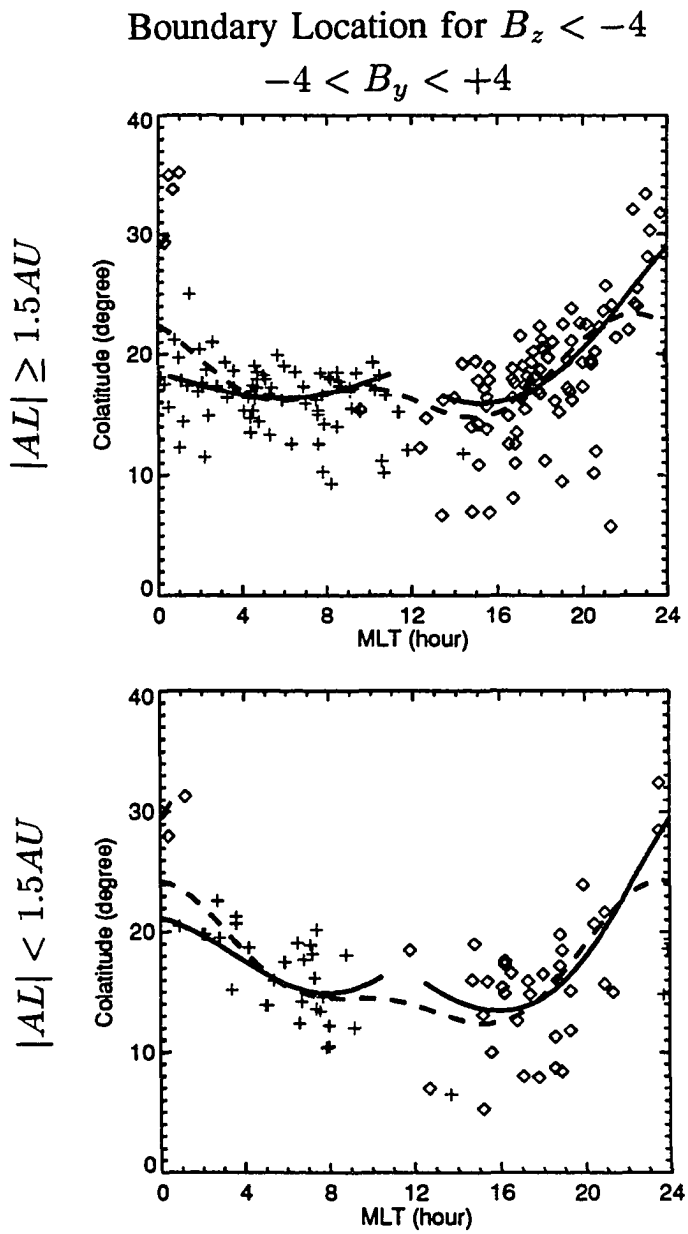

Figure 3.18 Location of the convection reversal boundary for the subgroup with $B_z < -4$ and $-4 < B_y < +4$. The representation of lines and symbols is the same as that in Figure 3.14.

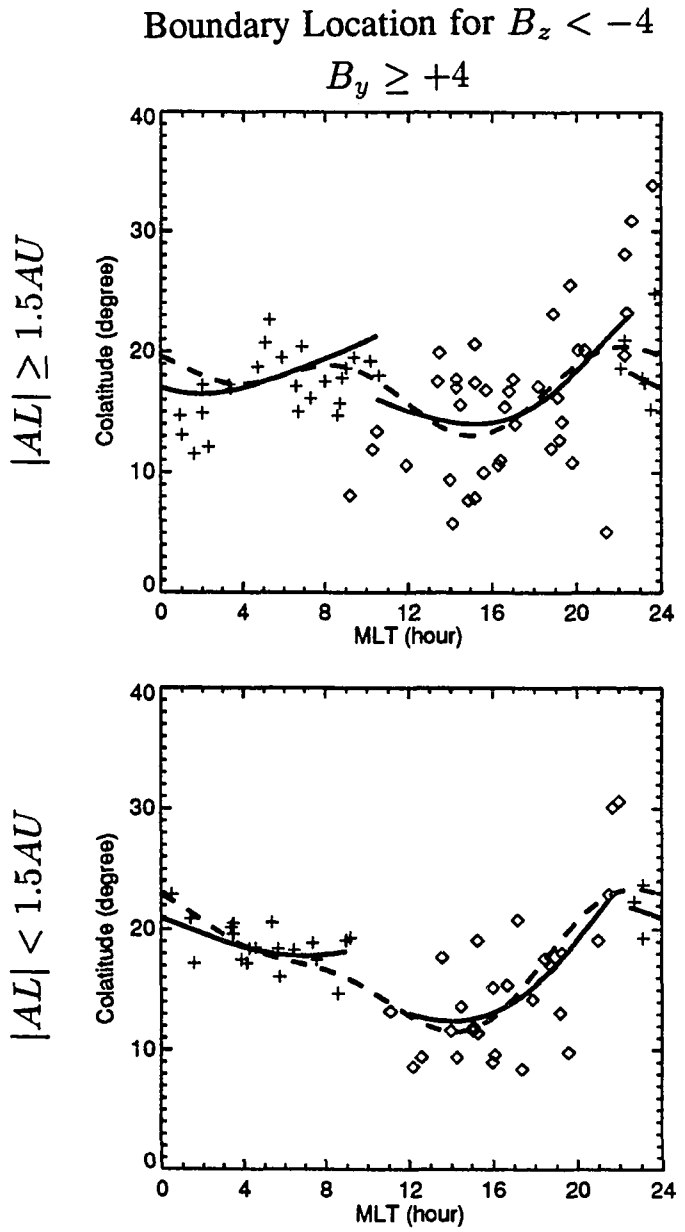

Figure 3.19 Location of the convection reversal boundary for the subgroup with $B_z < -4$ and $B_y \geq +4$. The representation of lines and symbols is the same as that in Figure 3.14.

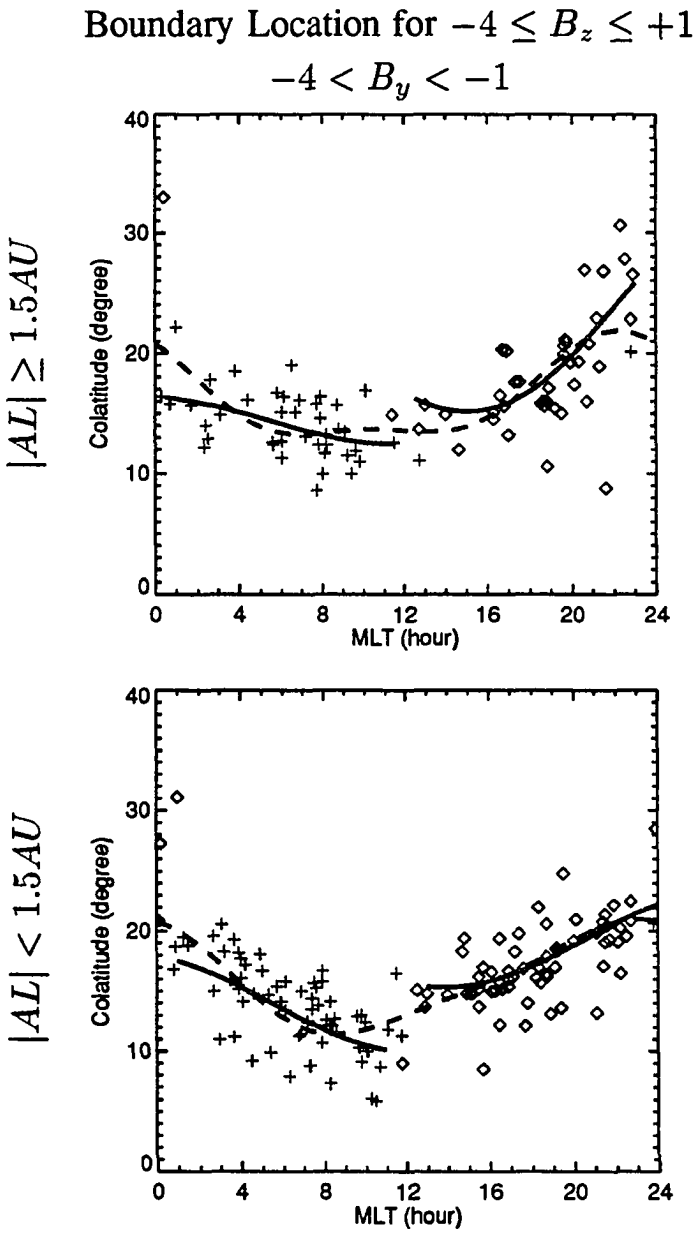

Figure 3.20 Location of the convection reversal boundary for the subgroup with $-4 \leq B_z \leq +1$ and $-4 < B_y < -1$. The representation of lines and symbols is the same as that in Figure 3.14.

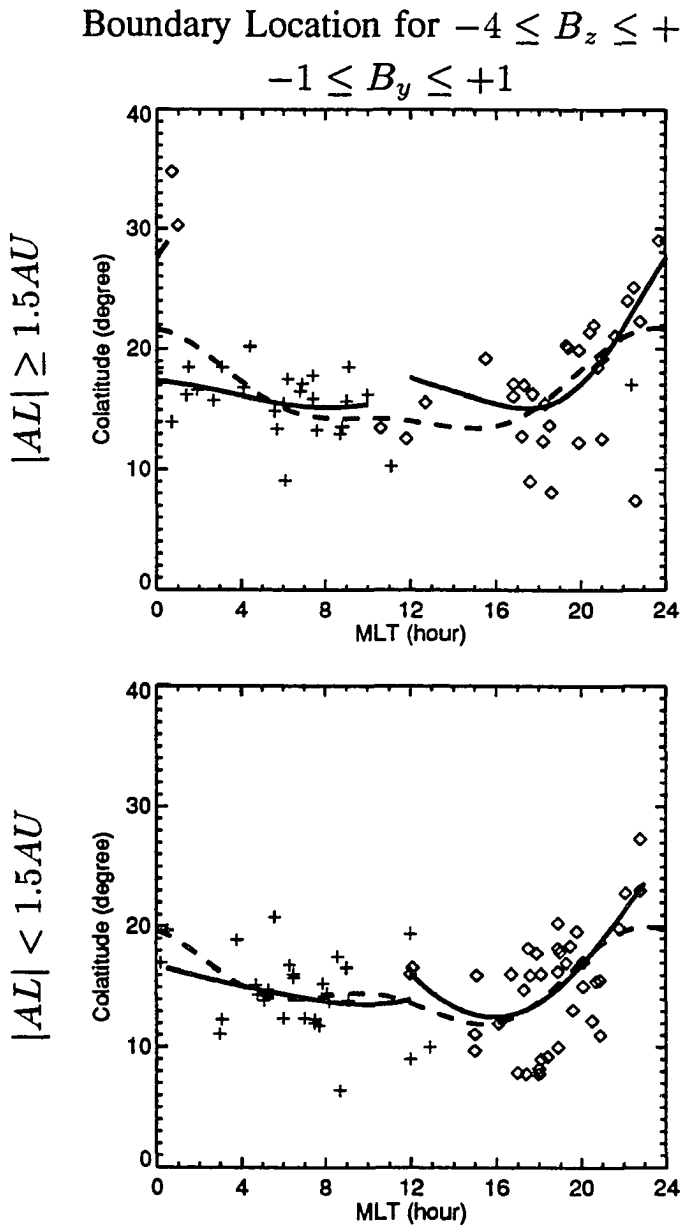

Figure 3.21 Location of the convection reversal boundary for the subgroup with $-4 \leq B_z \leq +1$ and $-1 \leq B_y \leq +1$. The representation of lines and symbols is the same as that in Figure 3.14.

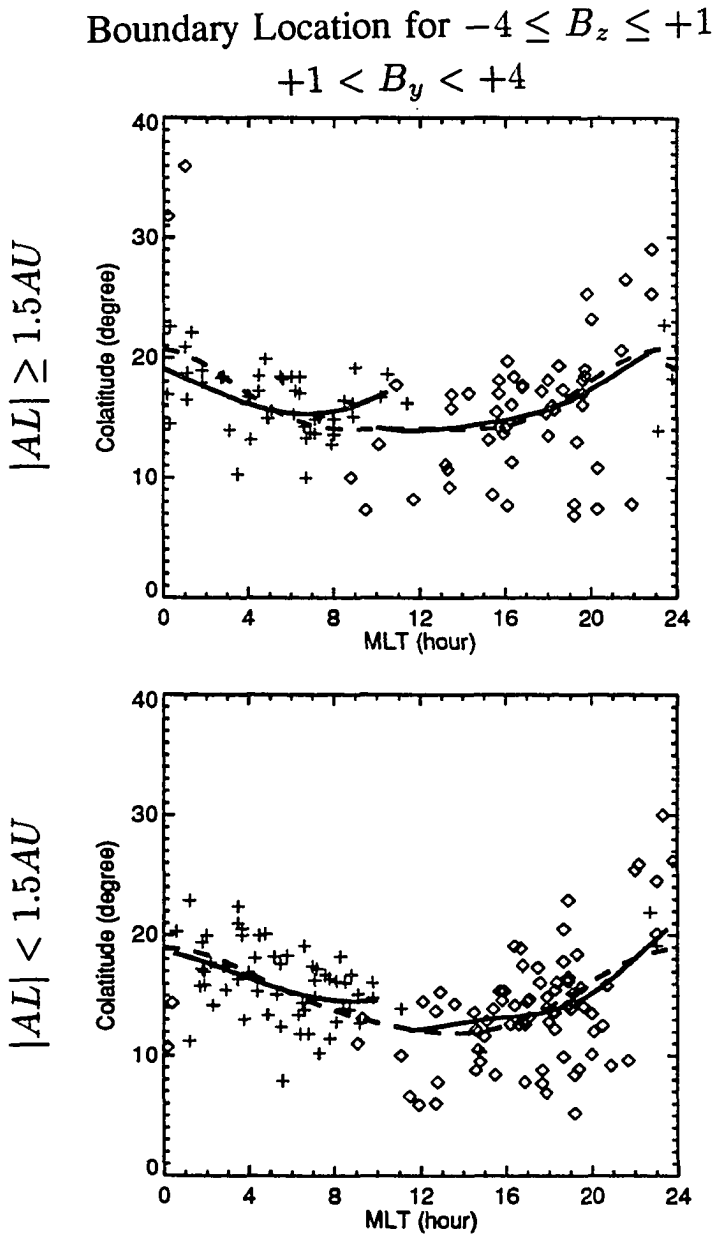

Figure 3.22 Location of the convection reversal boundary for the subgroup with $-4 \leq B_z \leq +1$ and $+1 < B_y < +4$. The representation of lines and symbols is the same as that in Figure 3.14.

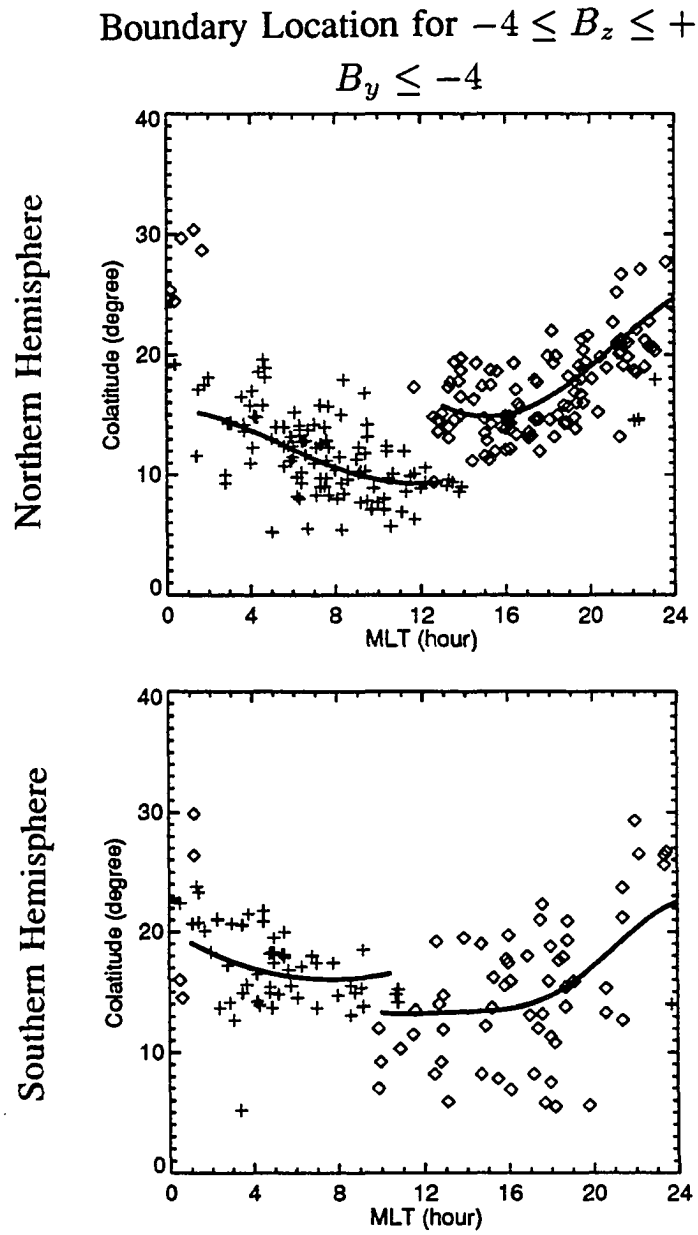

Figure 3.23 Location of the convection reversal boundary for the subgroup with $-4 \leq B_z \leq +1$ and $B_y \leq -4$. The upper graph shows the data points in the northern hemisphere and the lower graph shows the data points in the southern hemisphere. The plus symbols represent dawn/maximum potential points and the diamond symbols represent dusk/minimum potential points. These points were fit separately (solid lines).

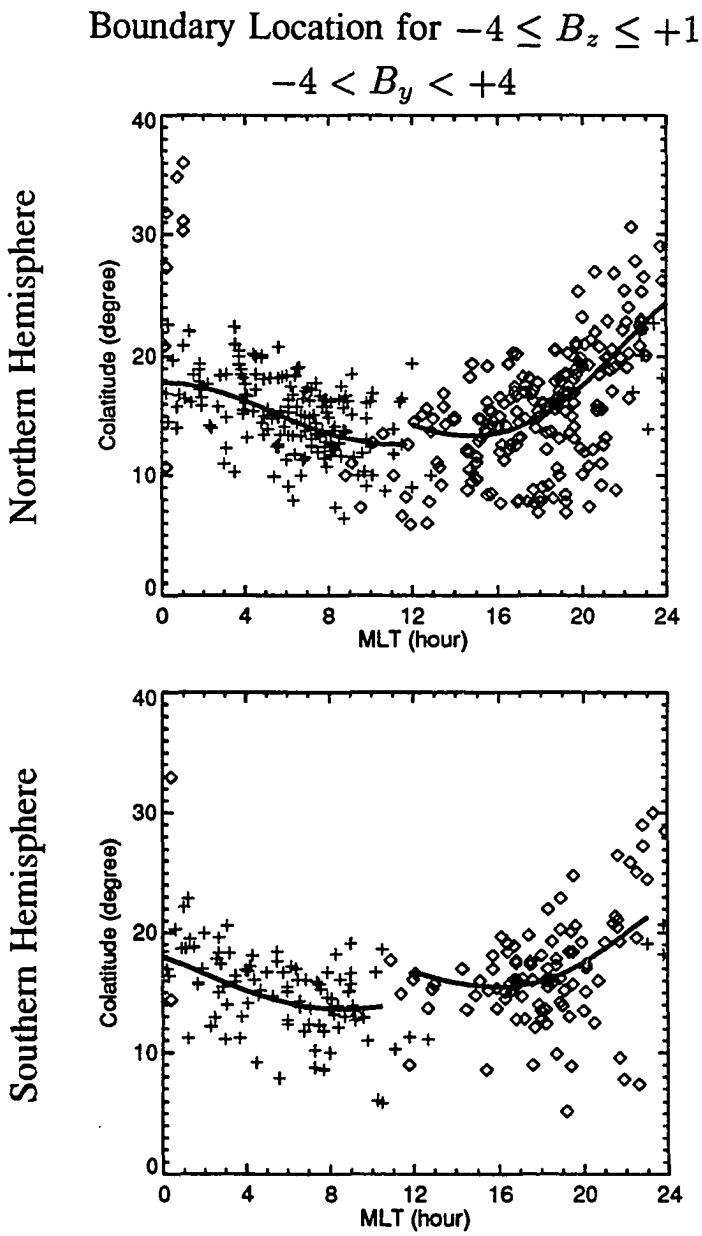

Figure 3.24 Location of the convection reversal boundary for the subgroup with $-4 \leq B_z \leq +1$ and $-4 < B_y < +4$. The representation of lines and symbols is the same as that in Figure 3.23.

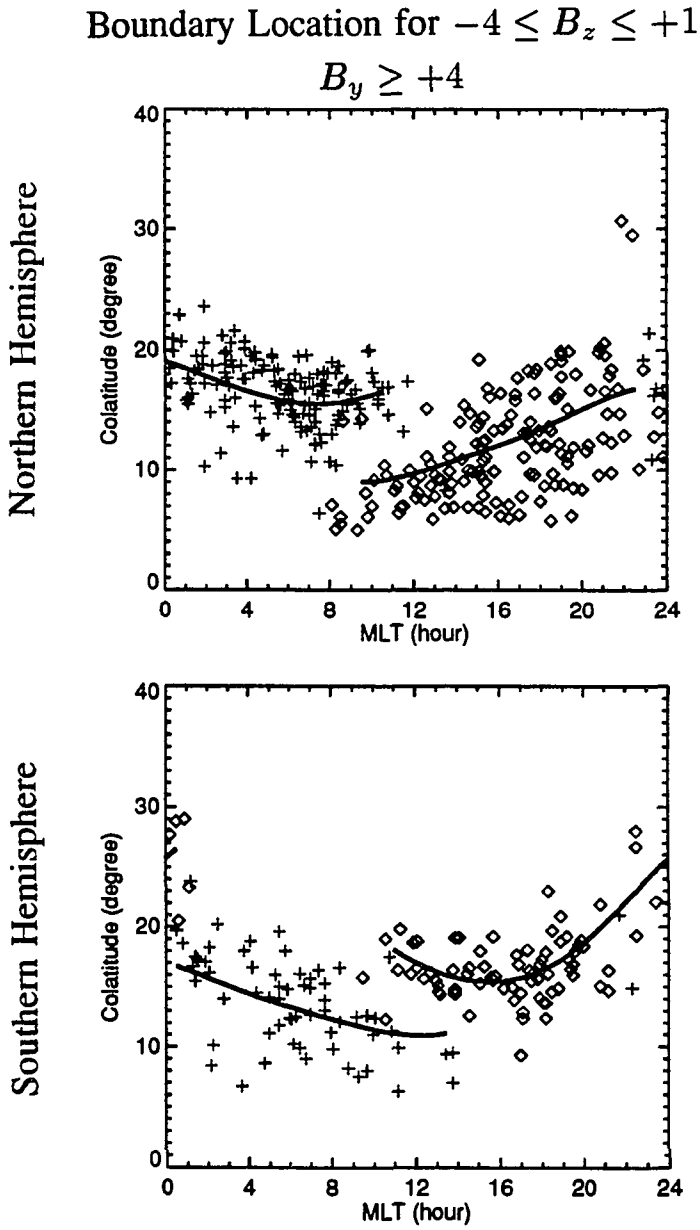

Figure 3.25 Location of the convection reversal boundary for the subgroup with $-4 \leq B_z \leq +1$ and $B_y \geq +4$. The representation of lines and symbols is the same as that in Figure 3.23.

The boundary colatitudes, f_c, were also fit in a form

$$f_c(MLT) = B_0 + \sum_{n=1}^{N} B_n \cos[\frac{n\pi}{12} MLT - \theta_n] \tag{3.3}$$

where B_0, B_n, and θ_n are the coefficients to be determined by the approach mentioned in Subsection 3.3.1. The values of these coefficients are listed in Tables 3.1-3.3. A termination of the series at $n = 2$ produced a satisfactory match between the series representation and the data points. The fitting curves are shown as the dash lines in Figures 3.14 - 3.25. From looking at the data points near noon or midnight, the colatitude distribution does not appear to be a continuous, single-value function. Thus, the same curve-fitting process have been repeated, but fitting the colatitude of the maximum and minimum potential separately. This may lead to the crossing of the two potential segments near noon or midnight. To avoid this, 92% of the data points have been used, with 4% of data points cut from each end of the maximum and minimum potential segments. The values of these coefficients are listed in Tables 3.4-3.6. The results are shown as the solid lines in Figures 3.14 - 3.25.

CHAPTER 4

Reproduction of the Ionospheric Convection Patterns

The results of fitting the random measurements of the boundary potentials and locations with a Fourier series representations have been shown in the previous chapter. In this form it is difficult to comprehend the fitting curves. For the purpose of easier visualization of the results, the boundary fit has been used as the boundary conditions of a model to calculate the illustrative ionospheric convection pattern. Note that some simplifying assumptions were used in the model. In this chapter the description of the models will be stated first. Following this, the resulting convection patterns will be shown.

4.1 A Simple Model for Solving Laplace Equation

In this section the electrodynamics of ionospheric convection and the main equation of the model are discussed briefly. The ionospheric convection is mainly driven by the electric fields, which are generated at the magnetopause due to the solar wind-magnetosphere interaction and transmitted along the magnetic field lines between the ionosphere and the magnetosphere. The field-aligned currents flow from the magnetosphere and connect with the horizontal currents in the lower ionosphere to form a closed current system by the coupling between the magnetosphere and ionosphere. The entire current system must satisfy the current continuity equation in MHD approximation

$$\nabla \cdot \mathbf{J} \simeq 0 \tag{4.1}$$

where $\mathbf{J}$ is the current density. The divergence of current can generate a charge density, then the electric field builds up quickly to balance the divergence of current. In most cases the

equation (4.1) is used to calculate the electric field rather than Poisson's equation. The equation (4.1) can be rewritten to

$$\nabla \cdot \mathbf{I} = j_{\parallel} \tag{4.2}$$

where $j_{\parallel}$ is the density of the field-aligned current (positive for a downward current) and $\mathbf{I_i}$ is the horizontal current in the ionosphere. The relationship among electric field, current, and conductivity are related by Ohm's law with Hall and Pedersen conductivities separated

$$\mathbf{I_i} = \Sigma_P \mathbf{E} + \Sigma_H \mathbf{B_0} \times \mathbf{E} \tag{4.3}$$

where Σ_H and Σ_P are the height-integrated Hall and Pedersen conductivities, B_0 is a unit vector of magnetic field, and E is the ionospheric electric. Since the magnetic field in a high-latitude region is nearly vertical and points downward, the unit vector of the magnetic field is in $-z$ direction. Combining (4.2), (4.3), we have

$$\nabla \cdot [\Sigma_P \mathbf{E} + \Sigma_H \mathbf{B_0} \times \mathbf{E}] = j_{\parallel}. \tag{4.4}$$

Faraday's law in steady state is

$$\nabla \times \mathbf{E} = 0. \tag{4.5}$$

The electric field is assumed to be curl-free, which is described by

$$\mathbf{E} = -\nabla \Phi. \tag{4.6}$$

The electric field is perpendicular to a line of constant potential and is also perpendicular to $\mathbf{E} \times \mathbf{B}$ motion of plasma. Thus, the plasma flows along lines of constant potential and a pattern

of equipotential also represents the plasma flow pattern. Substituting (4.6) into (4.4), we have

$$\nabla \cdot [\Sigma_P \nabla \Phi + \Sigma_H \mathbf{B_0} \times \nabla \Phi] = -j_{\parallel} \tag{4.7}$$

or

$$\Sigma_P \nabla^2 \Phi + \nabla \Sigma_P \cdot \nabla \Phi + \nabla \Sigma_H \cdot (\mathbf{B_0} \times \nabla \Phi) = -j_{\parallel}. \tag{4.8}$$

The field-aligned currents provide the connection between the ionosphere and the magnetosphere. *Iijima and potemra* [1976, 1978] have shown that the field-aligned current in solar wind-magnetosphere-ionosphere coupling system can be classified into region 1 and region 2 current systems. The region 1 field-aligned current flows into the ionosphere on the dawnside and out of the ionosphere on the duskside while the region 2 field-aligned current flows into the ionosphere on the duskside and out of the ionosphere on the dawnside. The intensity of the region 1 current is greater than the intensity of the region 2 current by a factor of 2 or more. They also used Triad satellite data to study large-scale characteristics of field-aligned currents associated with substorms and have shown that the intensity of the field-aligned current increases during substorms. *Fujii et al.* [1981] found that the dayside region 1 field-aligned current is higher in the summer hemisphere than that in the winter hemisphere. *Fujii and Iijima* [1987] have shown that the field-aligned current of region 1 and region 2 depends differently on ionospheric conductivity. The region 1 current intensity is linearly proportional to the conductivity at all MLT and the region 2 current also shows a dependence on conductivity, but poor correlation than region 1 current. This implies that region 1 current is primarily driven by a voltage generator and region 2 current seems to be driven by a combination of voltage and current generator.

The convection model to be calculated below consists of two boundaries. One of the boundaries is coincident with the measured convection reversal boundaries. Note that this

boundary condition has implied the region 1 current on the boundary. The other boundary is located at a lower latitude. This low-latitude boundary on the nightside is chosen in circular shape, which is located at 58° for the group ($-4 \leq B_z \leq +1$) and 55° for the group ($B_z < -4$). The low-latitude boundary on the dayside is chosen in elliptic shape, which is chosen as 70° at noon for the group ($-4 \leq B_z \leq +1$) and 65° at noon for the group ($B_z < -4$). These values of latitude are from the models of *Heppner and Maynard* [1987]. The potential value is assumed to be zero around the low-latitude boundary.

For lack of the corresponding observational information on the ionospheric conductivity and the field-aligned current, the following simplifying assumptions are made. First, it has been assumed that the field-aligned current is negligible away from the convection reversal boundary so that the field-aligned current on the right-hand side of (4.8) can be neglected as an approximation. Second, the conductivity gradient is assumed to be small so that the first term on the left-hand side of (4.8) dominates. Thus, the equation (4.8) can be reduced to

$$\nabla^2 \Phi = 0. \tag{4.9}$$

4.2 Illustration of Boundary Potentials and Locations

The equation (4.9) has been solved everywhere in the high-latitude region except at the convection reversal boundary, using the boundary conditions determined by the observation. The numerical scheme is a modified Gauss-Siedel iteration with a successive over-relaxation method. The method of successive over-relaxation can speed up the convergence of iteration. The potentials at the convection reversal boundary remained unchanged during the calculation. At this point the potentials have been multiplied by the mean value of the corrected AU index in order to convert the units back to kV. The iteration terminates when the norm, or sum

of the residual is less than the error per step times the initial value of norm. The details of the numerical scheme for solving Laplace equation in rectangular coordinates are shown in Appendix B.

Although the location of the convection reversal boundary is measured in latitude and MLT, which are in polar coordinates, rectangular coordinates were used in the numerical calculation and plotting. This was done in order to get better convergence at the origin, and for a more convenient interface with the contour plotting software. A comparison between the polar and rectangular coordinates will be shown in Appendix C. The difference is shown to be small. Note that as a consequence of this approach (keeping potentials fixed on the boundary), the points on the convection reversal boundary do not obey (4.9), and all of the region 1 field-aligned currents are concentrated on these points. The region 2 currents are at the lower latitude boundary, which is not realistic.

Figures 4.1 - 4.9 are the illustrative patterns which are calculated from the continuous, single-value functions. The heavy solid lines in each graph show the location of the boundary. For convenience, the maximum and minimum values of the electric potential as well as their difference, are shown at the bottom of each graph. Figures 4.10 - 4.18 are the results which were obtained by using the same procedure, with two separate functions for the positive and negative boundaries. Similarly, the heavy solid lines in each graph show the locations of the boundaries. Comparing the patterns with a continuous and a discontinuous boundaries, the features of premidnight Harang discontinuity and the dayside "throat" near the cusp can be seen from the patterns with a discontinuous boundary.

The upper row in Figures 4.19 - 4.21 show the patterns in the northern hemisphere and the lower row in Figure 4.19 - 4.21 show the patterns in the southern hemisphere. It can be seen that the convection pattern is reversed in response to IMF B_y in opposite hemispheres. Thus,

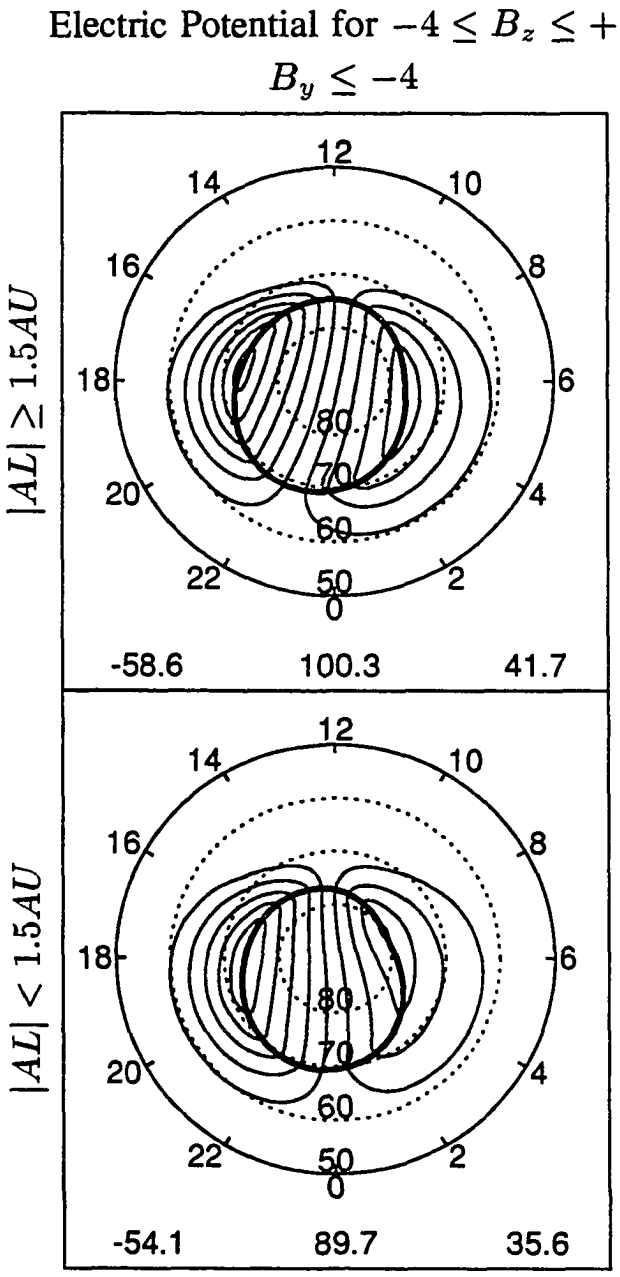

Figure 4.1 Illustration of the continuous convection reversal boundary for the subgroup with $-4 \leq B_z \leq +1$ and $B_y \leq -4$. These patterns were derived by solving the Laplace equation. The thin solid lines represent the equipotential lines and the heavy solid lines represent the convection reversal boundary. The numbers at lower-left and lower-right corners in each graph represent the dusk and dawn potentials, respectively.

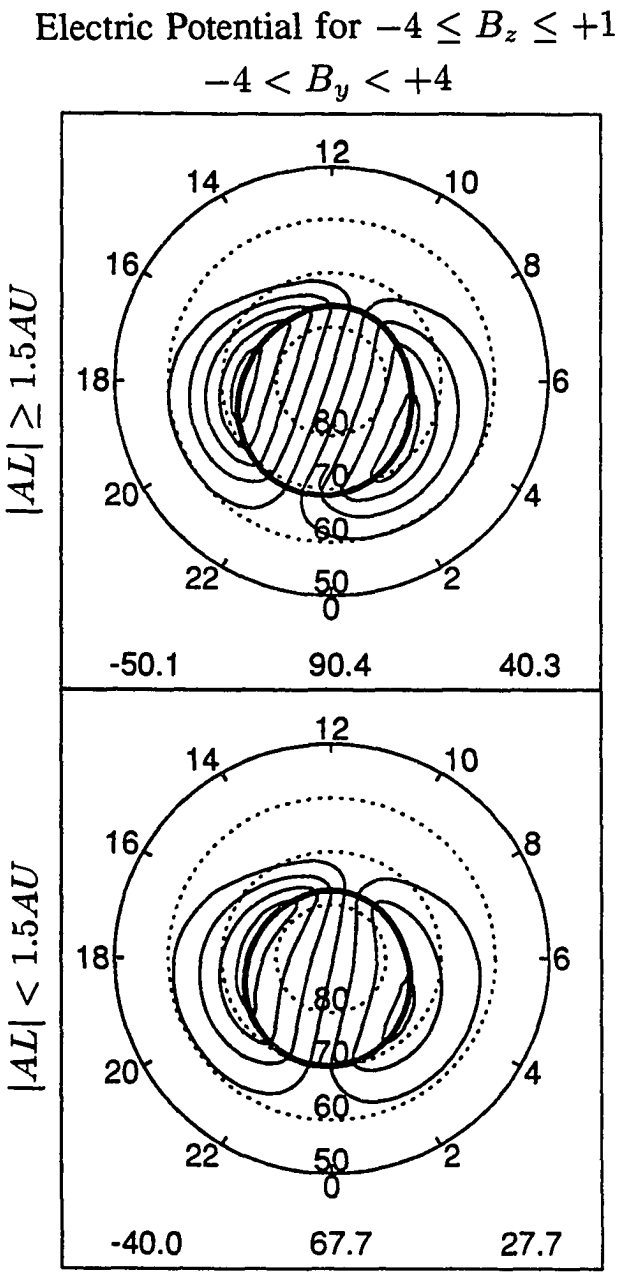

Figure 4.2 Illustration of the continuous convection reversal boundary for the subgroup with $-4 \leq B_z \leq +1$ and $-4 < B_y < +4$. The representation of lines and numbers is the same as that in Figure 4.1.

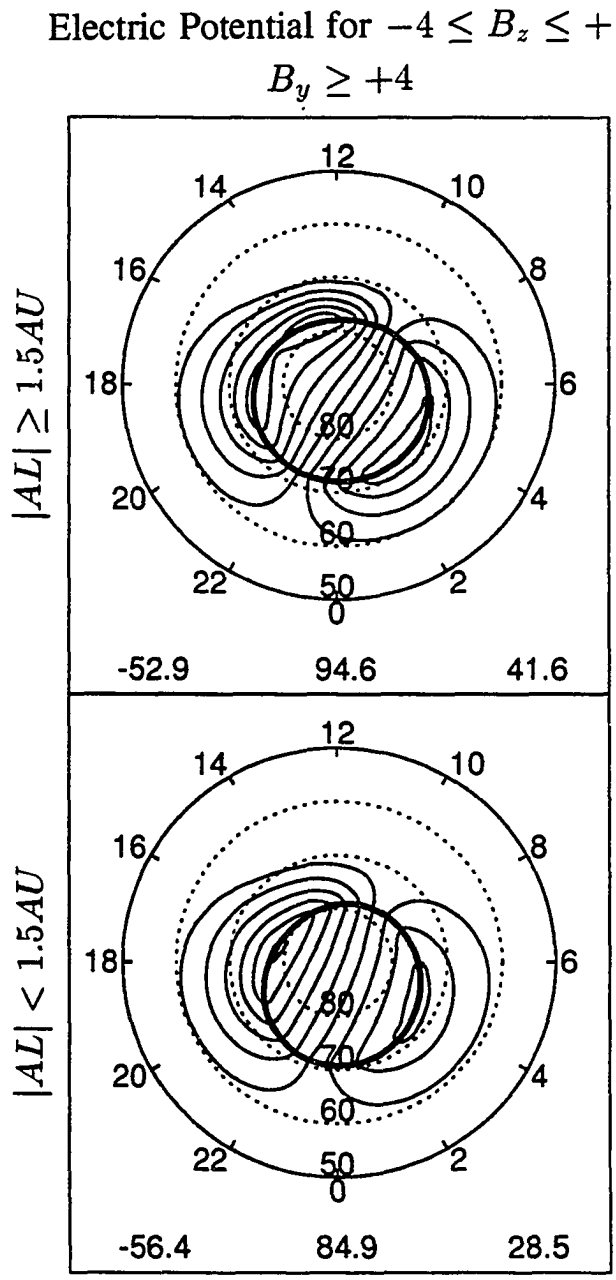

Figure 4.3 Illustration of the continuous convection reversal boundary for the subgroup with $-4 \leq B_z \leq +1$ and $B_y \geq +4$. The representation of lines and numbers is the same as that in Figure 4.1.

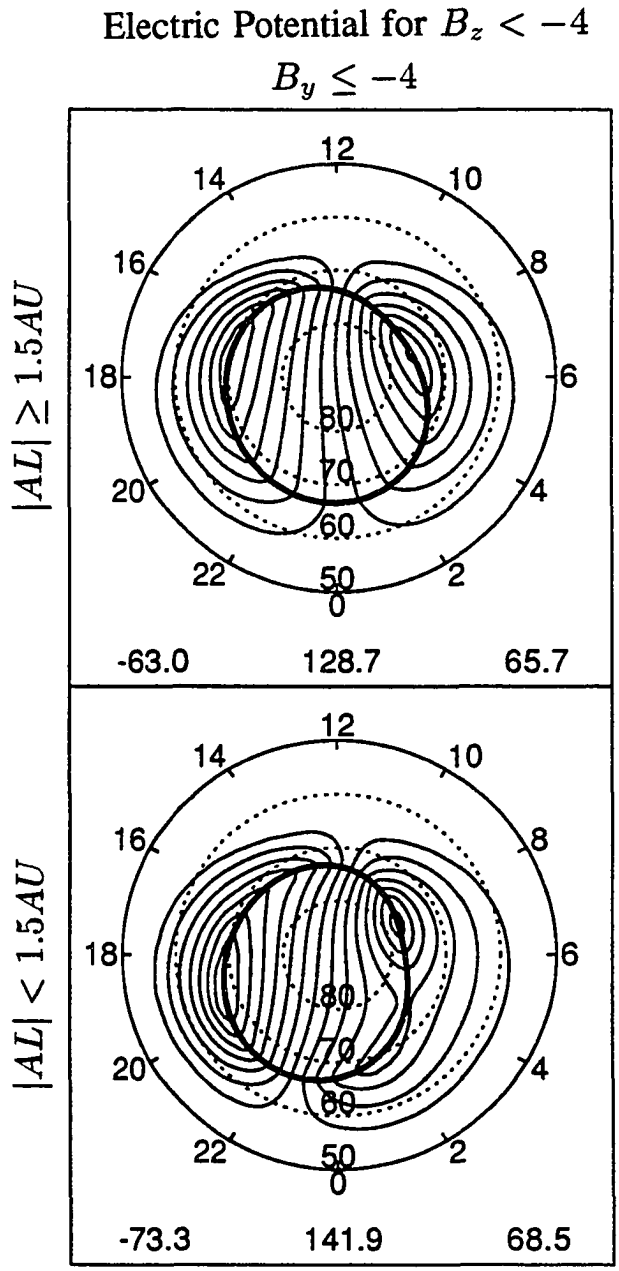

Figure 4.4 Illustration of the continuous convection reversal boundary for the subgroup with $B_z < -4$ and $B_y \leq -4$. The representation of lines and numbers is the same as that in Figure 4.1.

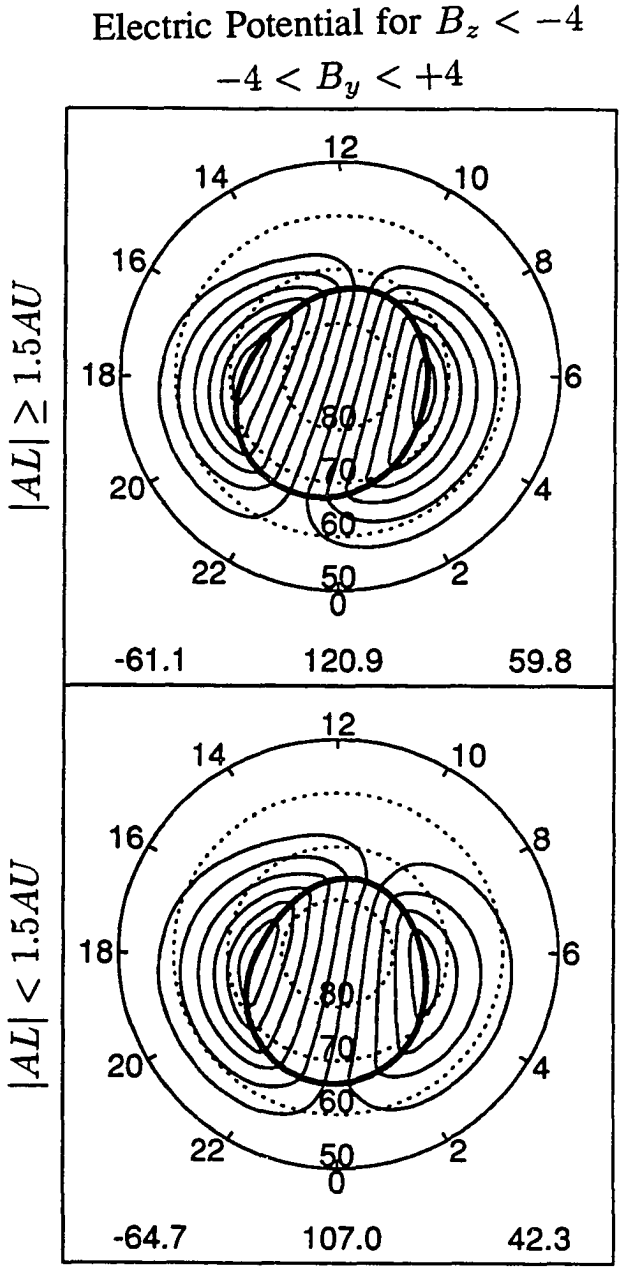

Figure 4.5 Illustration of the continuous convection reversal boundary for the subgroup with $B_z < -4$ and $-4 < B_y < +4$. The representation of lines and numbers is the same as that in Figure 4.1.

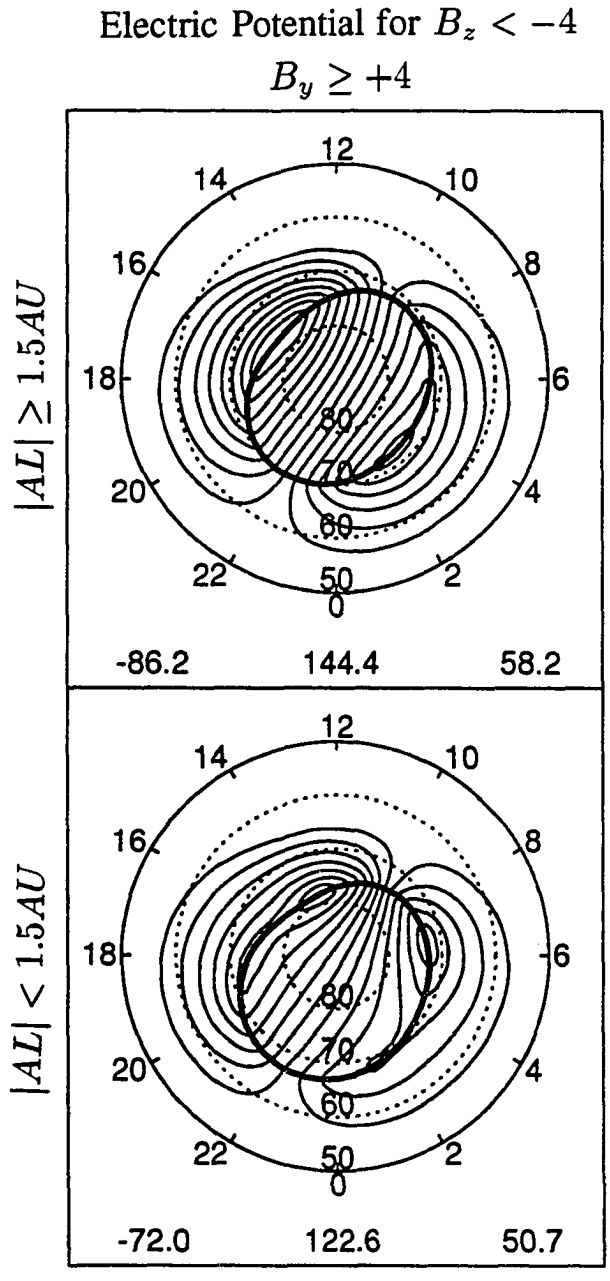

Figure 4.6 Illustration of the continuous convection reversal boundary for the subgroup with $B_z < -4$ and $B_y \geq +4$. The representation of lines and numbers is the same as that in Figure 4.1.

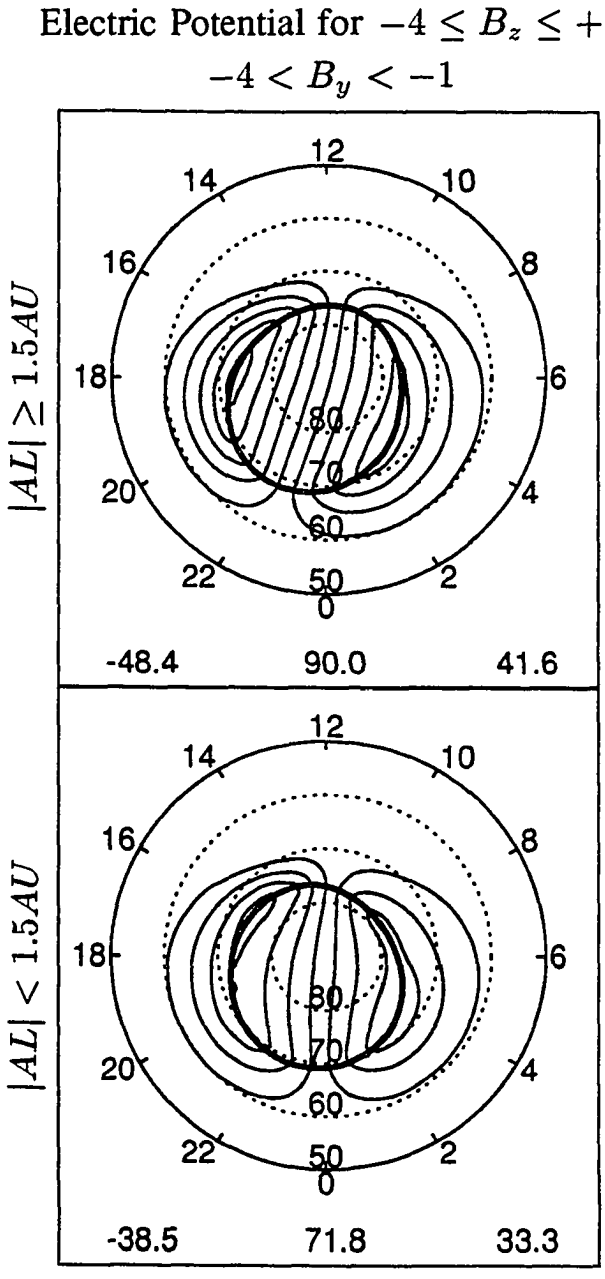

Figure 4.7 Illustration of the continuous convection reversal boundary for the subgroup with $-4 \leq B_z \leq +1$ and $-4 < B_y < -1$. The representation of lines and numbers is the same as that in Figure 4.1.

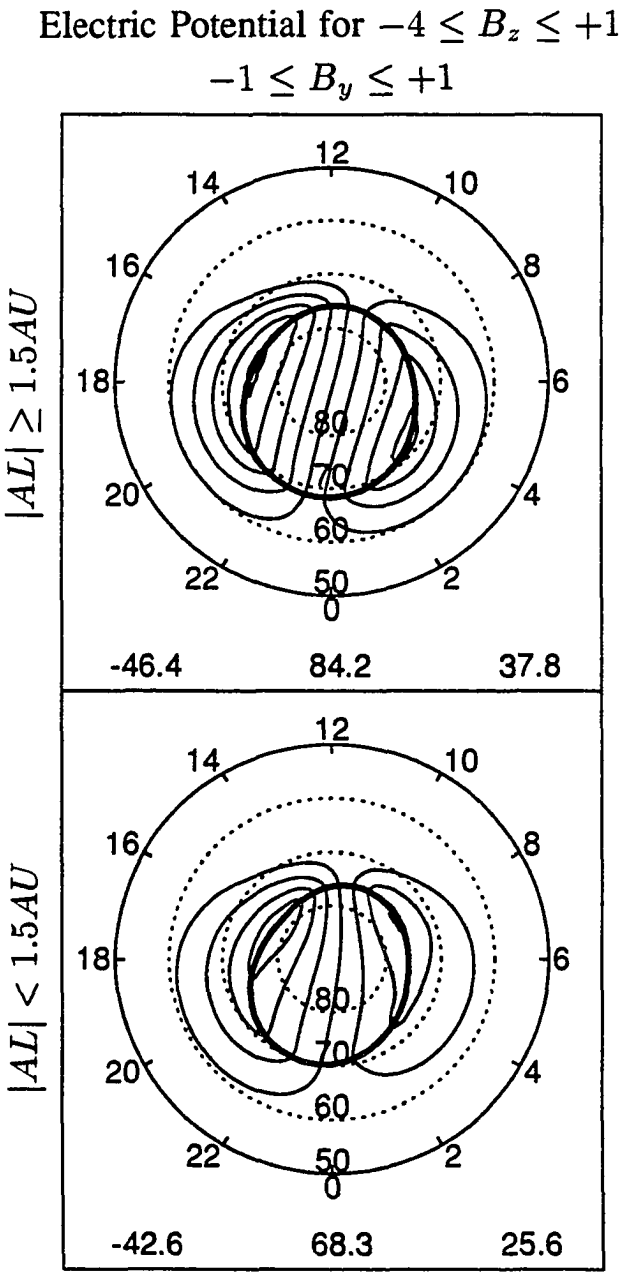

Figure 4.8 Illustration of the continuous convection reversal boundary for the subgroup with $-4 \leq B_z \leq +1$ and $-1 \leq B_y \leq +1$. The representation of lines and numbers is the same as that in Figure 4.1.

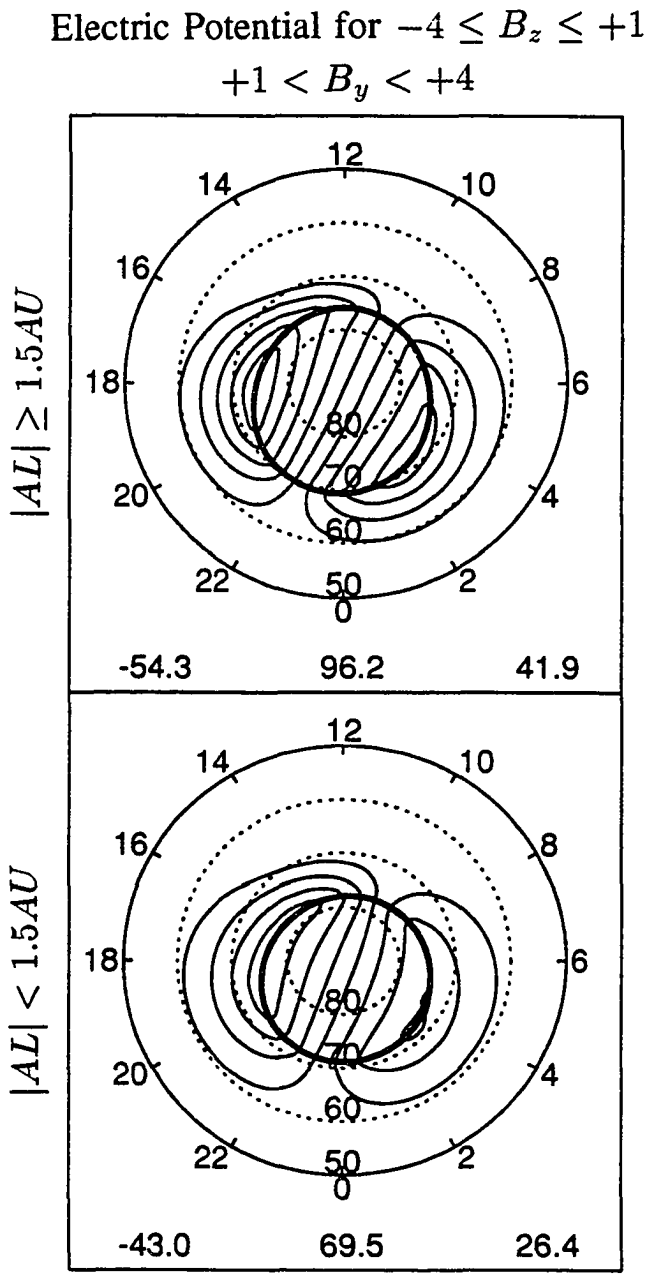

Figure 4.9 Illustration of the continuous convection reversal boundary for the subgroup with $-4 \leq B_z \leq +1$ and $+1 < B_y < +4$. The representation of lines and numbers is the same as that in Figure 4.1.

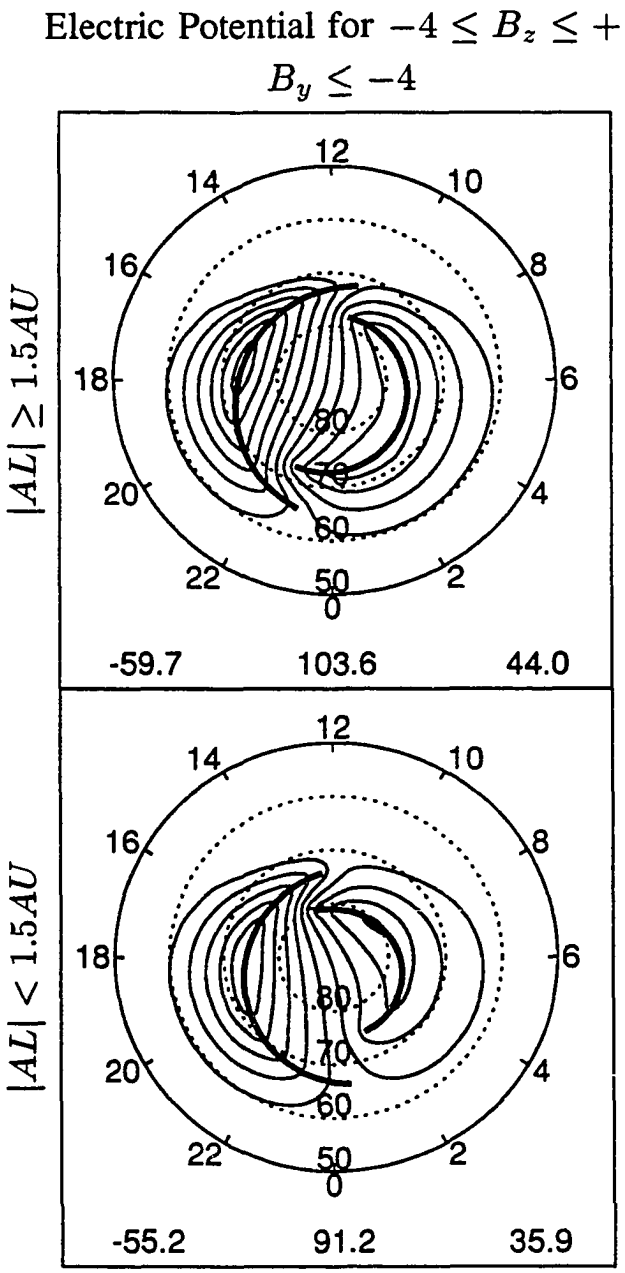

Figure 4.10 Illustration of the discontinuous convection reversal boundary for the subgroup with $-4 \leq B_z \leq +1$ and $B_y \leq -4$. These graphs were derived by solving the Laplace equation. The thin solid lines represent the equipotential lines and the heavy solid lines represent the convection reversal boundary. The numbers at lower-left and lower-right corners in each graph represent the dusk and dawn potentials, respectively.

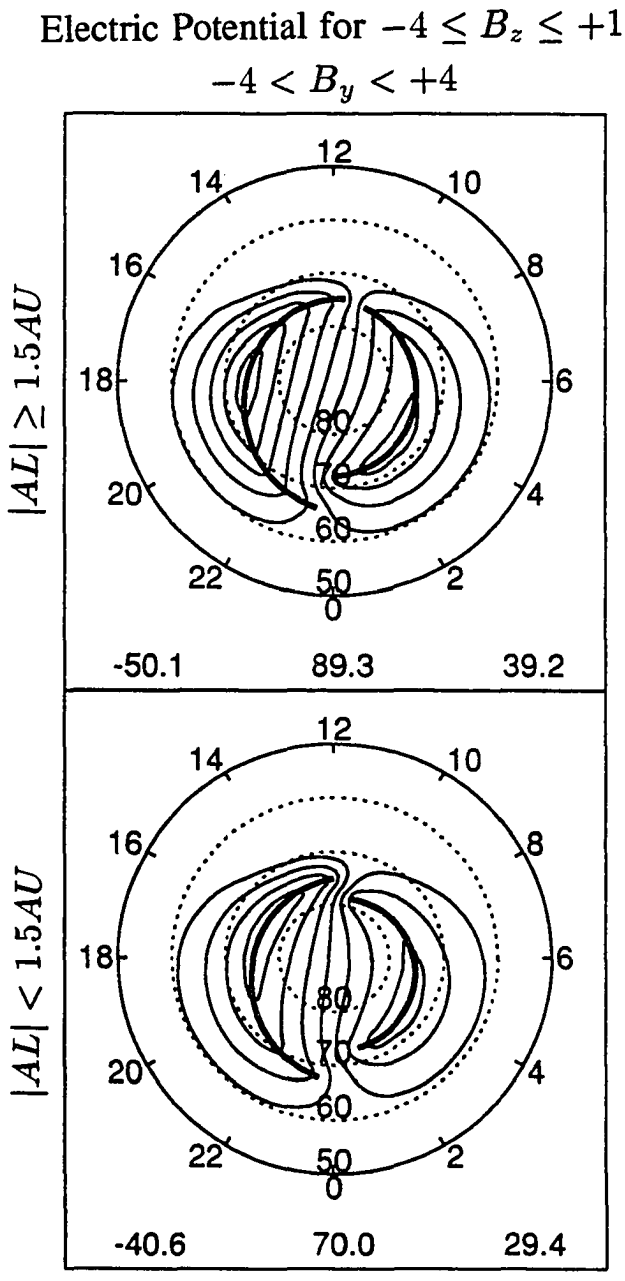

Figure 4.11 Illustration of the discontinuous convection reversal boundary for the subgroup with $-4 \leq B_z \leq +1$ and $-4 < B_y < +4$. The representation of lines and numbers is the same as that in Figure 4.10.

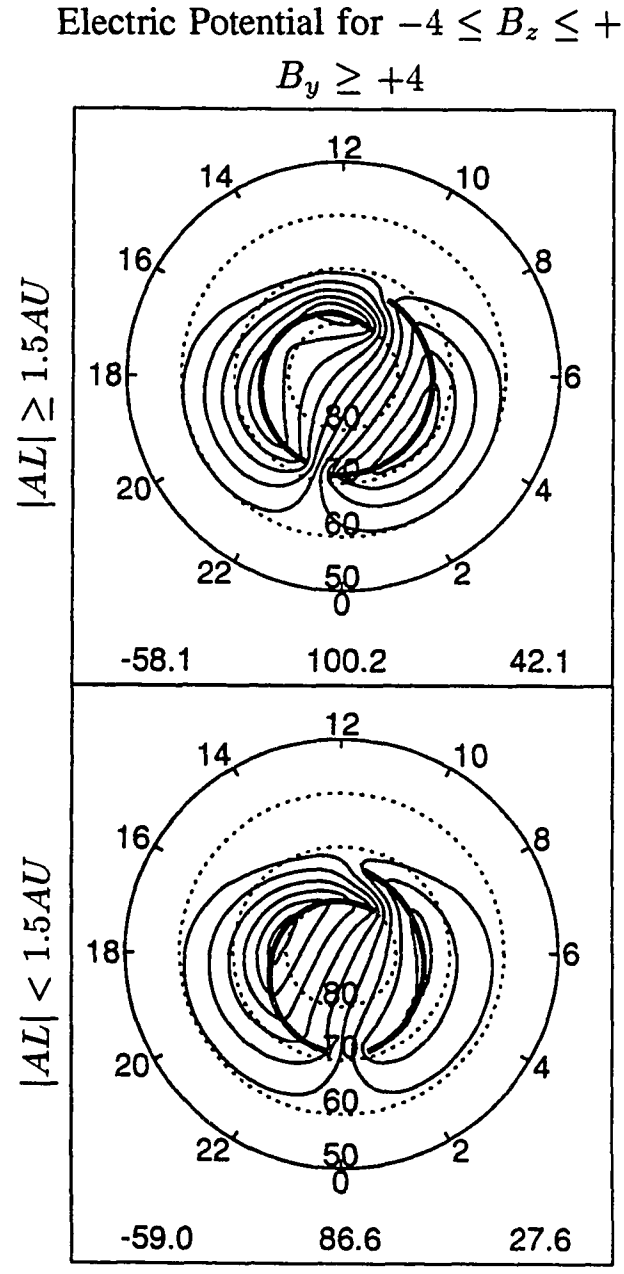

Figure 4.12 Illustration of the discontinuous convection reversal boundary for the subgroup with $-4 \leq B_z \leq +1$ and $B_y \geq +4$. The representation of lines and numbers is the same as that in Figure 4.10.

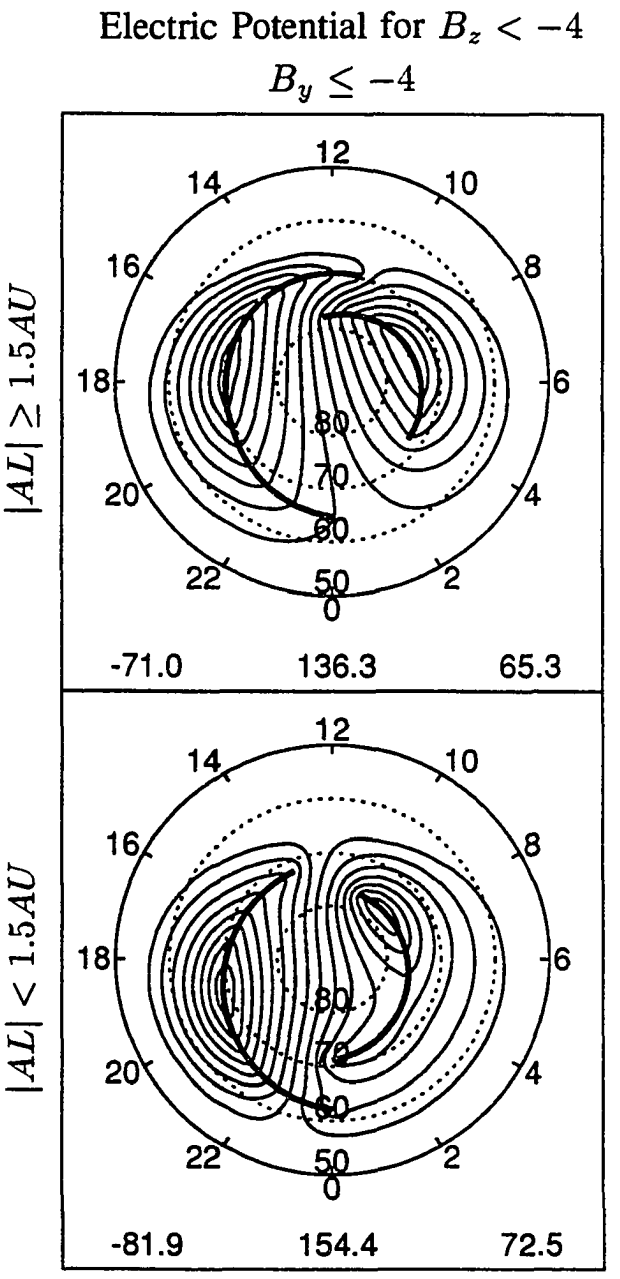

Figure 4.13 Illustration of the discontinuous convection reversal boundary for the subgroup with $B_z < -4$ and $B_y \leq -4$. The representation of lines and numbers is the same as that in Figure 4.10.

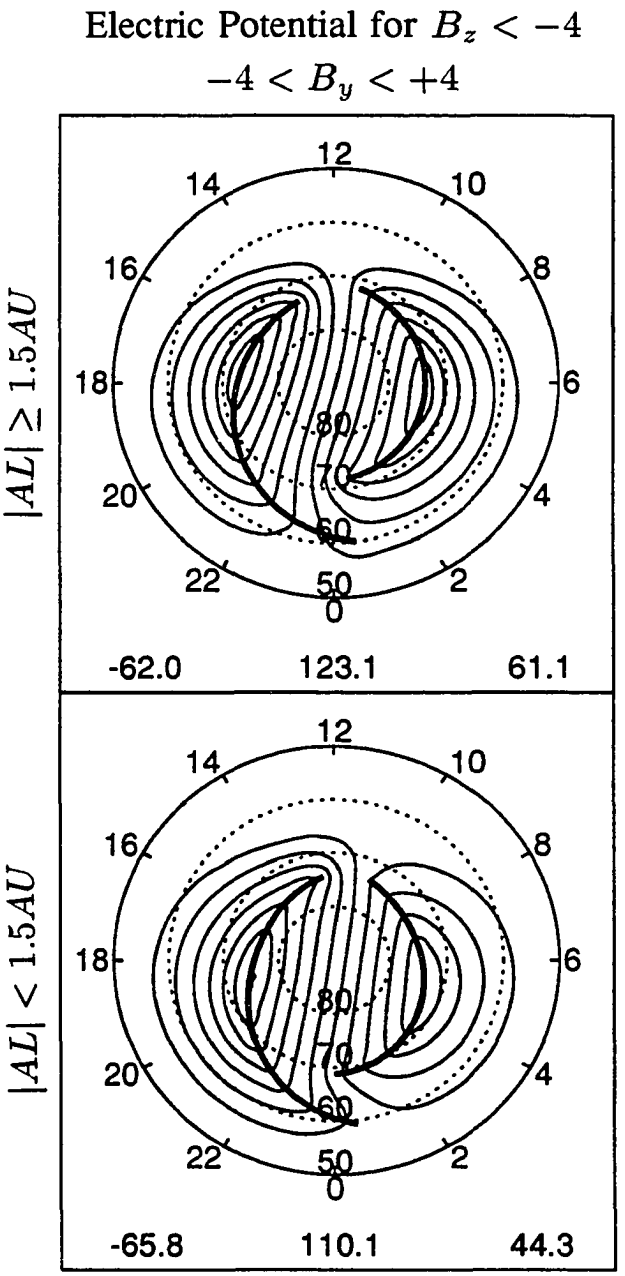

Figure 4.14 Illustration of the discontinuous convection reversal boundary for the subgroup with $B_z < -4$ and $-4 < B_y < +4$. The representation of lines and numbers is the same as that in Figure 4.10.

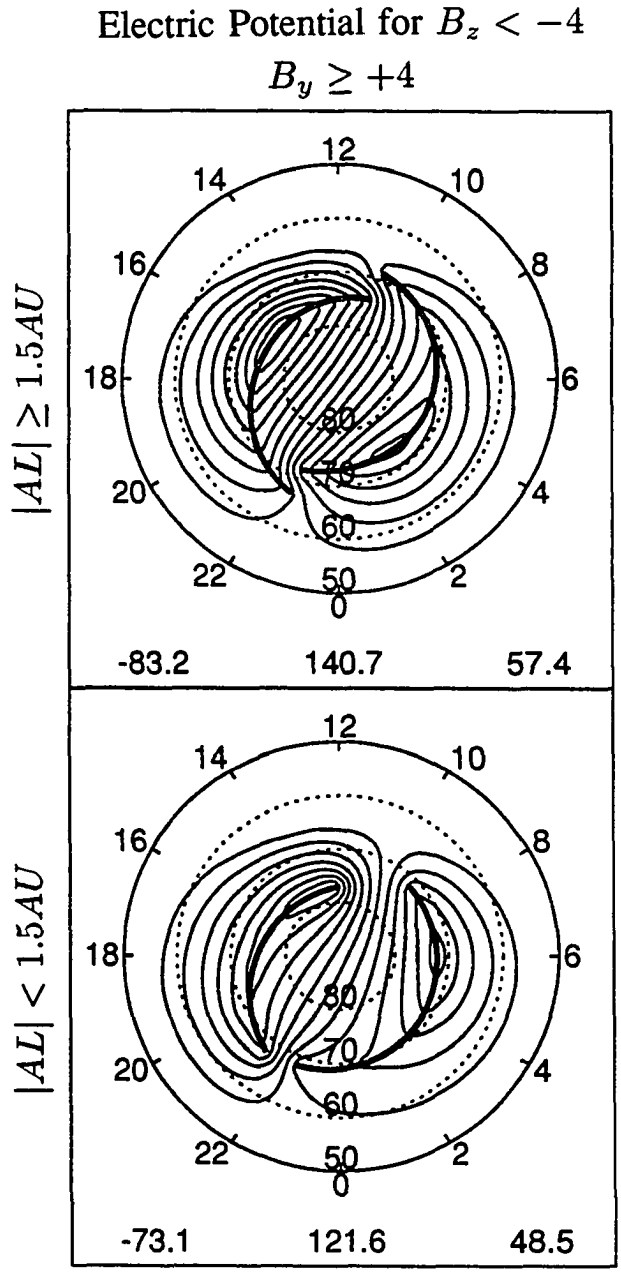

Figure 4.15 Illustration of the discontinuous convection reversal boundary for the subgroup with $B_z < -4$ and $B_y \geq +4$. The representation of lines and numbers is the same as that in Figure 4.10.

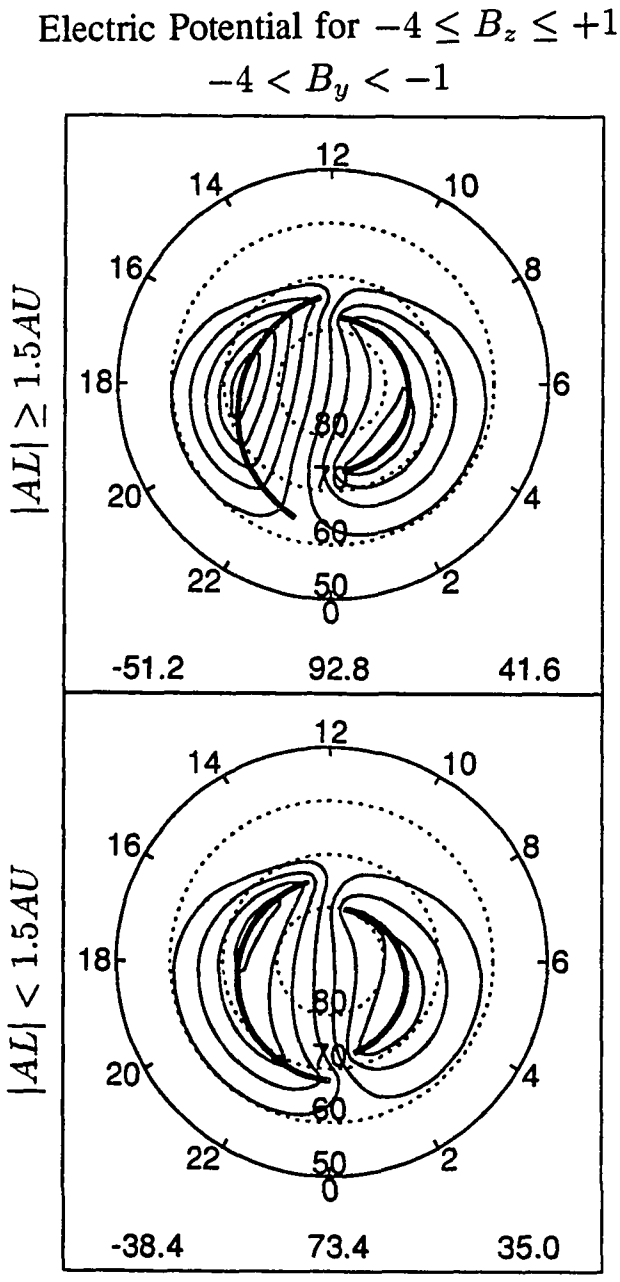

Figure 4.16 Illustration of the discontinuous convection reversal boundary for the subgroup with $-4 \leq B_z \leq +1$ and $-4 < B_y < -1$. The representation of lines and numbers is the same as that in Figure 4.10.

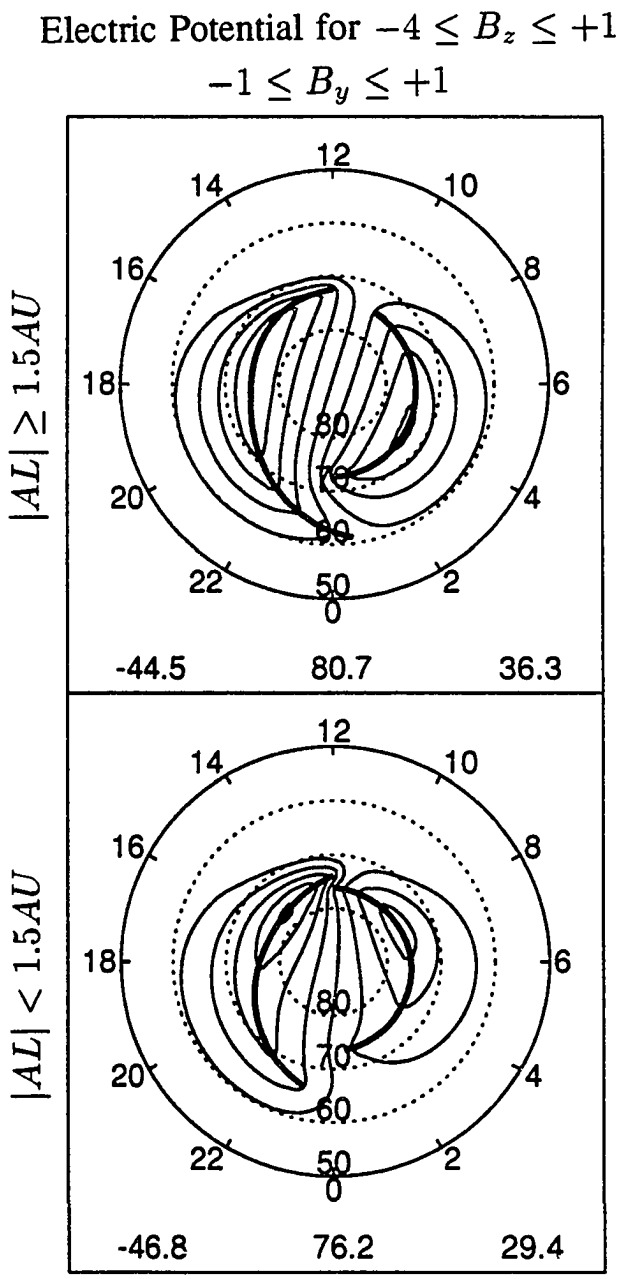

Figure 4.17 Illustration of the discontinuous convection reversal boundary for the subgroup with $-4 \leq B_z \leq +1$ and $-1 \leq B_y \leq +1$. The representation of lines and numbers is the same as that in Figure 4.10.

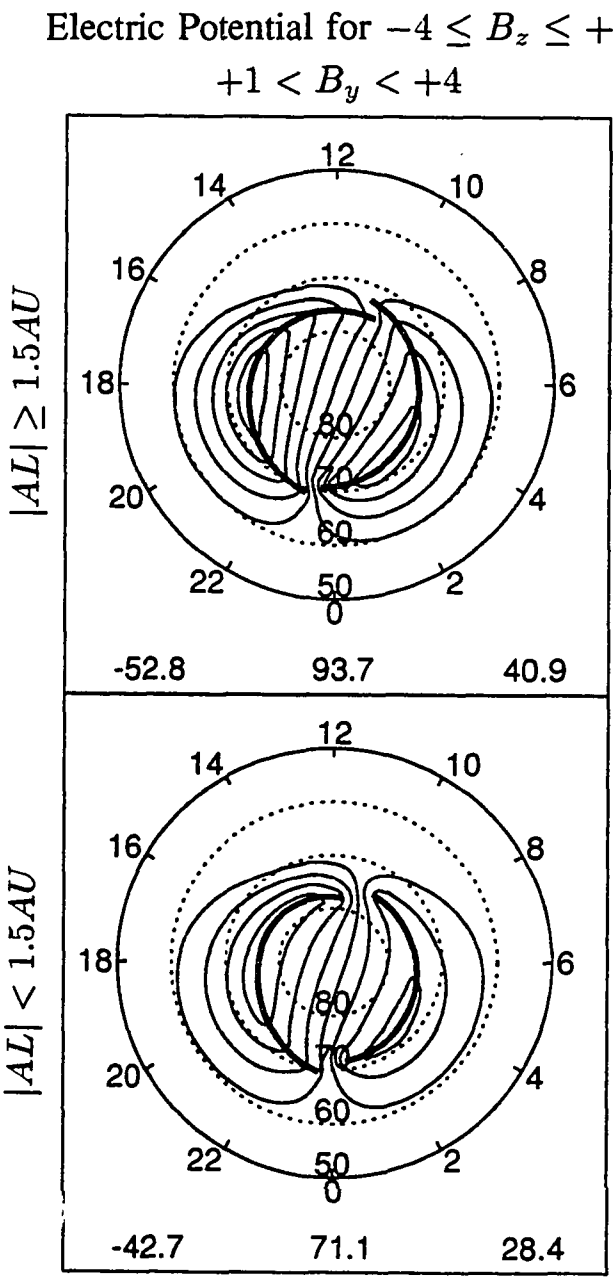

Figure 4.18 Illustration of the discontinuous convection reversal boundary for the subgroup with $-4 \leq B_z \leq +1$ and $+1 < B_y < +4$. The representation of lines and numbers is the same as that in Figure 4.10.

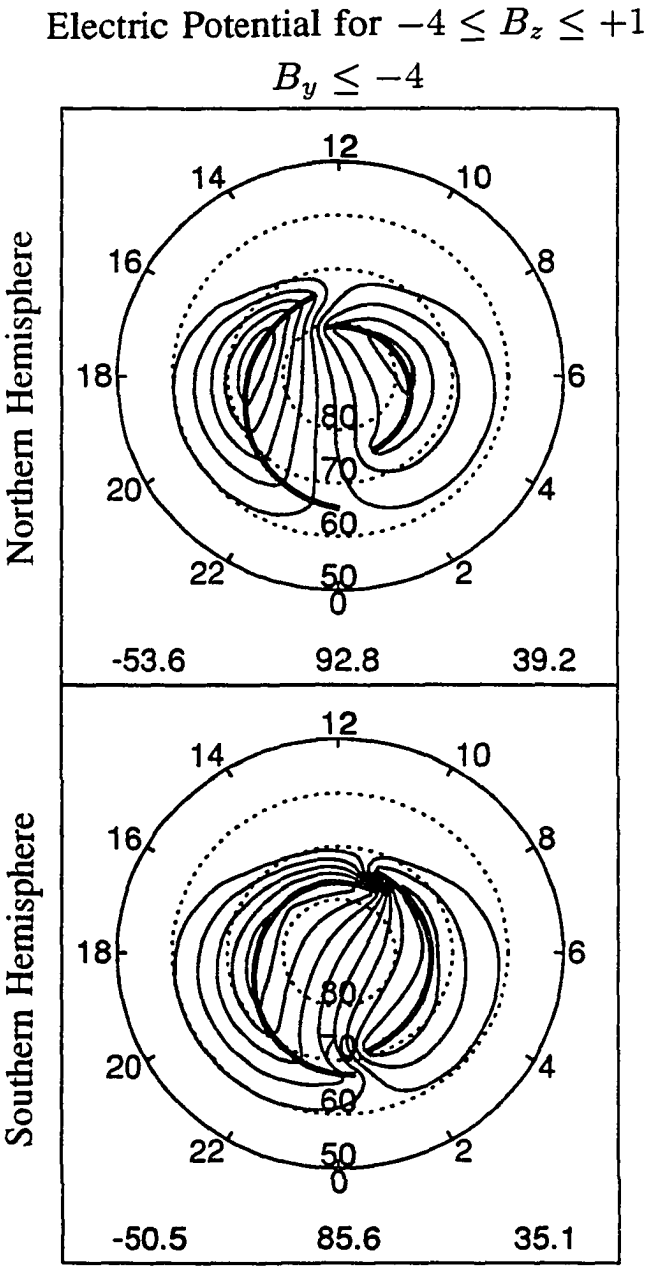

Figure 4.19 Illustration of the B_y effect on the patterns in different hemispheres for the subgroup with $-4 \leq B_z \leq +1$ and $B_y \leq -4$. The upper graph shows the patterns in the northern hemisphere and the lower graph shows the patterns in the southern hemisphere. The thin and heavy solid lines represent the equipotential lines and convection reversal boundary. The numbers at lower-left and lower-right corners represent the dusk and dawn potentials.

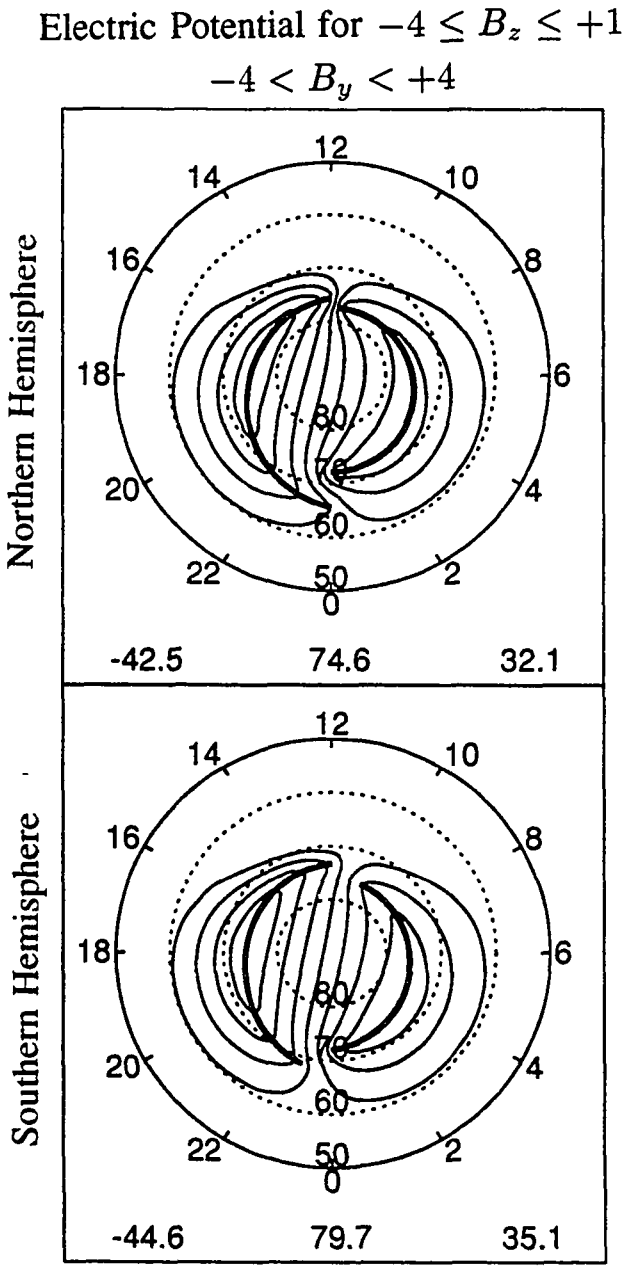

Figure 4.20 Illustration of the B_y effect on the patterns in different hemispheres for the subgroup with $-4 \leq B_z \leq +1$ and $-4 < B_y < +4$. The representation of lines and numbers is the same as that in Figure 4.19.

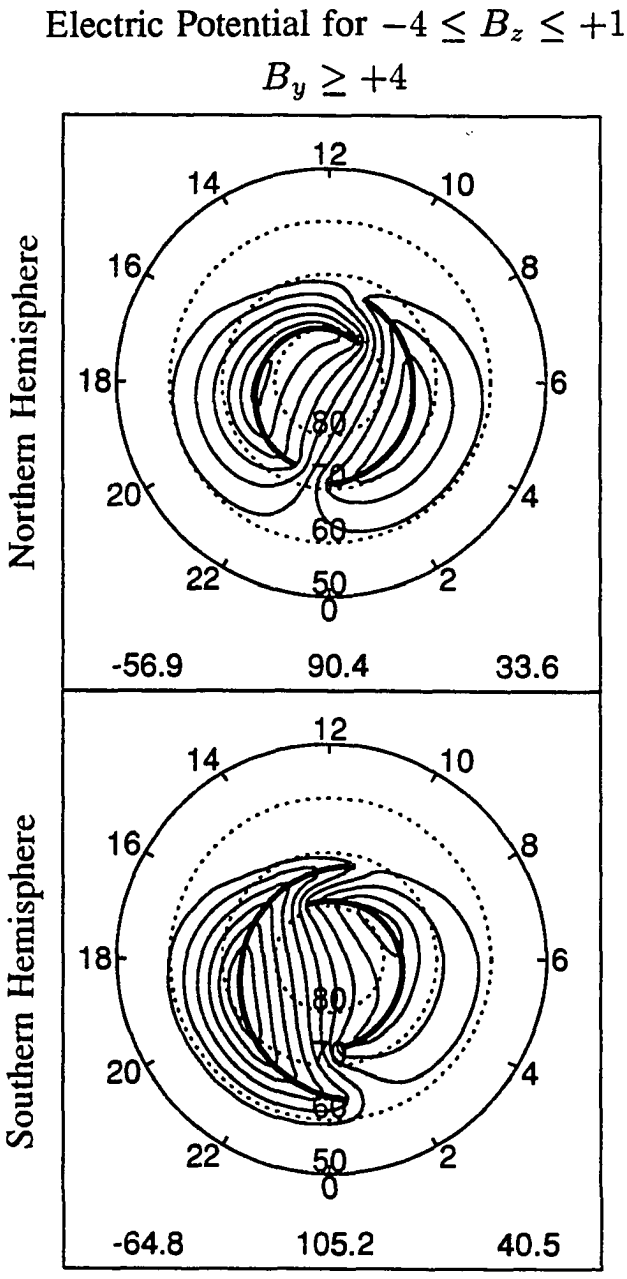

Figure 4.21 Illustration of the B_y effect on the patterns in different hemispheres for the subgroup with $-4 \leq B_z \leq +1$ and $B_y \geq +4$. The representation of lines and numbers is the same as that in Figure 4.19.

it is reasonable to mix the passes both in the northern and southern hemispheres according to IMF B_y.

4.3 A Model for Solving the Inhomogeneous Current Continuity Equation

Solving (4.9) is only for illustrating the fitting boundary conditions, but in a real situation the conductivity is nonuniform. For the lack of the corresponding conductivity model, a conductivity model which consists of day-night effect and enhancement of particles precipitation [*Rasmussen and Schunk*, 1987] has been used. The day-night conductivity model considers the direct solar EUV radiation [*Vickrey et al.*, 1981]

$$\Sigma_H = P\Sigma_P = 10\sqrt{\cos\chi} \tag{4.10}$$

and scattered solar EUV radiation [*Strobel et al.*, 1980]

$$\begin{aligned} \Sigma_H = P\Sigma_P &= 1 \qquad && \chi \leq 90^\circ \\ \Sigma_H = P\Sigma_P &= 10^{\cos\chi} && \chi > 90^\circ \end{aligned} \tag{4.11}$$

where χ is the solar zenith angle and P is the ratio of height-integrated Hall to Pedersen conductivity. The χ can be calculated from seasonal tilt angle and dipole tilt angle. The details of the calculation of χ are discussed in Appendix D.

The conductivity enhancement due to particles precipitation can be estimated from the electron average energy E_0 and the electron energy flux I [*Robinson et al.*, 1987]

$$\Sigma_P = [\frac{40E_0}{(16 + E_0^2)}]I^{0.5} \tag{4.12}$$

where E_0 is in units of keV and I is in units of ergs/cm^{2}s. The ratio of the Hall to Pedersen conductivity is given by

$$\frac{\Sigma_H}{\Sigma_P} = 0.45E_0^{0.85}. \tag{4.13}$$

Hardy et al. [1987] used (4.12) and (4.13) to calculate the height-integrated, electron-produced Hall and Pedersen conductivity. They divided the data under different K_p values.

From their model the conductivity patterns can be assumed to be a Gaussian distribution in latitude and longitude, thus

$$\Sigma_H = \Sigma_{H_0} exp[-\frac{(\theta - \theta_0)^2}{D_\theta^2} - \frac{(\phi - \phi_0)^2}{D_\phi^2}] \qquad (4.14)$$
$$\Sigma_H = P\Sigma_P$$

where Σ_{H_0}, P, ϕ_0, D_θ, and D_ϕ can be estimated from their patterns. The specification of these parameters is shown in Table 4.1. The location of peak conductivity at each local time, θ_0, has been adjusted to match the continuous boundary in each category. As pointed out by *Wallace and Budzinski* [1981], the conductivities from different sources cannot be simply added. It should be calculated by the square root of the sum of squares of components.

The illustrative convection patterns have implicit field-aligned currents on the convection reversal boundary. The region 1 current is confined to a width of one degree. This is not far from the real field-aligned current pattern. But, the region 2 current is located on the low-latitude boundary. This is not realistic. For lack of corresponding field-aligned current model, the region 2 current is assumed a Gaussian shape three degrees outside the region 1 current. The locations of peak on the dawnside and duskside remains fixed, but the peak value of the region 2 current has been adjusted until the field-aligned current difference between into and out of the ionosphere is less than 5%. This makes the total field-aligned current conserved.

The equation (4.8) can be solved by specifying a nonuniform conductivity distribution and a region 2 current distribution. The details of numerical scheme for solving (4.8) are shown in Appendix E.

Table 4.1 The specification of the parameters in the conductivity model.

Groups	$\Sigma_{H_0}(mho)$	P	$\phi_0(deg.)$	$D_\theta(deg.)$	$D_\phi(deg.)$
$-4 \leq B_z \leq +1$	15	2	-90	6	90
$B_z \leq -4$	25	2	-75	6	90

4.4 Resulting Ionospheric Convection Patterns

For lack of observational information on the corresponding conductivity and field-aligned current in the ionosphere, a conductivity model and a region 2 field-aligned current model have been used to show the sequences how the conductivity and field-aligned current affect the ionospheric convection. Figures 4.22 - 4.30 are the resulting convection patterns for only adding the conductivity on the model. The results show that another convection reversal is detached from the dusk-cell convection reversal near midnight.

A condition was imposed on the region 2 field-aligned current is that the total upward current (summed over both the region 1 and region 2 currents) is equal to the total downward current. This is important because the upward and downward region 1 field-aligned currents, which were determined from the DE-2 measurements (combined with the conductivity model), are not balanced by themselves. Figures 4.31 - 4.39 are the resulting convection patterns for adding both the conductivity and field-aligned current on the model. The results show that another convection reversal on the duskside shifts back to the determined convection reversal and the electric field is enhanced in the region between region 1 and region 2 currents.

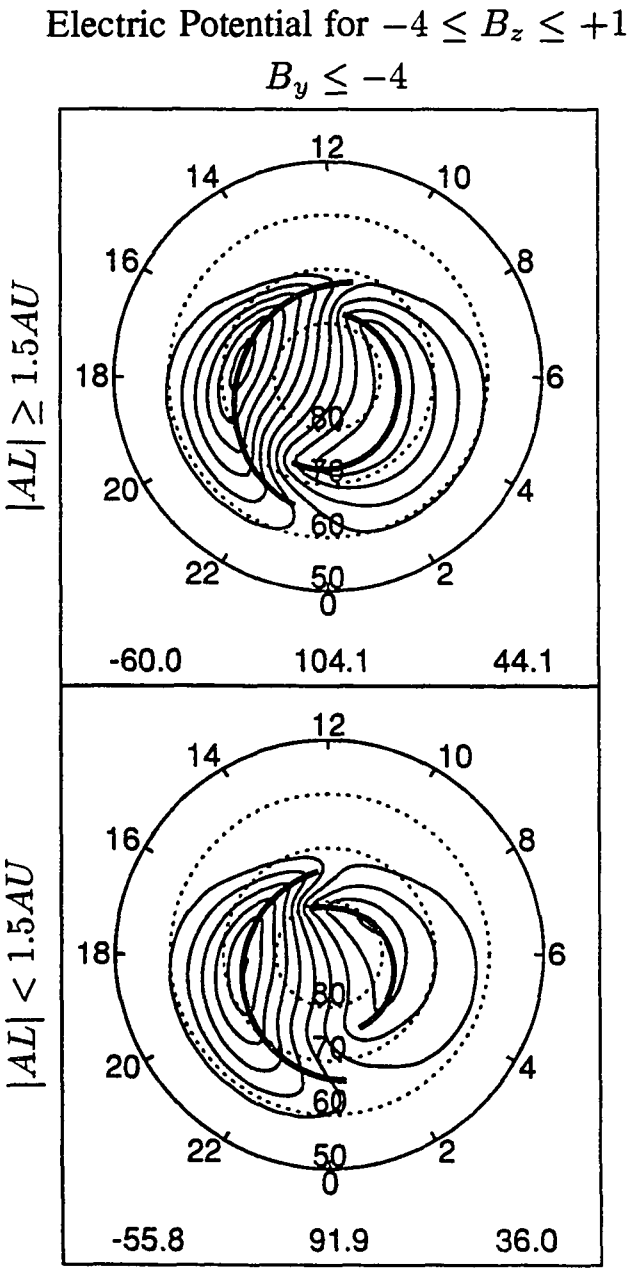

Figure 4.22 Reproduction of the ionospheric convection patterns for the subgroup with $-4 \leq B_z \leq +1$ and $B_y \leq -4$. These graphs were derived by solving the current continuity equation with nonuniform conductivity. The thin solid lines represent the equipotential lines and the heavy solid lines represent the convection reversal boundary. The numbers at lower-left and lower-right corners in each graph represent the dusk and dawn potentials, respectively.

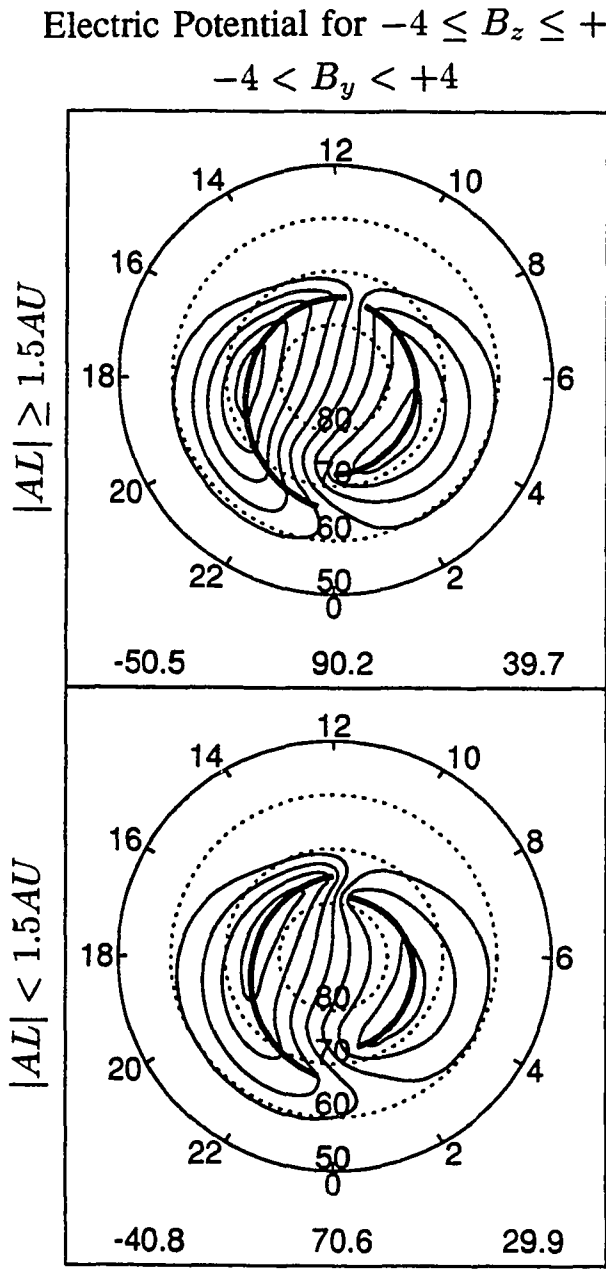

Figure 4.23 Reproduction of the ionospheric convection patterns for the subgroup with $-4 \leq B_z \leq +1$ and $-4 < B_y < +4$. The representation of lines and numbers is the same as that in Figure 4.22.

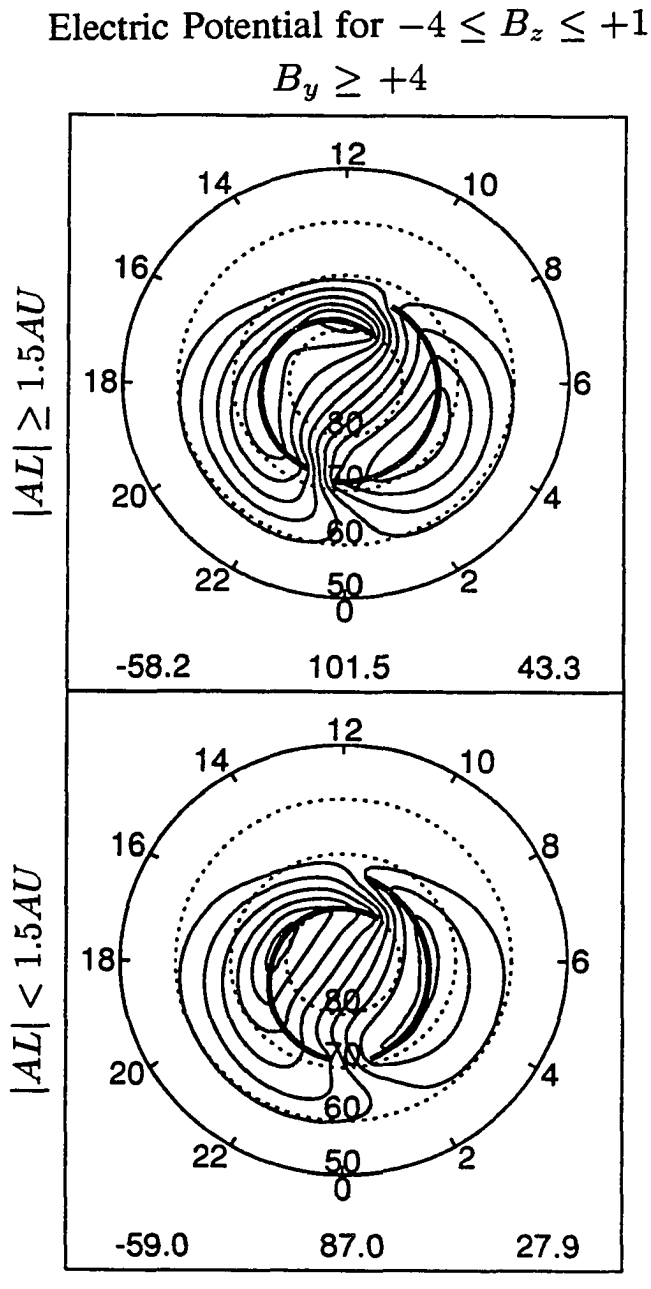

Figure 4.24 Reproduction of the ionospheric convection patterns for the subgroup with $-4 \leq B_z \leq +1$ and $B_y \geq +4$. The representation of lines and numbers is the same as that in Figure 4.22.

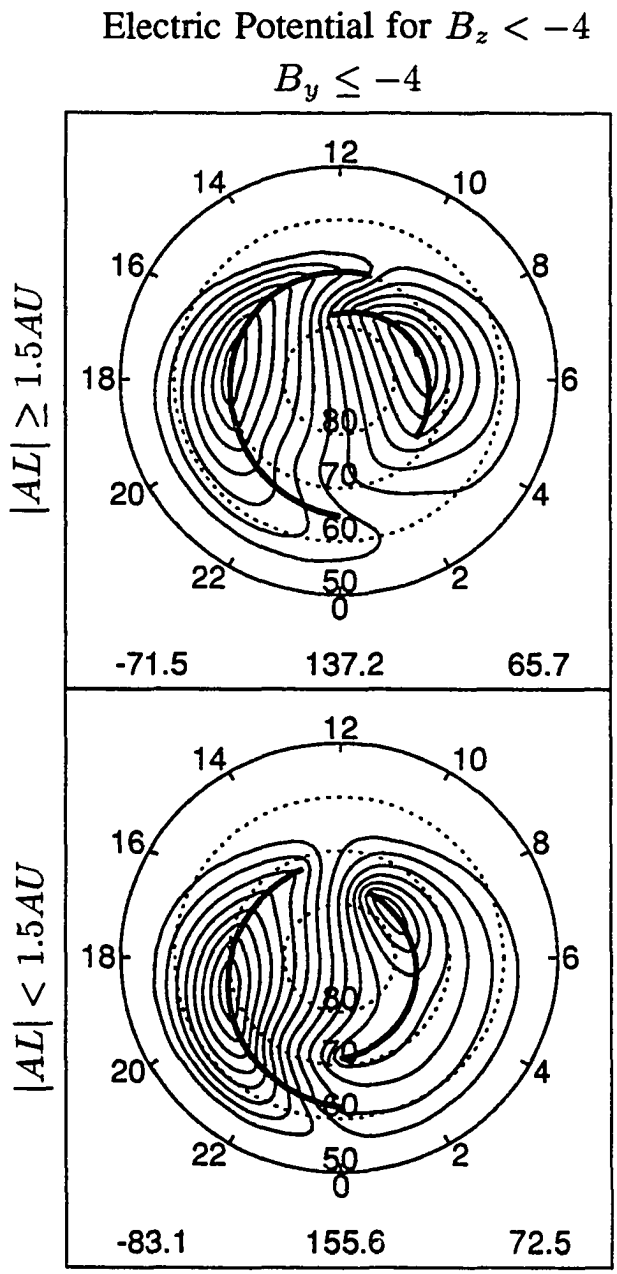

Figure 4.25 Reproduction of the ionospheric convection patterns for the subgroup with $B_z < -4$ and $B_y \leq -4$. The representation of lines and numbers is the same as that in Figure 4.22.

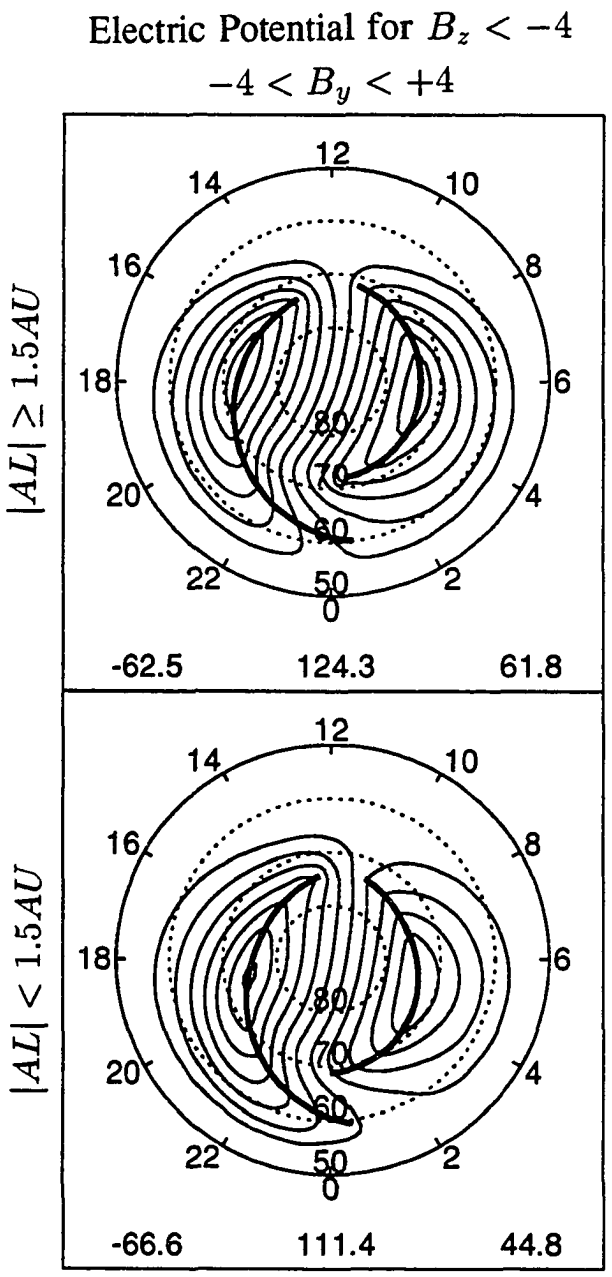

Figure 4.26 Reproduction of the ionospheric convection patterns for the subgroup with $B_z < -4$ and $-4 < B_y < +4$. The representation of lines and numbers is the same as that in Figure 4.22.

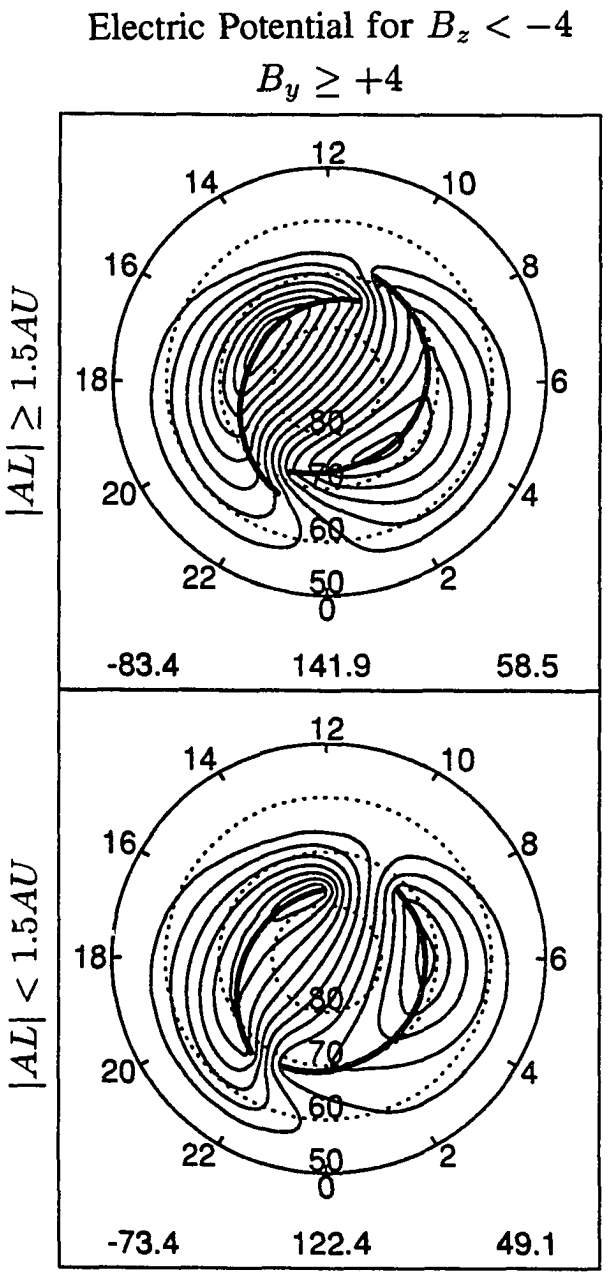

Figure 4.27 Reproduction of the ionospheric convection patterns for the subgroup with $B_z < -4$ and $B_y \geq +4$. The representation of lines and numbers is the same as that in Figure 4.22.

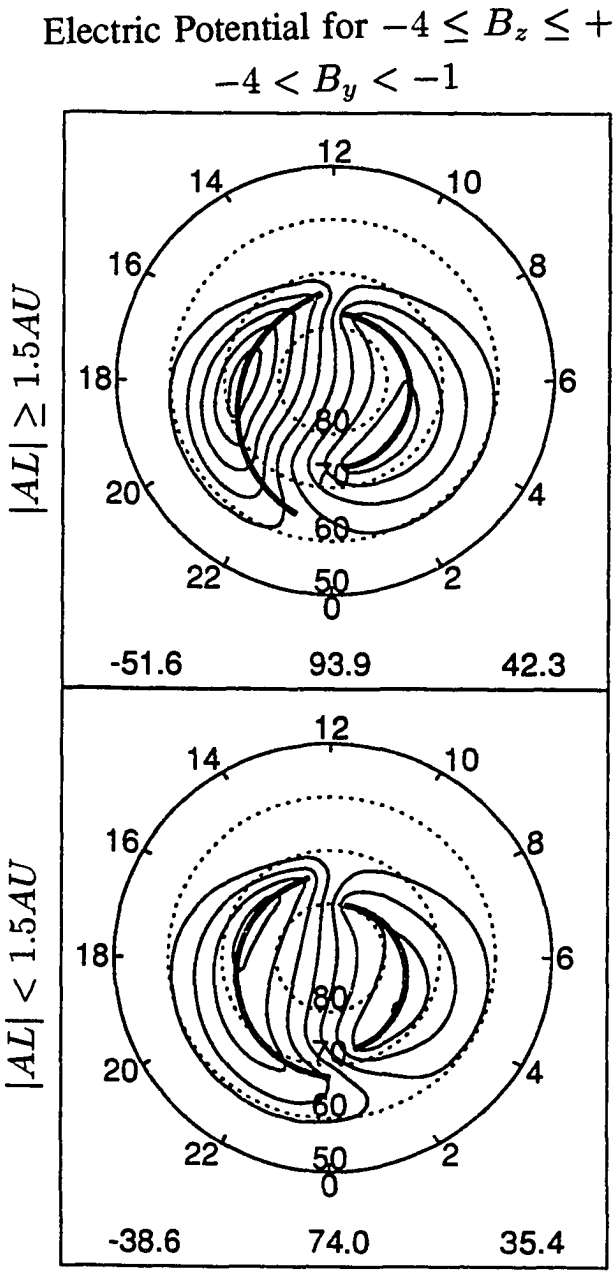

Figure 4.28 Reproduction of the ionospheric convection patterns for the subgroup with $-4 \leq B_z \leq +1$ and $-4 < B_y < -1$. The representation of lines and numbers is the same as that in Figure 4.22.

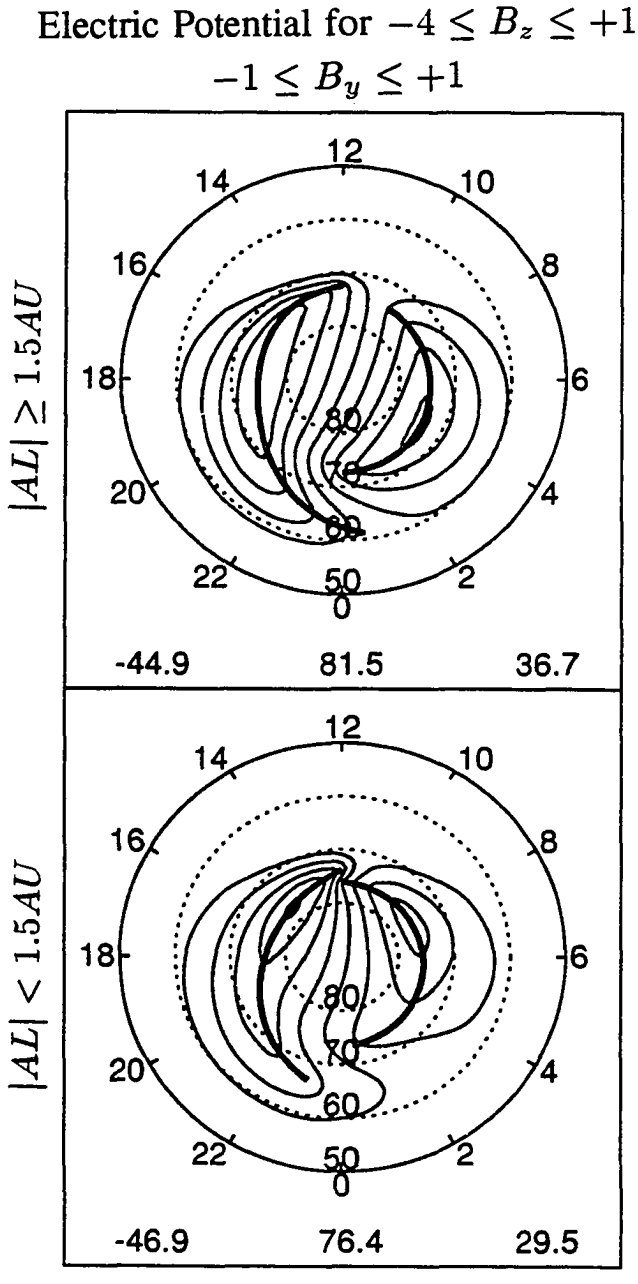

Figure 4.29 Reproduction of the ionospheric convection patterns for the subgroup with $-4 \leq B_z \leq +1$ and $-1 \leq B_y \leq +1$. The representation of lines and numbers is the same as that in Figure 4.22.

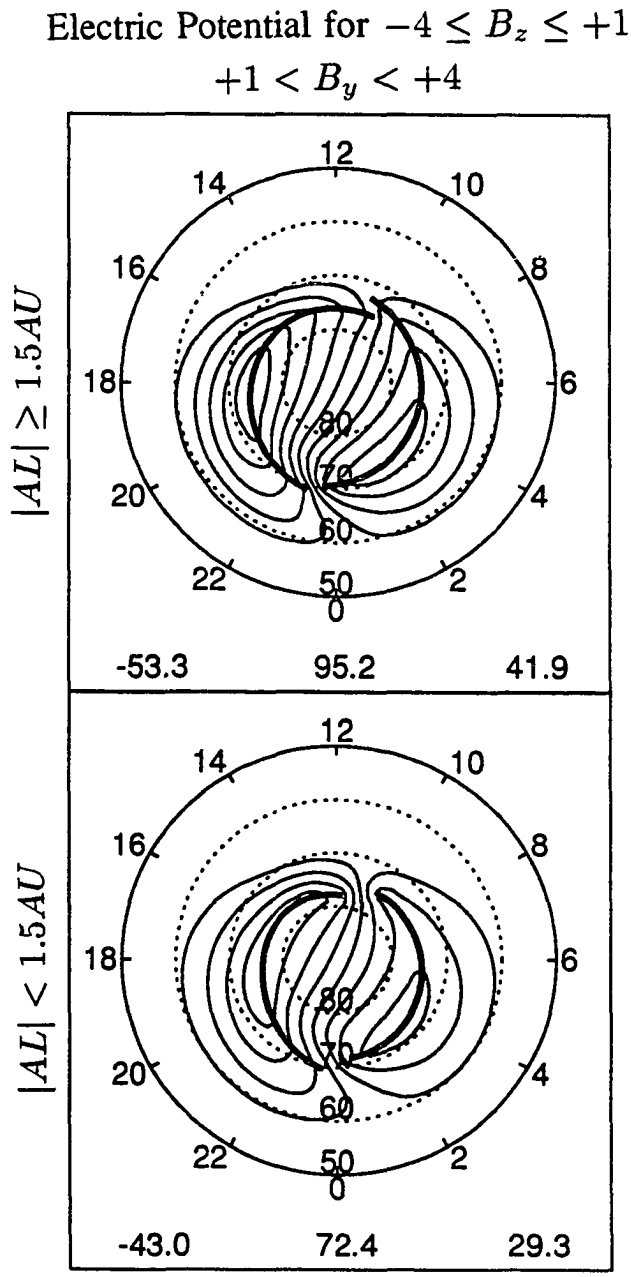

Figure 4.30 Reproduction of the ionospheric convection patterns for the subgroup with $-4 \leq B_z \leq +1$ and $+1 < B_y < +4$. The representation of lines and numbers is the same as that in Figure 4.22.

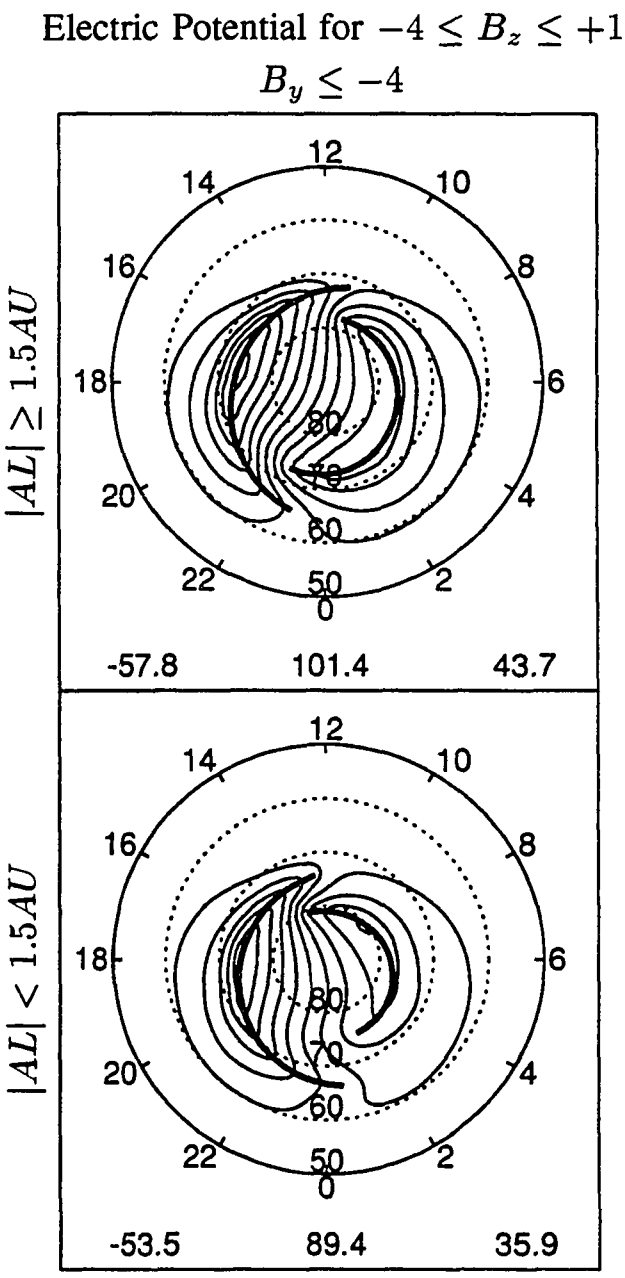

Figure 4.31 Reproduction of the ionospheric convection patterns for the subgroup with $-4 \leq B_z \leq +1$ and $B_y \leq -4$. These graphs were derived by solving the current continuity equation with nonuniform conductivity and region 2 current. The thin solid lines represent the equipotential lines and the heavy solid lines represent the convection reversal boundary. The numbers at lower-left and lower-right corners in each graph represent the dusk and dawn potentials, respectively.

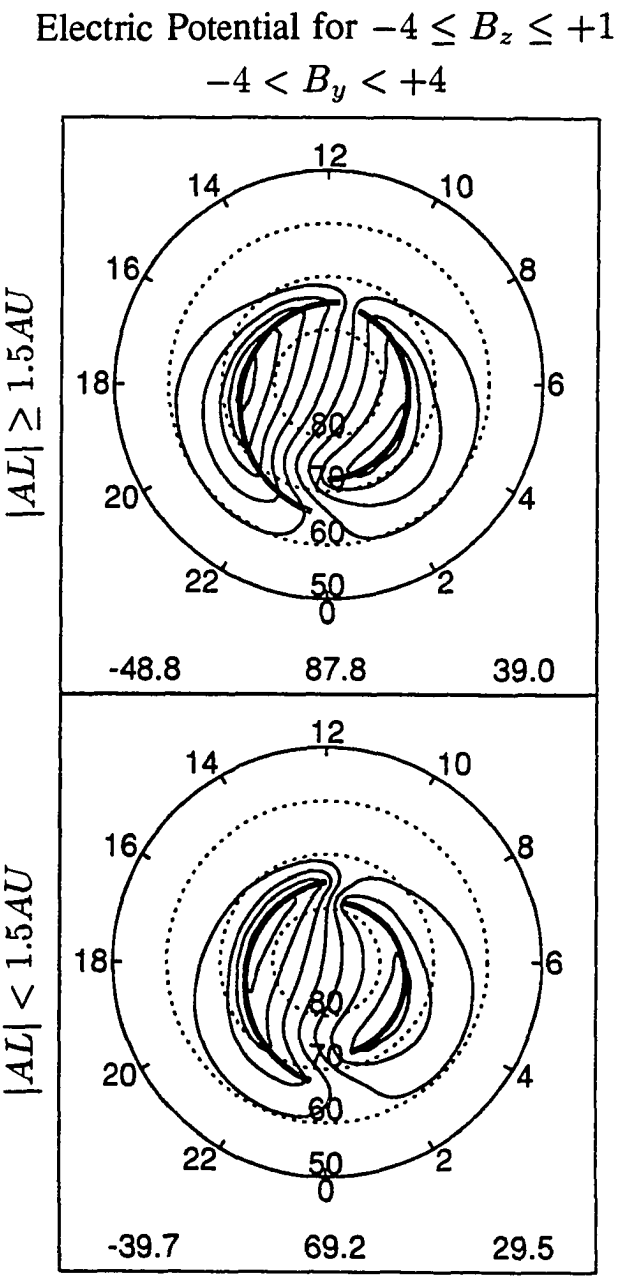

Figure 4.32 Reproduction of the ionospheric convection patterns for the subgroup with $-4 \leq B_z \leq +1$ and $-4 < B_y < +4$. The representation of lines and numbers is the same as that in Figure 4.31.

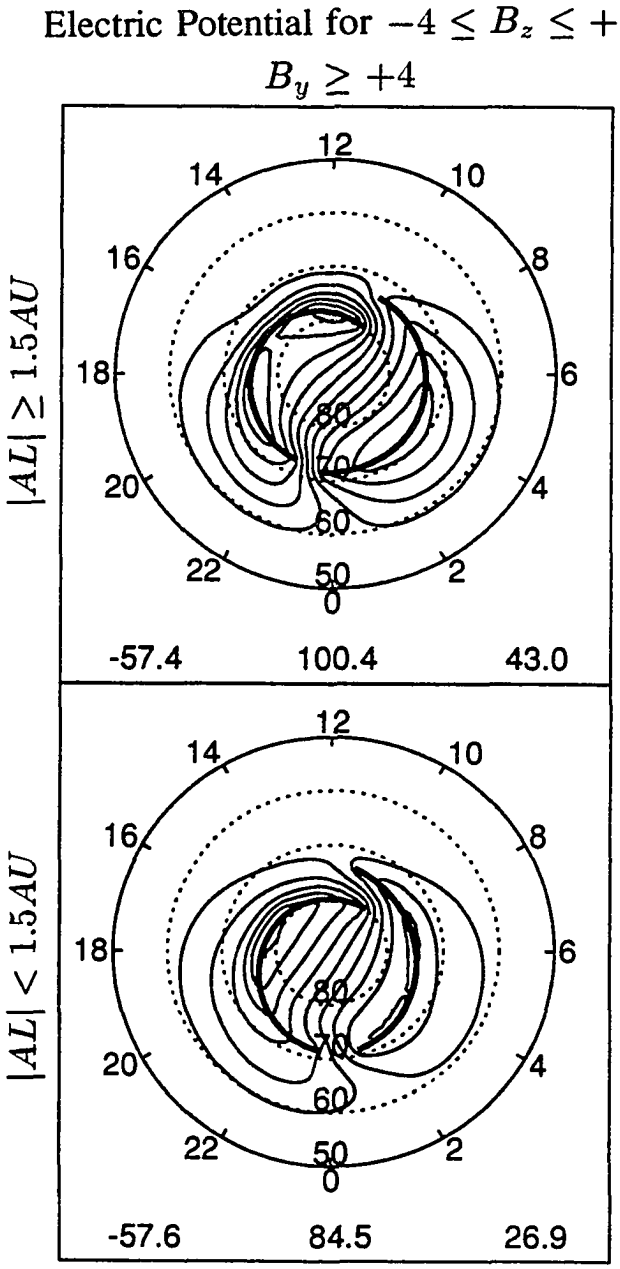

Figure 4.33 Reproduction of the ionospheric convection patterns for the subgroup with $-4 \leq B_z \leq +1$ and $B_y \geq +4$. The representation of lines and numbers is the same as that in Figure 4.31.

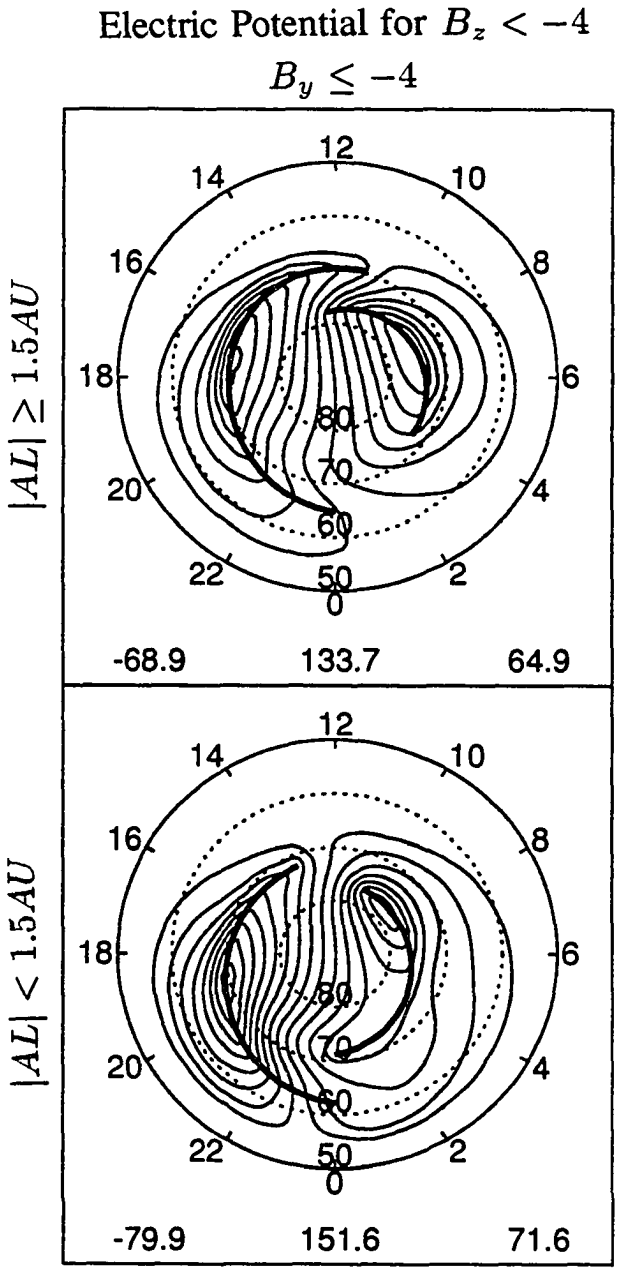

Figure 4.34 Reproduction of the ionospheric convection patterns for the subgroup with $B_z < -4$ and $B_y \leq -4$. The representation of lines and numbers is the same as that in Figure 4.31.

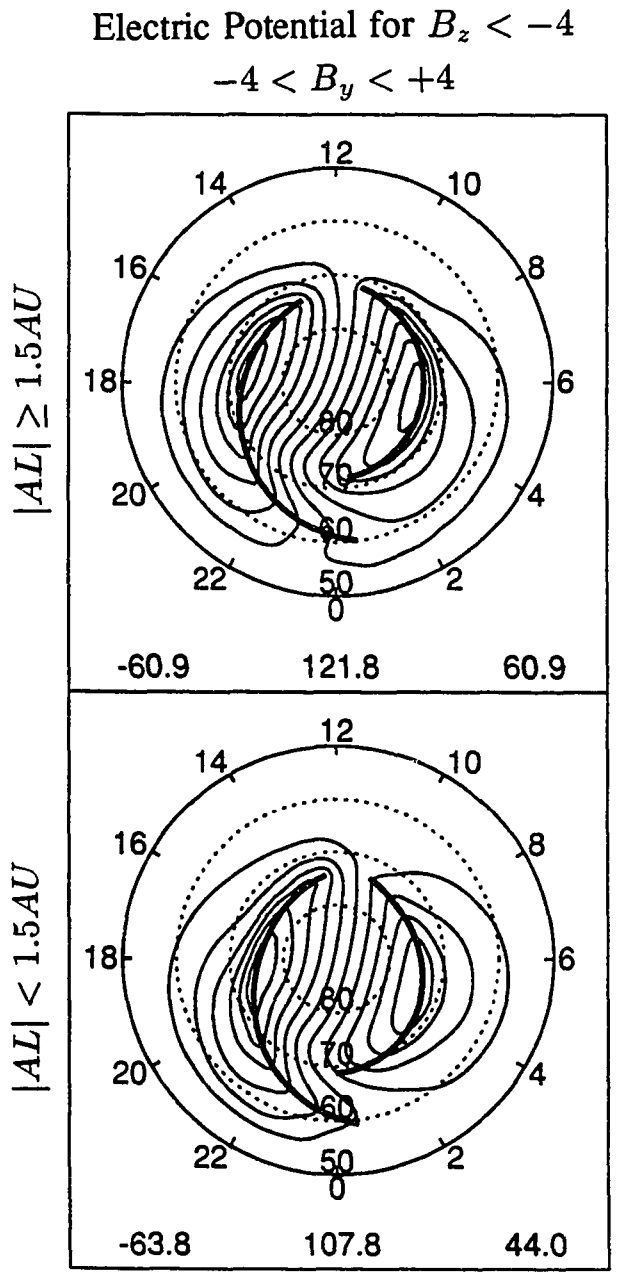

Figure 4.35 Reproduction of the ionospheric convection patterns for the subgroup with $B_z < -4$ and $-4 < B_y < +4$. The representation of lines and numbers is the same as that in Figure 4.31.

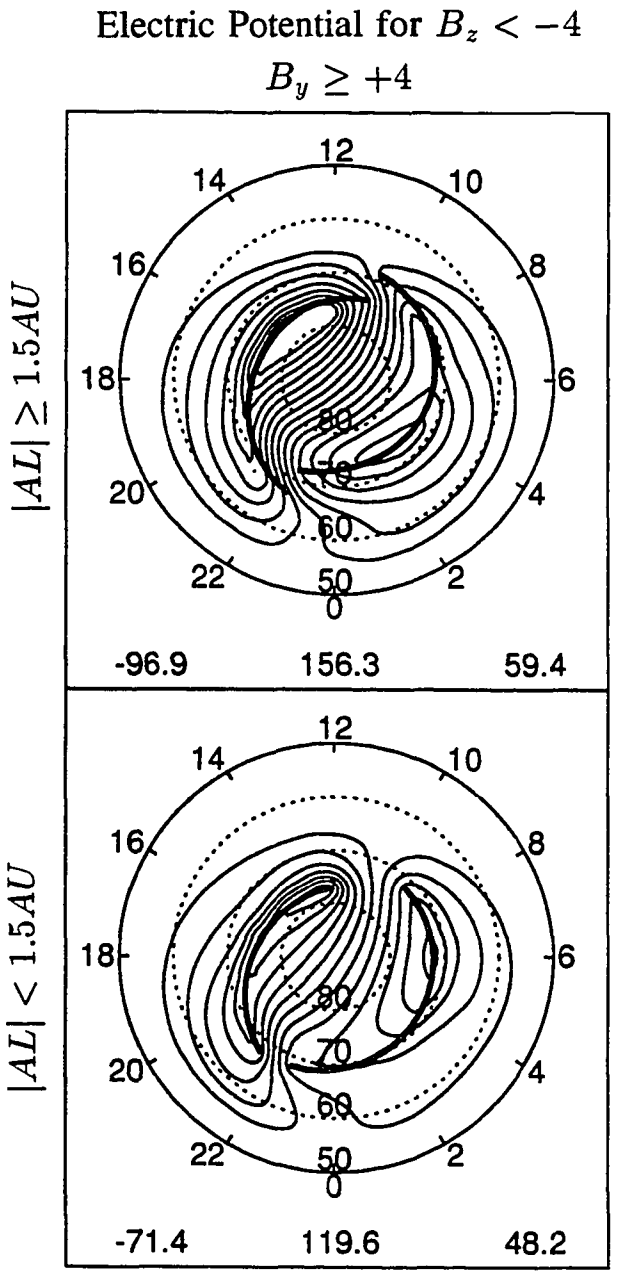

Figure 4.36 Reproduction of the ionospheric convection patterns for the subgroup with $B_z < -4$ and $B_y \geq +4$. The representation of lines and numbers is the same as that in Figure 4.31.

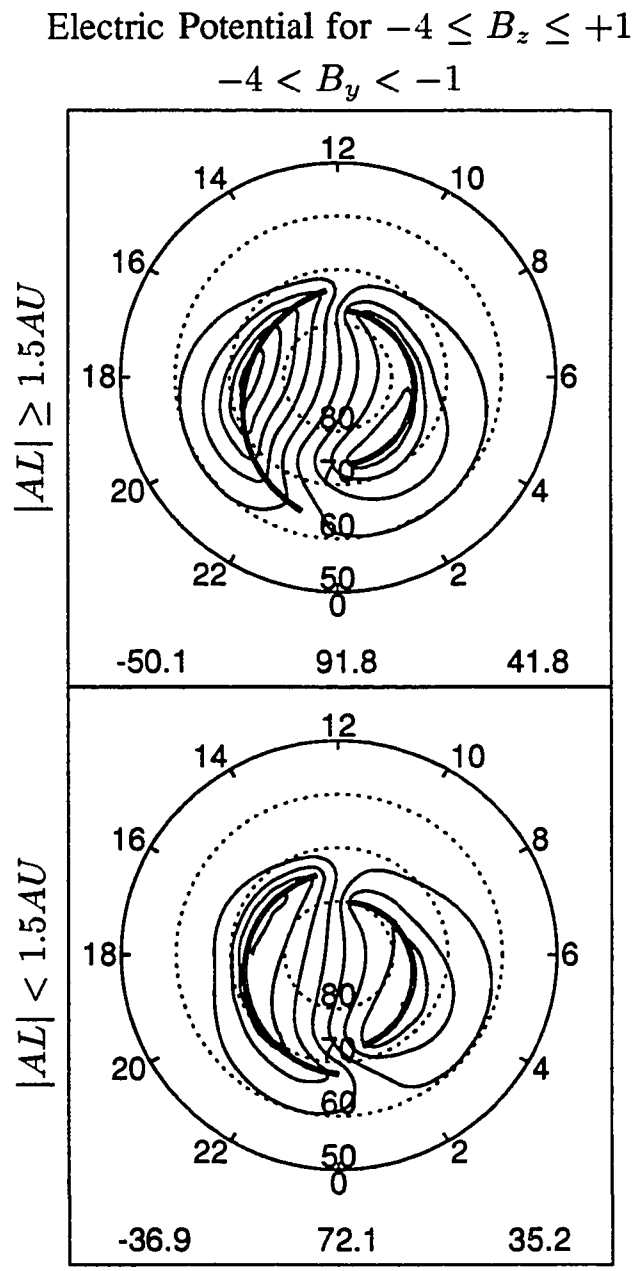

Figure 4.37 Reproduction of the ionospheric convection patterns for the subgroup with $-4 \leq B_z \leq +1$ and $-4 < B_y < -1$. The representation of lines and numbers is the same as that in Figure 4.31.

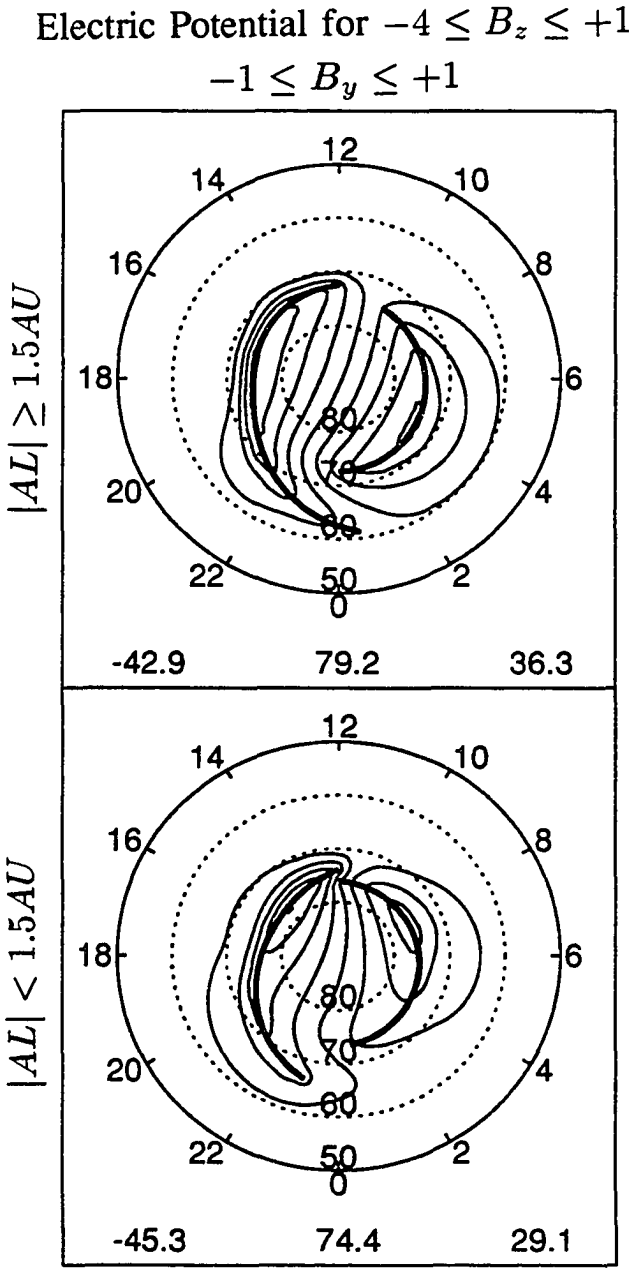

Figure 4.38 Reproduction of the ionospheric convection patterns for the subgroup with $-4 \leq B_z \leq +1$ and $-1 \leq B_y \leq +1$. The representation of lines and numbers is the same as that in Figure 4.31.

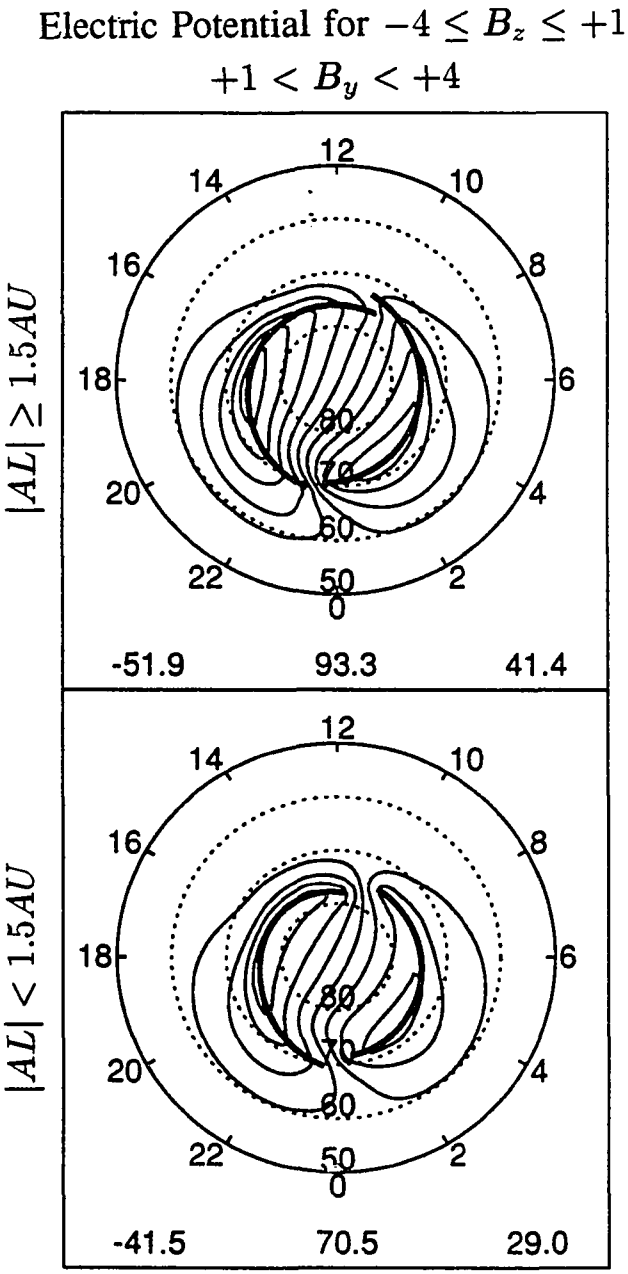

Figure 4.39 Reproduction of the ionospheric convection patterns for the subgroup with $-4 \leq B_z \leq +1$ and $+1 < B_y < +4$. The representation of lines and numbers is the same as that in Figure 4.31.

CHAPTER 5

Discussion

The DE-2 satellite has provided a large number of random measurements. These data show the combined influence of the IMF, auroral electrojet, and conductivity on the ionospheric electric fields. Each measurement shows the change of ionospheric electric field at different times and at different locations. These random measurements have been combined using the prevailing IMF and auroral electrojet conditions, in order to study the effects of southward IMF on the relationships among the auroral electrojet, the ionospheric conductivity, and ionospheric convection. In this way the assumption that the ionospheric convection is in steady state has been implicitly used. Unlike the method of averaging the potentials at every locations, the procedure that has been used in this study is similar to that of *Lu et al.* [1989]. They determined the potential values around the convection reversal boundary first, then used a simple model to calculate the potential values away from the boundary. But, three improvements have been done on their procedure. First of all, they normalize the potentials by a predicted value rather than a measured parameter. As discussed in Subsection 1.1.1, several coupling functions between the solar wind and transpolar cap potential have been found by the observational data, but nobody can tell which one is better. Therefore it may increase the uncertainty using the predicted values. In this study a parameter, AU, measured simultaneously with the electric field measurement is chosen. The measured potentials were normalized by the AU index instead of the predicted potential.

The second difference is related with the location of the boundary. The model of *Lu et al.* [1989] assumed the convection reversal boundary is circular, which is fixed at 75° latitude. From the data, the location of the convection reversal boundary varies with the local time.

Therefore, the convection reversal boundary cannot be assumed to be circular. In this study a function of boundary location in terms of MLT is obtained to reflect the variation of the location of the convection reversal.

The third difference is to see whether or not the convection reversal boundary is continuous. The model of *Lu et al.* [1989] has only one convection reversal at each local time. From the data the multiple convection reversal can be seen frequently in the electric field measurements, especially occurring near noon or midnight. This implies that the convection reversal boundary is not continuous, i.e., a potential gap is allowed near noon or midnight. Very few models [*Moses et al.*, 1987; *Heppner and Maynard*, 1987] have considered the potential gap. The usage of a continuous boundary can simplify the calculation, but it is not realistic. In this study the maximum and minimum potential points are fit with two separate functions to show the discontinuous boundary. It can be found that these two functions are usually overlapped near noon or midnight.

The difference between the continuous and discontinuous reversal boundaries is the gaps of potentials and locations. The discontinuous reversal boundary allows the gaps of potentials and locations around the convection reversal boundary at any local time. The continuous reversal boundary has a similarity to the classic drawing of auroral oval which is along the boundary of open and closed field lines. All the patterns with a continuous and a discontinuous reversal boundaries, as illustrated in Figures 4.1 - 4.18, show that the IMF B_y mainly affects the geometry of the convection reversal boundary which appear as the heavy lines in these figures. The convection pattern rotates clockwise as IMF B_y changes from negative to positive. The IMF B_y effect is not significant on the potential value around the convection reversal boundary. The size of the auroral oval and magnitude of potentials increase as the southward B_z increases in magnitude. These results are consistent with the model of *Heppner and Maynard* [1987], but these are based on different analysis of DE-2 data. Furthermore, the convection patterns with

a discontinuous reversal boundary are better than the convection patterns with a continuous reversal boundary because some features of eastward or westward flow near the cusp region are averaged out on the pattern with a continuous reversal boundary.

Figures 5.1 - 5.3 shows an overlay of the potential distribution around the continuous reversal boundary. The solid lines show the potential values as a function of MLT for the cases with an intense auroral electrojet ($|AL| \geq 1.5 \cdot AU$) and the dashed lines show the potential values for the cases with a weak auroral electrojet ($|AL| < 1.5 \cdot AU$). As the westward electrojet is intense, there is a common feature in these figures. The maximum potential increases and its location shifts towards midnight. The zero-potential point near midnight shifts towards premidnight and the slope (westward electric field) at this point increases except the category ($B_z < -4$ and $B_y \leq -4$). This inconsistency is attributed to the very few data between 0 and 4 MLT, so this apparent inconsistency is just the result of no data. The enhanced westward electric field near midnight is expected for an increased rate of magnetic flux of nightside reconnection.

The convection patterns with a discontinuous convection reversal boundary can result from the nonuniform ionospheric Hall conductivity. This has been demonstrated in the M-I coupling model [*Kan et al.*, 1988]. The ionospheric convection imposed by the solar wind in the M-I coupling model has been assumed to be a symmetric two-cell pattern with a continuous convection reversal boundary. However, due to the electrodynamic interaction between the magnetosphere and ionosphere, the resulting convection pattern becomes distorted to produce the Harang discontinuity, and convection reversal boundary becomes discontinuous, as shown in Figure 5 of [*Kan et al.*, 1988]. The distortion of the convection pattern and the discontinuous convection reversal boundary is caused by the nonuniform Hall conductivity.

To verify this, an example is shown in Figure 5.4. The upper-left side in Figure 5.4 is a Hall conductivity model which has only solar UV enhancement in summer solstice. The

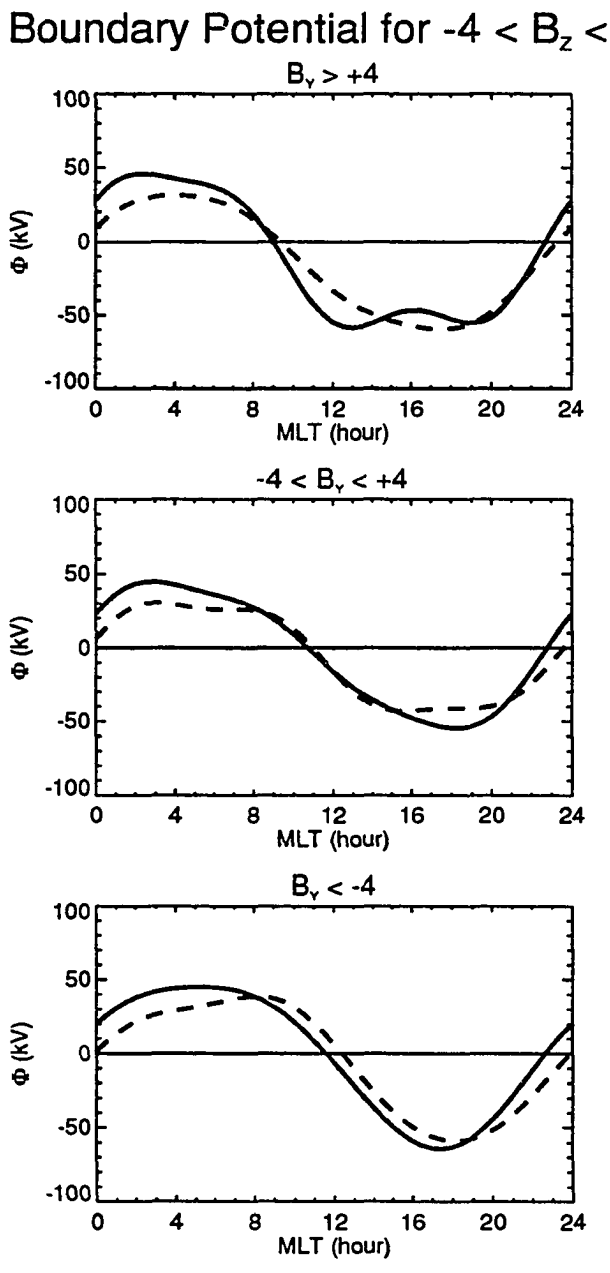

Figure 5.1 Comparison of the electric potential on the continuous convection reversal boundary for the group with $-4 \leq B_z \leq +1$. The upper, middle, and lower graphs represent different B_y ranges. The solid lines represent the results with an intense auroral electrojet. The dash lines represent the results with a weak auroral electrojet.

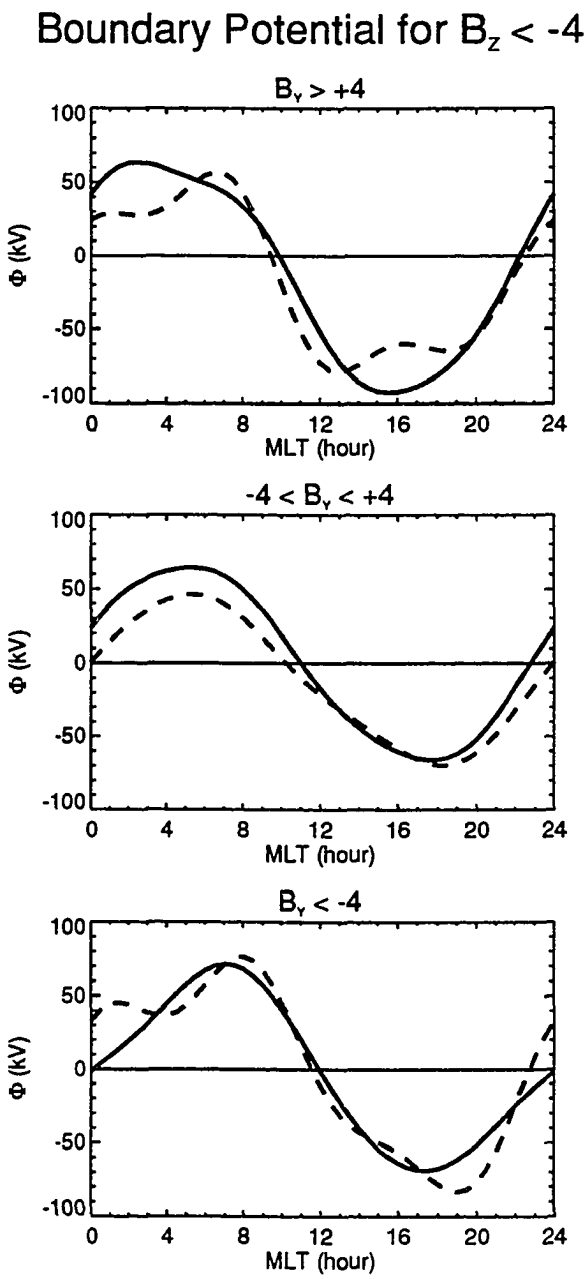

Figure 5.2 Comparison of the electric potential on the continuous convection reversal boundary for the group with $B_z < -4$. The representation of graphs and lines is the same as that in Figure 5.1.

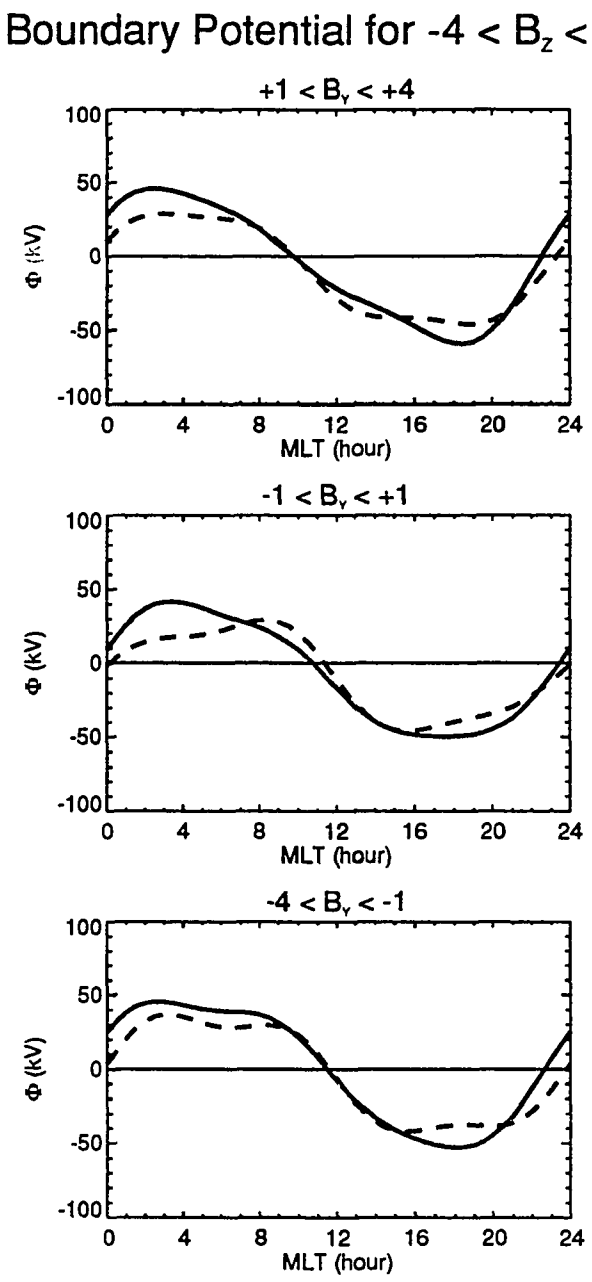

Figure 5.3 Comparison of the electric potential on the continuous convection reversal boundary for the subgroup with $-4 \leq B_z \leq +1$ and $-4 < B_y < +4$. The representation of graphs and lines is the same as that in Figure 5.1.

calculation of solar UV enhancement has been shown in Section 4.3. The Pedersen conductivity model is assumed to be one-half of the Hall conductivity model. Solving (4.8) in the simplified case without field-aligned current except on the fixed convection reversal boundary, a convection pattern is produced, as shown in the upper-right side of Figure 5.4. The fixed boundary potentials and locations were taken from the result of the continuous curve fits for the category ($-4 < B_y < +1$, $-4 < B_z < +1$, and $|AL| < 1.5 \cdot AU$). Furthermore, a conductivity enhancement due to auroral precipitation was added in the conductivity, as shown in the lower-left side of Figure 5.4. This enhancement is assumed to be a Gaussian distribution in latitude and longitude, as discussed in Section 4.3. The peak value of Hall conductivity was chosen to be 15 mho and the ratio of Hall to Pedersen conductivity is 2. The D_ϕ is 90° and ϕ_0 is $-90°$. The θ_0 is fit to the latitude of the continuous boundary and D_θ is 6°. A convection pattern is produced by using this conductivity distribution and the identical boundary conditions, as shown in the lower-right of Figure 5.4. It can be found that the positive and negative reversals no longer meet at midnight. The polarization electric fields due to nonuniform conductivity are responsible for the detachment of the two convection reversals.

The merging, which can generate an electric field, occurs on the duskside in the northern magnetosphere when IMF B_y is positive. A corresponding electric field in the ionosphere can produce a westward component in the plasma flow and cause the convection reversal boundary on the dayside to be discontinuous. The $\mathbf{B} \times \mathbf{V}$ dynamo in the open field lines near the tail lobe can also generate an electric field. A corresponding electric field in the ionosphere can produce a westward component in the plasma flow and cause the convection reversal boundary on the nightside to be discontinuous, as shown in the upper-right graph of Figure 5.5. Similar arguments can be applied to negative IMF B_y. The merging occurs on the dawnside in the northern magnetosphere when IMF B_y is negative. A corresponding electric field in the ionosphere can produce a eastward component in the plasma flow and cause the

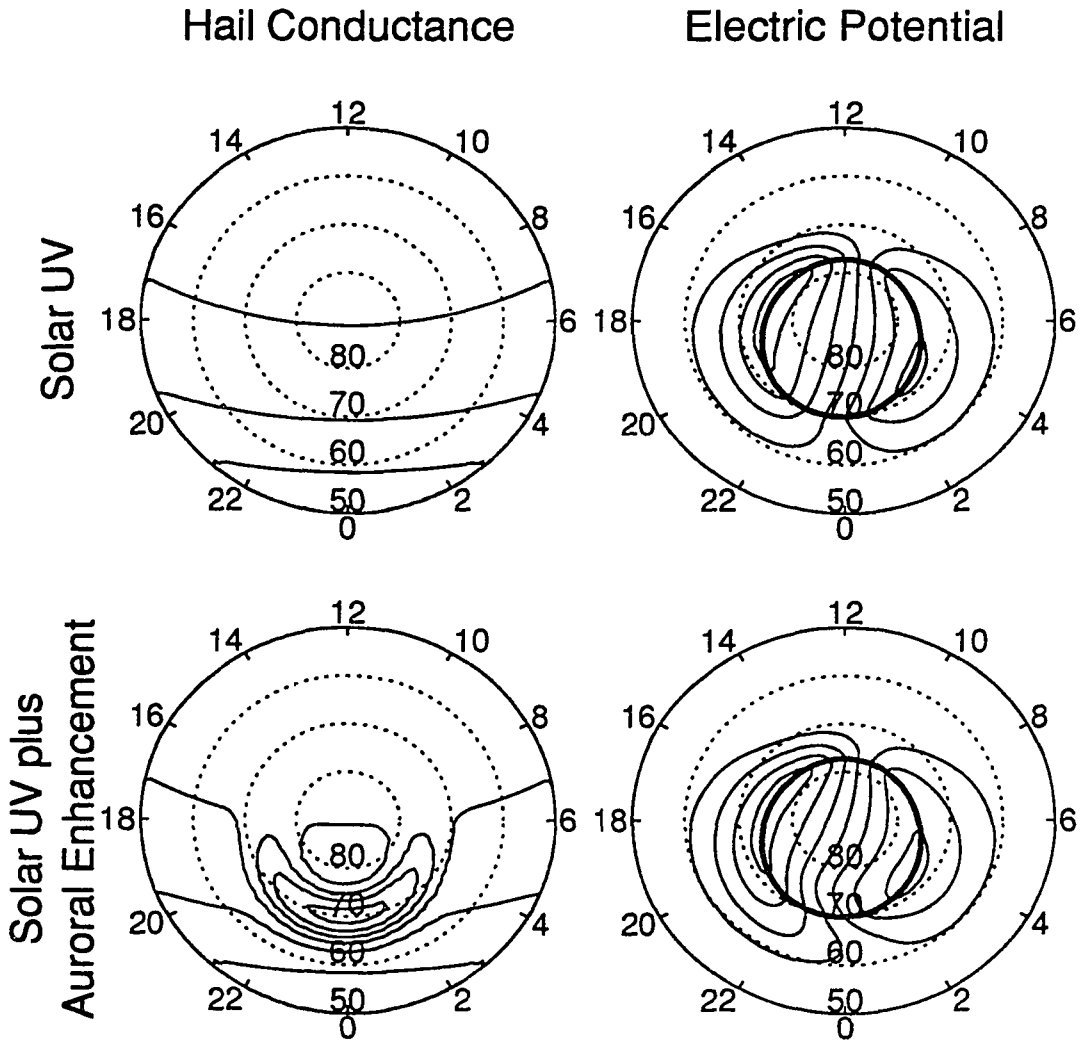

Figure 5.4 Illustration of the relationship between the conductivity and the convection. The upper-left graph shows the conductivity pattern produced only by solar UV radiation in summer solstice. The lower-left graph shows the conductivity pattern with a conductivity enhancement (maximum value is 15 mho). It can be found that the convection pattern is distorted near midnight, as shown on the lower-right side of this figure. The upper-right graph shows no distortion near midnight.

convection reversal boundary on the dayside to be discontinuous. The $\mathbf{B} \times \mathbf{V}$ dynamo in the open field lines near the tail lobe can generate another electric field, but its direction is opposite to the electric field with a positive IMF B_y. A corresponding electric field in the ionosphere can produce a eastward component in the plasma flow and cause the convection reversal on the nightside to be discontinuous, as shown in the upper-left graph of Figure 5.5.

However, the convection is distorted when the plasma flows through a region with a conductivity enhancement on the nightside. For the case with a positive B_y, the convection on the nightside becomes more westward and turns the direction to eastward in the enhancement region, as shown in lower-right graph of Figure 5.5. But for negative B_y, the convection on the nightside becomes more eastward in the enhancement region, as shown in the lower-left graph of Figure 5.5. Comparing the convection patterns for positive and negative IMF B_y, it can be seen the convection patterns on the nightside polar cap are also dependent on the orientation of the IMF B_y. This result is consistent with the observations from sondrestrom radar [*de la Beaujardière et al.*, 1985]. They have shown that the convection for positive B_y is not a mirror effect of the convection for negative B_y. The westward flow was found on the nightside polar cap when the IMF B_y is positive.

In another point of view, an additional convection reversal is found to be detached from the dusk-cell convection reversal on the nightside because of the conductivity enhancement. Also the detachment for positive B_y is larger than the detachment for negative B_y. Since the path of the satellite is random, it may be possible to miss one of the convection reversals. Also, the computer program used in the study were designed to determine only the largest convection reversal in case that there are multiple convection reversals in the measurement. This will result in larger scattering of data points for the case with a positive B_y because the detachment is larger. But for the case with a negative B_y, the detachment is small, the

scattering of data points should be smaller. This feature is consistent with the scatter plots in Figures 3.14-3.16.

As mentioned in subsection 3.3.2, an additional convection reversal, which is detached from the dawn cell, was also found on the dayside. This might be related to the conductivity enhancement due to the precipitation of particles from the low-latitude boundary layer. However, on the dayside the solar UV enhancement has a strong influence on the conductivity . The conductivity enhancement from low-latitude boundary layer is not effective in the case that the background conductivity is large. Unlike the detachment on the nightside, the detachment on the dayside due to particles precipitation is not frequently observed from the data.

The upper-left graph of Figure 5.6 shows the field-aligned current pattern without a region 2 system. The resulting convection pattern is shown in the upper-right graph of Figure 5.6. The lower-left graph of Figure 5.6 shows the field-aligned current pattern with a region 2 system added. Note that the addition of region 2 system to insure the conservation of total field-aligned current. The resulting convection is shown in the lower-right graph of Figure 5.6. Comparing these two convection patterns, it can be seen that the electric field is enhanced in the region between the region 1 and region 2 currents. This is due to the superposition of the same orientation of the electric fields imposed by the region 1 and region 2 currents. The electric field outside the region 2 current is reduced because of the superposition of the opposite electric fields.

In this study all the passes were processed without a detailed inspection. Many erroneous passes were discarded only on the basis that some points were conspicuously out of place and did not conform to a two-cell convection pattern. The simple procedure only locates two extreme values per pass. Actually, more than two convection reversals are frequently seen in the passes traversing near noon-midnight meridian. A more complicated procedure is required to locate every convection reversals and the low-latitude zero-potential boundaries in each pass.

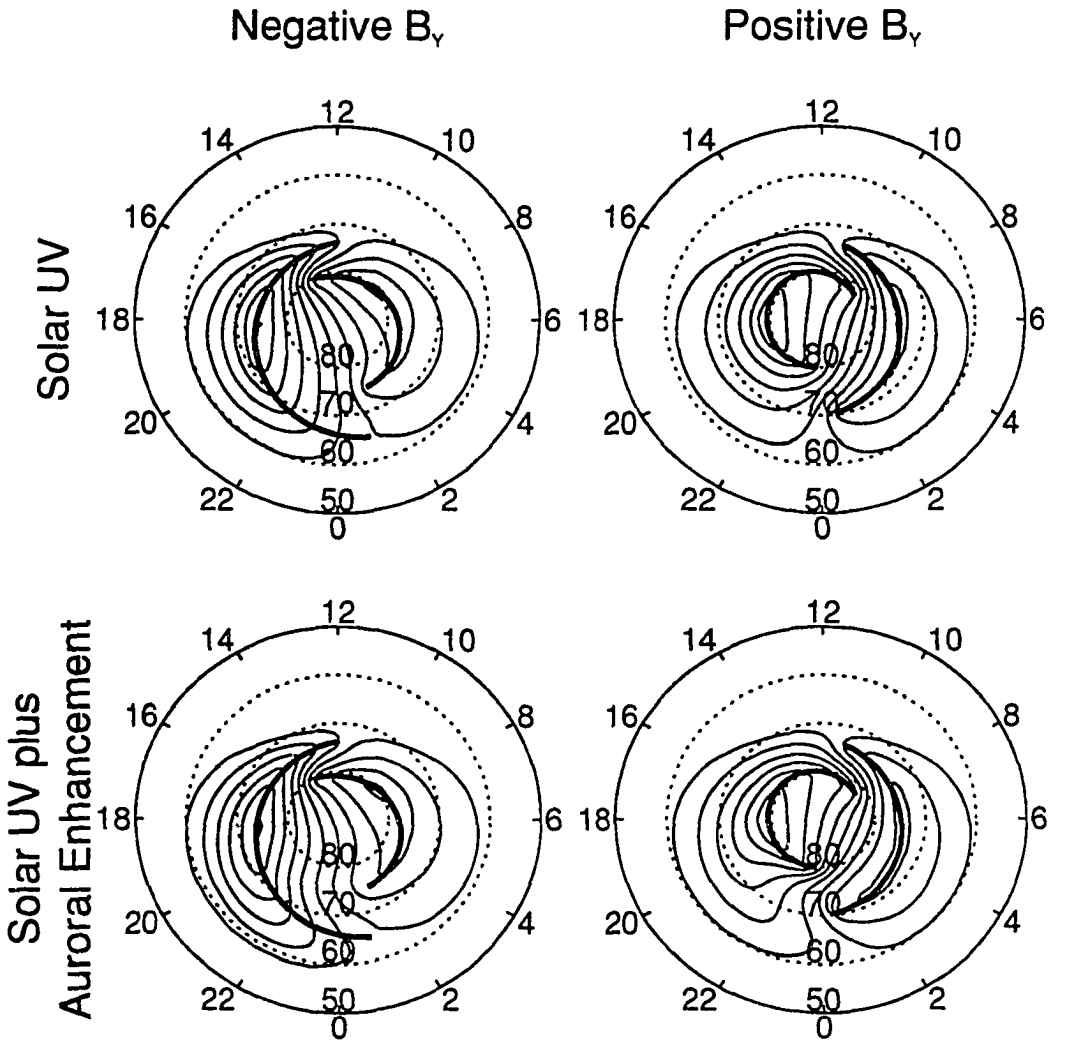

Figure 5.5 Illustration of relationship among the solar wind, the conductivity, and the convection. The conductivity patterns are the same as those in Figure 5.4. The upper-left graph shows the convection pattern imposed by the negative B_y. The upper-right graph shows that convection pattern imposed by the positive B_y. It can be found that an additional convection reversal is detached from the dusk-cell convection reversal, as shown on the lower row of this figure.

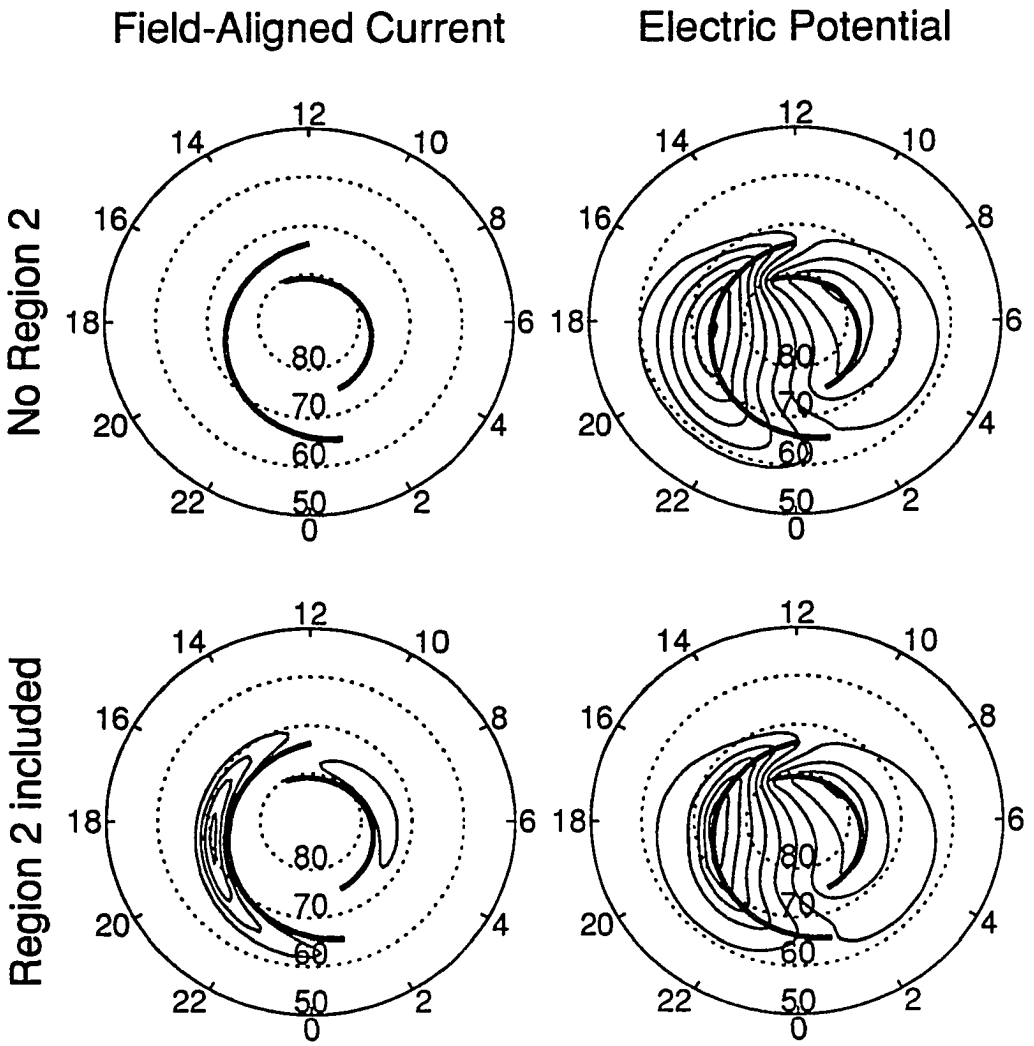

Figure 5.6 Illustration of the relationship between the region 2 field-aligned current and the convection. The conductivity patterns are the same as those in Figure 5.4. The upper-left graph shows the pattern without region 2 current. The electric fields are enhanced in the region between region 1 and region 2 currents when the region 2 field-aligned current is added, as shown on the lower row of this figure.

Also the passes for the $AU_C < 100$, corresponding to lower polar cap potential and smaller polar cap size, could be added. It may be possible to use this procedure of mapping of the convection reversals to study the distorted, multi-cell patterns associated with the northward B_z.

CHAPTER 6

Conclusion

As indicated in Section 1.3, the objective of the thesis is to reproduce the ionospheric convection patterns under different combinations of geomagnetic activity and solar wind conditions, and to study the effects of southward IMF on the relationships among the auroral electrojet, the ionospheric conductivity, and the ionospheric convection. The DE-2 satellite has provided *insitu* observations on the ionospheric electric fields at all local time. These data have been used to determine how the potential is distributed around the convection reversal boundary and its location, which served as the boundary conditions of a simple model of calculating the electric potential in the high-latitude region. Also, the IMF data from IMP-8 or ISEE-3 and the geomagnetic indices (AU and AL) have been used to group the random electric field measurements into 18 categories. A series of data criteria were imposed on the original data in order to eliminate the passes with "bad" data. The following conclusions can be reached through the resulting ionospheric convection patterns:

1. The IMF B_y mainly affects the geometry of the convection reversal boundary. It can be seen that the IMF B_y affects the orientation of the dayside "throat" and produces westward or eastward flow across the noon-midnight meridian. The two-cell convection pattern rotates clockwise as IMF B_y changes from negative to positive. The polar cap potential and size increase as the southward B_z increases. These results are consistent with the previous studies about the relationship between the IMF and ionospheric convection.

2. As the westward electrojet gets more intense, the maximum dawn potential increases and shifts towards midnight. Also the westward electric field is enhanced near midnight and the zero-potential line shifts towards premidnight. These are all related to an intrusion of the

dawn cell into the dusk cell. The enhanced westward electric field is related to an increased earthward plasma sheet convection, which is driven by an enhanced dawn-to-dusk electric field in the plasma sheet during substorms. As shown in [*Weimer*, 1993], this westward electric field near midnight increases the Pedersen current in the westward electrojet. This suggests that the westward electrojet is a combination of the Pedersen and Hall currents.

3. Conductivity enhancement around the auroral oval generates a polarization electric field. This polarization electric field adds to the original convection electric field, and results in a distortion of the convection pattern and an intrusion of dawn cell to dusk cell, and an apparent separation of convection reversals near midnight. At this point it becomes apparent, the conductivity enhancement is responsible for the distortion of the convection.

4. The merging associated electric field in the dayside cusp and the $\mathbf{B} \times \mathbf{V}$ associated electric field in the nightside polar cap have a component which is perpendicular to the dawn-to-dusk direction when the IMF B_y is positive or negative. These electric fields can produce the westward or eastward flow and cause the convection reversal to be discontinuous. The convection is distorted when the plasma flows through the region with a conductivity enhancement on the nightside. This can result in an additional convection reversal, which is detached from the dusk-cell convection reversal. The additional convection reversal is clear for the patterns with a positive IMF B_y. Comparing the convection patterns on the nightside for positive and negative IMF B_y, the difference is is significant. The westward flow is found in the nightside polar cap when the IMF B_y is positive.

5. The main feature of two-cell ionospheric convection is dominated by the region 1 field-aligned current. But the region 2 field-aligned current may modify the convection outside the convection reversal boundary. The electric field is enhanced in the region between region 1 and region 2 currents.

6. From the points of the distortion of the convection on the nightside and the "throat" feature on the dayside, the convection reversal could be multiple. It is much better to fit the maximum and minimum potential points with two separate functions than to fit the data with only one function. The convection patterns with a discontinuous reversal is more realistic than the convection patterns with a continuous reversal.

APPENDIX A

Least-Squares Fitting

The data are fit in a given time with a Fourier series. The Fourier form used as follows

$$f(\theta) = S(1) + S(2)\cos[\theta - S(3)] \qquad (A.1)$$

where S(1),S(2) and S(3) are the parameters which needs to be determined, and θ is a arbitrary variable. We use the least-squares method to determine these parameters, in order to obtain a function to best describe the data. The least-squares criterion is to minimize the function

$$L = \sum_{i=1}^{n}(Y_i - Y_i')^2 \qquad (A.2)$$

where Y_i is the experimental value and Y_i' is the value of the generated function. If we let

$$Y_i' = f(\theta_i) = a_0 + a_1\cos\theta + a_2\sin\theta. \qquad (A.3)$$

Substituting (A.3) into (A.2), thus

$$L = \sum_{i=1}^{n}(Y_i - a_0 - a_1\cos\theta_i - b_1\sin\theta_i)^2. \qquad (A.4)$$

We minimize L as a function of a_0, a_1 and a_2 by taking partials, $\partial L/\partial a_0$, $\partial L/\partial a_1$, and

$\partial L/\partial b_1$, then setting the partials zero

$$\frac{\partial L}{\partial a_0} = -2\sum_{i=1}^{n}(Y_i - a_0 - a_1\cos\theta_i - b_1\sin\theta_i) = 0 \qquad (A.5)$$

$$\frac{\partial L}{\partial a_1} = -2\sum_{i=1}^{n}(Y_i - a_0 - a_1\cos\theta_i - b_1\sin\theta_i)(-\cos\theta_i) = 0 \qquad (A.6)$$

$$\frac{\partial L}{\partial b_1} = -2\sum_{i=1}^{n}(Y_i - a_0 - a_1\cos\theta_i - b_1\sin\theta_i)(-\sin\theta_i) = 0 \qquad (A.7)$$

rearranging (A.5), (A.6), and (A.7)

$$\sum_{i=1}^{n} Y_i = Na_0 + a_1\sum_{i=1}^{n}\cos\theta_i + b_1\sum_{i=1}^{n}\sin\theta_i \qquad (A.8)$$

$$\sum_{i=1}^{n} Y_i\cos\theta_i = a_0\sum_{i=1}^{n}\cos\theta_i + a_1\sum_{i=1}^{n}\cos^2\theta_i + b_1\sum_{i=1}^{n}\cos\theta_i\sin\theta_i \qquad (A.9)$$

$$\sum_{i=1}^{n} Y_i\sin\theta_i = a_0\sum_{i=1}^{n}\sin\theta_i + a_1\sum_{i=1}^{n}\cos\theta_i\sin\theta_i + b_1\sum_{i=1}^{n}\sin^2\theta_i. \qquad (A.10)$$

The equations (A.8), (A.9) and (A.10) are the set of simultaneous equations. We need to calculate the summation in the desired interval and solve the system of equations to find a_0, a_1 and b_1. The equation (A.3) may be rewritten in the form

$$f(\theta) = a_0 + \sqrt{a_1^2 + b_1^2}\left(\frac{a_1}{\sqrt{a_1^2 + b_1^2}}\cos\theta + \frac{b_1}{\sqrt{a_1^2 + b_1^2}}\sin\theta\right)$$

or

$$f(\theta) = a_0 + \sqrt{a_1^2 + b_1^2}\cos[\theta - \tan^{-1}(\frac{b_1}{a_1})]. \qquad (A.11)$$

The coefficients of (A.1) can be defined in terms of the parameters found by the solutions of the equations

$$S(1) = a_0 \qquad (A.12)$$

$$S(2) = \sqrt{a_1^2 + b_1^2} \qquad (A.13)$$

$$S(3) = \tan^{-1}(\frac{b_1}{a_1}). \qquad (A.14)$$

APPENDIX B

Numerical Scheme for Solving Laplace Equation in Rectangular Coordinates

Laplace equation (4.9) in rectangular coordinates in two dimensions

$$\frac{\partial^2 \Phi}{\partial x^2} + \frac{\partial^2 \Phi}{\partial y^2} = 0. \qquad (B.1)$$

Rewriting (B.1) in a finite difference representation using central differences, we have

$$\frac{\Phi_{j+1,k} - 2\Phi_{j,k} + \Phi_{j-1,k}}{(\Delta x)^2} + \frac{\Phi_{j,k+1} - 2\Phi_{j,k} + \Phi_{j,k-1}}{(\Delta y)^2} = 0 \qquad (B.2)$$

where j is index for axis x, k is index for axis y. Multiplying (B.2) by $(\Delta x)^2$, thus

$$\Phi_{j+1,k} - 2\Phi_{j,k} + \Phi_{j-1,k} + \frac{(\Delta x)^2}{(\Delta y)^2}(\Phi_{j,k+1} - 2\Phi_{j,k} + \Phi_{j,k-1}) = 0. \qquad (B.3)$$

Setting $\Delta x = \Delta y$ and Solving (B.3) for $\Phi_{j,k}$, yields

$$\Phi_{j,k} = \frac{1}{4}(\Phi_{j+1,k} + \Phi_{j-1,k} + \Phi_{j,k+1} + \Phi_{j,k-1}). \qquad (B.4)$$

To show how successive over-relaxation can be applied to Laplace equation, we begin with (B.4), adding superscript to show a new value computed from previous iterations, we have

$$\Phi_{j,k}^{(i+1)} = \frac{1}{4}(\Phi_{j+1,k}^{(i)} + \Phi_{j-1,k}^{(i)} + \Phi_{j,k+1}^{(i)} + \Phi_{j,k-1}^{(i)}). \qquad (B.5)$$

The method of successive over-relaxation can improve the speed of convergence. We both add and subtract $\Phi_{j,k}^{(i)}$ on the righthand side of (B.5) and add an over-relaxation factor λ

to get a new iteration relation, getting

$$\Phi_{j,k}^{(i+1)} = \Phi_{j,k}^{(i)} + \frac{\lambda}{4}(\Phi_{j+1,k}^{(i)} + \Phi_{j-1,k}^{(i)} + \Phi_{j,k+1}^{(i)} + \Phi_{j,k-1}^{(i)} - 4\Phi_{j,k}^{(i)}). \qquad (B.6)$$

The value of the factor is between 1 and 2. The optimum over-relaxation factor λ can be estimated by

$$\lambda = \frac{2}{1 + (1 - \omega^2)^{1/2}} \qquad (B.7)$$

where is determined as follows. Let

$$Y_{j,k}^{i} = \Phi_{j,k}^{(i+1)} - \Phi_{j,k}^{(i)}. \qquad (B.8)$$

A norm of $Y^{(i+1)}$ is given by

$$\| Y^{(i+1)} \| = \sum_{j=1}^{n} \sum_{k=1}^{n} |Y_{j,k}^{(i+1)}|. \qquad (B.9)$$

Now

$$\frac{\| Y^{(i+1)} \|}{\| Y^{(i)} \|} \rightarrow \omega^2 \qquad \text{as } i \rightarrow 0. \qquad (B.10)$$

The iteration terminates when the norm, or sum of the residual is less than the error per step times the initial value of norm.

APPENDIX C

Numerical Scheme for Solving Laplace's Equation in Polar Coordinates

Laplace's equation in polar coordinates is

$$\frac{\partial^2\Phi}{\partial r^2}+\frac{1}{r}\frac{\partial\Phi}{\partial r}+\frac{1}{r^2}\frac{\partial^2\Phi}{\partial\theta^2}=0. \tag{C.1}$$

Rewriting (C.1) in a finite difference representation using central differences, we have

$$\begin{aligned}\frac{\Phi_{j+1,k}-2\Phi_{j,k}+\Phi_{j-1,k}}{(\Delta r)^2}+\frac{1}{r_j}\Big[\frac{\Phi_{j+1,k}-\Phi_{j-1,k}}{2(\Delta r)}\Big]\\ +\frac{1}{r_j^2}\Big[\frac{\Phi_{j,k+1}-2\Phi_{j,k}+\Phi_{j,k-1}}{(\Delta\theta)^2}\Big]=0\end{aligned} \tag{C.2}$$

where j is index for latitude, k is index for azimuthal angle. Multiplying (C.2) by $(\Delta r)^2$, thus

$$\begin{aligned}\Phi_{j+1,k}-2\Phi_{j,k}+\Phi_{j-1,k}+\frac{\Delta r}{2r_j}(\Phi_{j+1,k}-\Phi_{j-1,k})\\ +\frac{(\Delta r)^2}{r_j^2(\Delta\theta)^2}(\Phi_{j,k+1}-2\Phi_{j,k}+\Phi_{j,k-1})=0.\end{aligned} \tag{C.3}$$

Solving (C.3) for $\Phi_{j,k}$, yields

$$\begin{aligned}\Phi_{j,k}=\frac{1}{[2+\frac{2(\Delta r)^2}{r_j^2(\Delta\theta)^2}]}\Big\{(1+\frac{\Delta r}{2r_j})\Phi_{j+1,k}+(1-\frac{\Delta r}{2r_j})\Phi_{j-1,k}\\ +\Big[\frac{(\Delta r)^2}{r_j^2(\Delta\theta)^2}\Big](\Phi_{j,k+1}+\Phi_{j,k-1})\Big\}.\end{aligned} \tag{C.4}$$

To show how successive over-relaxation can be applied to Laplace's equation, we begin with (C.4), Adding superscripts to show a new value computed from previous iterations, we have

$$\begin{aligned}\Phi_{j,k}^{(i+1)}=\frac{1}{[2+\frac{2(\Delta r)^2}{r_j^2(\Delta\theta)^2}]}\Big\{(1+\frac{\Delta r}{2r_j})\Phi_{j+1,k}^{(i)}+(1-\frac{\Delta r}{2r_j})\Phi_{j-1,k}^{(i)}\\ +\Big[\frac{(\Delta r)^2}{r_j^2(\Delta\theta)^2}\Big](\Phi_{j,k+1}^{(i)}+\Phi_{j,k-1}^{(i)})\Big\}.\end{aligned} \tag{C.5}$$

The method of successive over-relaxation can improve the speed of convergence. We both add and subtract $\Phi_{j,k}^{(i)}$ on the righthand side and add an over-relaxation factor λ to get a

new iteration relation, getting

$$\Phi_{j,k}^{(i+1)} = \Phi_{j,k}^{(i)} + \frac{\lambda}{[2+\frac{2(\Delta r)^2}{r_j^2(\Delta\theta)^2}]}\Big\{(1+\frac{\Delta r}{2r_j})\Phi_{j+1,k}^{(i)} + (1-\frac{\Delta r}{2r_j})\Phi_{j-1,k}^{(i)} + \Big[\frac{(\Delta r)^2}{r_j^2(\Delta\theta)^2}\Big](\Phi_{j,k+1}^{(i)} + \Phi_{j,k-1}^{(i)}) - \Big[2+\frac{2(\Delta r)^2}{r_j^2(\Delta\theta)^2}\Big]\Phi_{j,k}^{(i)}\Big\}. \quad (C.6)$$

The value of factor is between 1 and 2. The optimum λ can be estimated by the method discussed in Appendix B. The iteration terminates when the norm is less than the error per step times the initial value of the norm.

The boundaries are fit to the nearest grid points. The averaged error per grid points in polar coordinates is 0.23 degree. The error in rectangular coordinates is 0.33 degree. Both are not bad for studying the large-scale convection. The rectangular coordinates were used in order to get better convergence at the origin, and for a convenient interface with the plotting contour software. The Figure C.1 shows a comparison between the rectangular and polar coordinates. The dash lines in this figure represent the potential contours in polar coordinates and the solid lines represent the potential contours in rectangular coordinates. It can be shown that the difference between two coordinates is small.

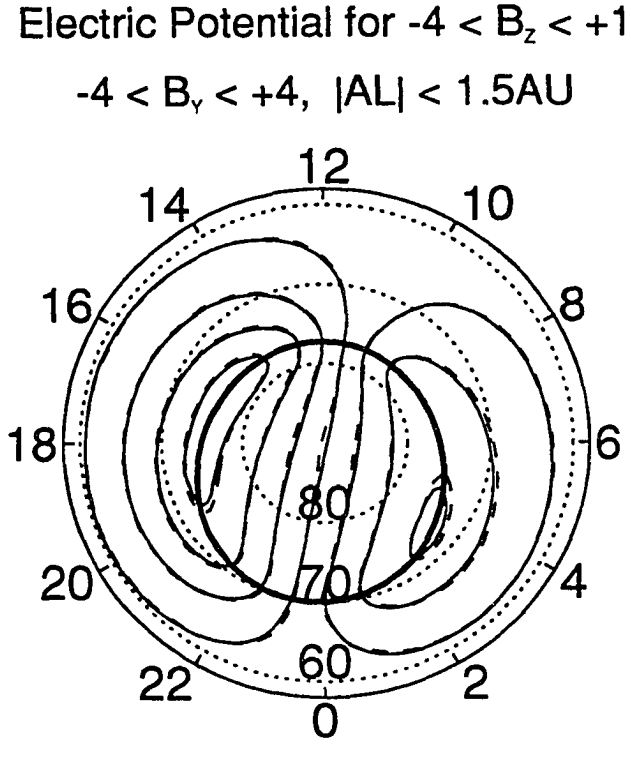

Figure C.1 Comparison between the polar and rectangular coordinates. The dash lines represent the potential contours in polar coordinates. The solid lines represent the potential contours in rectangular coordinates. The result shows the difference between these two coordinates is small.

APPENDIX D

Calculation of Solar Zenith Angle χ

Since the rotation of the earth to sun with a period of 365.25 days and the self rotation of the earth about its axis once every 24 hours, the dipole tilt angle varies with universal time (UT) and day of year (DOY). The expressions are as follows

$$\psi_{yr} = 23.4 \cos\left[(DOY - 172)\frac{2\pi}{365.25}\right] \qquad (D.1)$$

$$\psi_{day} = 11.2 \cos\left[(UT - 16.72)\frac{2\pi}{24}\right] \qquad (D.2)$$

where ψ_{yr} is the seasonal dipole tilt angle and ψ_{day} is the daily dipole tilt angle. The total tilt angle, μ, is the sum of the seasonal and daily tilt angles. We have

$$\mu = \psi_{yr} + \psi_{day}. \qquad (D.3)$$

The total tilt angle is used for the conversion of GSM and SM coordinates. The geocentric solar magnetospheric coordinate system (GSM) has its x-axis from the earth to the sun. The y-axis is defined to be perpendicular to the earth's magnetic dipole so that the x-z plane contains a dipole axis. Another coordinate system is solar magnetic coordinates (SM). The z-axis is chosen as the north magnetic pole and the y-axis is perpendicular to the earth-sun line towards dusk. The difference between GM and GSM systems is a rotation about the y-axis. The amount of the rotation is simply the total dipole tilt angle. Note that the x-axis of this

system does not point directly at the sun [*Russell*, 1971]. The conversion becomes

$$\begin{pmatrix} X \\ Y \\ Z \end{pmatrix}_{GSM} = \begin{pmatrix} \cos\mu & 0 & \sin\mu \\ 0 & 1 & 0 \\ -\sin\mu & 0 & \cos\mu \end{pmatrix} \begin{pmatrix} X \\ Y \\ Z \end{pmatrix}_{SM} \tag{D.4}$$

converting the magnetic colatitude and local time to cartesian SM coordinates. We have

$$\begin{pmatrix} X \\ Y \\ Z \end{pmatrix}_{SM} = \begin{pmatrix} \sin\theta\cos\phi \\ \sin\theta\cos\phi \\ \cos\theta \end{pmatrix} \tag{D.5}$$

where θ is the colatitude and ϕ is the longitude. Note that 12 hours MLT is equal to 0° longitude. Substitute (D.5) into (D.4), thus

$$\begin{pmatrix} X \\ Y \\ Z \end{pmatrix}_{GSM} = \begin{pmatrix} \cos\mu & 0 & \sin\mu \\ 0 & 1 & 0 \\ -\sin\mu & 0 & \cos\mu \end{pmatrix} \begin{pmatrix} \sin\theta\cos\phi \\ \sin\theta\sin\phi \\ \cos\theta \end{pmatrix} \tag{D.6}$$

or

$$\begin{pmatrix} X \\ Y \\ Z \end{pmatrix}_{GSM} = \begin{pmatrix} \sin\theta\cos\phi\cos\mu + \cos\theta\sin\mu \\ \sin\theta\sin\phi \\ -\sin\theta\cos\phi\sin\mu + \cos\theta\cos\mu \end{pmatrix}. \tag{D.7}$$

The solar zenith angle is denoted as the angle between the position unit vector $\mathbf{P}$ and the unit vector $\mathbf{S}$ from earth to sun. Since the x-axis of GSM coordinates points toward sun, the dot product of $\mathbf{P}$ and $\mathbf{S}$ is equal to $P_{X_{GSM}}$, where $P_{X_{GSM}}$ is the x coordinate of the $\mathbf{P}$ position unit vector, in GSM coordinates. The solar zenith angle at the position $\mathbf{P}$ is

$$\begin{aligned} \chi &= \cos^{-1}(\mathbf{P}\cdot\mathbf{S}) \\ &= \cos^{-1}(P_{X_{GSM}}) \\ &= \cos^{-1}(\sin\theta\cos\phi\cos\mu + \cos\theta\sin\mu). \end{aligned} \tag{D.8}$$

APPENDIX E

Numerical Scheme for Solving the Inhomogeneous Current Continuity Equation

The inhomogeneous current continuity equation (4.8) in two-dimension rectangular coordinates

$$\Sigma_P(\frac{\partial^2\Phi}{\partial x^2}+\frac{\partial^2\Phi}{\partial y^2})+(\nabla\Sigma_P)_x\frac{\partial\Phi}{\partial x}+(\nabla\Sigma_P)_y\frac{\partial\Phi}{\partial y}+(\nabla\Sigma_H)_x\frac{\partial\Phi}{\partial y}-(\nabla\Sigma_H)_y\frac{\partial\Phi}{\partial x}=-j_{\parallel} \quad (E.1)$$

where $j_{\parallel}$ is the field-aligned current (positive for the downward current) and

$$(\nabla\Sigma_P)_x=\frac{\partial\Sigma_p}{\partial x}$$
$$(\nabla\Sigma_P)_y=\frac{\partial\Sigma_P}{\partial y}$$
$$(\nabla\Sigma_H)_x=\frac{\partial\Sigma_H}{\partial x}$$
$$(\nabla\Sigma_H)_y=\frac{\partial\Sigma_H}{\partial y}.$$

Rewriting (E.1) in a finite difference representation, we have

$$\begin{aligned}&\Sigma_P[\frac{\Phi_{j+1,k}-2\Phi_{j,k}+\Phi_{j-1,k}}{(\Delta x)^2}]+\Sigma_P[\frac{\Phi_{j,k+1}-2\Phi_{j,k}+\Phi_{j,k-1}}{(\Delta y)^2}]+\\&[(\nabla\Sigma_P)_x-(\nabla\Sigma_H)_y](\frac{\Phi_{j+1,k}-\Phi_{j-1,k}}{2\Delta x})+\\&[(\nabla\Sigma_P)_y-(\nabla\Sigma_H)_x](\frac{\Phi_{j,k+1}-\Phi_{j,k-1}}{2\Delta y})=-j_{\parallel}\end{aligned} \quad (E.2)$$

where j is the index for axis x and k is the index for axis y. Multiplying (E.2) by $(\Delta x)^2$, thus

$$\begin{aligned}&\Sigma_P(\Phi_{j+1,k}-2\Phi_{j,k}+\Phi_{j-1,k})+\Sigma_P(\frac{\Delta x}{\Delta y})^2(\Phi_{j,k+1}-2\Phi_{j,k}+\Phi_{j,k-1})+\\&[(\nabla\Sigma_P)_x-(\nabla\Sigma_H)_y](\frac{\Delta x}{2})(\Phi_{j+1,k}-\Phi_{j-1,k})+\\&[(\nabla\Sigma_P)_y+(\nabla\Sigma_H)_x](\frac{\Delta x}{2\Delta y})(\Phi_{j,k+1}-\Phi_{j,k-1})=-j_{\parallel}.\end{aligned} \quad (E.3)$$

Setting $\Delta x=\Delta y$ and solving (E.3) for $\Phi_{j,k}$, yields

$$\Phi_{j,k} = A\Phi_{j+1,k} + B\Phi_{j-1,k} + C\Phi_{j,k+1} + D\Phi_{j,k-1} + Ej_{\|} \qquad (E.4)$$

where

$$A = \frac{2\Sigma_P + \Delta x[(\Sigma_P)_x - (\Sigma_H)_y]}{8\Sigma_P}$$

$$B = \frac{2\Sigma_P - \Delta x[(\Sigma_P)_x - (\Sigma_H)_y]}{8\Sigma_P}$$

$$C = \frac{2\Sigma_P + (\Sigma_P)_y + (\Sigma_H)_x}{8\Sigma_P}$$

$$D = \frac{2\Sigma_P - (\Sigma_P)_y - (\Sigma_H)_x}{8\Sigma_P}$$

$$E = \frac{1}{4\Sigma_P}.$$

Similarly for solving the Laplace equation in Appendix B, we use the successive over-relaxation method. Adding the superscript to show a new value computed from the previous value, we have

$$\Phi_{j,k}^{(i+1)} = A\Phi_{j+1,k}^{(i)} + B\Phi_{j-1,k}^{(i)} + C\Phi_{j,k+1}^{(i)} + D\Phi_{j,k-1}^{(i)} + Ej_{\|}^{(i)}. \qquad (E.5)$$

We both add and subtract $\Phi_{j,k}^{(i)}$ on the righthand side of (E.5) and add an over-relaxation factor λ to get a new iteration relation, getting

$$\Phi_{j,k}^{(i+1)} = \Phi_{j,k}^{(i)} + \lambda(A\Phi_{j+1,k}^{(i)} + B\Phi_{j-1,k}^{(i)} + C\Phi_{j,k+1}^{(i)} + D\Phi_{j,k-1}^{(i)} + Ej_{\|}^{(i)} - \Phi_{j,k}^{(i)}). \qquad (E.6)$$

The value of factor is between 1 and 2. The optimum λ can be estimated by the method discussed in Appendix B. The iteration terminates when the norm is less than the error per step times the initial value of the norm.

REFERENCES

Baker, K. B., and S. Wing, A new magnetic coordinate system for conjugate studies at high latitudes, J. Geophys. Res., 94, 9139-9143, 1989.

Bargatze, L. F., D. N. Baker, R. L. McPherron, and E. W. Hones, Jr., Magnetospheric impulse response for many levels of geomagnetic activity, J. Geophys. Res., 90, 6387-6394, 1985.

Bargatze, L. F., R. L. McPherron, and D. N. Baker, Solar wind-magnetosphere energy input functions, in solar Wind-Magnetosphere Coupling, edited by Y. Kamide and J. A. Slavin, p. 101-109, D. Reidel, 1986.

Blomberg, L. G., and G. T. Marklund, The influence of conductivities consistent with field-aligned currents on high-latitude convection patterns, J. Geophys. Res., 93, 14,493-14,499, 1988.

Clauer, C. R., P. M. Banks, A. Q. Smith, T. S. Jorgensen, E. Friis-Christensen, S. Vennerstrom, V. B. Wickwar, J. D. Kelly, and J. Doupnik, Observation of interplanetary magnetic field and of ionospheric plasma convection in the vicinity of the dayside polar cleft, Geophys. Res. Lett., 9, 891-894, 1984.

Clauer, C. R., and Y. Kamide, DP 1 and DP 2 current systems for the march 22, 1979 substorms, J. Geophys. Res., 90, 1343-1354, 1985.

Coroniti, F. V., and C. F. Kennel, Polarization of the auroral electrojet, J. Geophys. Res., 77, 2835-2850, 1972.

Couzens, D. A., and J. H. King, Interplanetary Medium Data Book - Supplement 3A, 1977 - 1985, National Space Science Data Center, GSFC/NASA, Greenbelt, MD, 1986.

Crooker, N. U., Dayside merging and cusp geometry, J. Geophys. Res., 84 951-959, 1979.

Davis, T. N., and M. Sugiura, Auroral electrojet activity index AE and its universal time variations, J. Geophys. Res., 71, 785-801, 1966.

de la Beaujardière, O., V. B. Wickwar, J. D. Kelly, and J. H. King, Effect of the interplanetary magnetic field y component on the high-latitude nightside convection, Geophys. Res. Lett., 12, 461-464, 1985.

de la Beaujardière, O., D. Alcayde, J. Fontanari, and C. Leger, Seasonal dependence of high-latitude electric field, J. Geophys. Res., 96, 5723-5735, 1991a.

de la Beaujardière, O., R. Johnson, and V. B. Wickwar, Ground-based measurements of Joule heating rates, in Auroral Physics, edited by C. -I. Meng, M. J. Rycroft, and L. A. Frank, p. 439-448, Cambridge UP, 1991b.

Doyle, M. A., and W. J. Burke, S3-2 measurements of the polar cap potential, J. Geophys. Res., 88, 9125-9133, 1983.

Dungey, J. W., Interplanetary magnetic field and auroral zones, Phys. Rev. Lett., 6, 47-48, 1961.

Foster, J. C., An empirical electric field model derived from Chatanika radar data, J. Geophys. Res., 88, 981-987, 1983.

Foster, J. C., Ionospheric signatures of magnetospheric convection, J. Geophys. Res., 89, 855-865, 1984.

Foster, J. C., J. M. Holt, and R. G. Musgrove, Ionospheric convection associated with discrete levels of particle precipitation, Geophys. Res. Lett., 13, 656-659, 1986.

Foster, J. C., T. Fuller-Rowell, and D. S. Evans, Quantitative patterns of large-scale field-aligned currents in the auroral ionosphere, J. Geophys. Res., 94, 2555-2564, 1989.

Frank, L. A., and J. D. Craven, Imaging results from dynamics explorer 1, Rev. Geophys., 26, 249-283, 1988.

Fujii, R., T. Iijima, T. A. Potemra, and M. Sugiura, Seasonal dependence of large-scale Birkeland currents, Geophys. Res. Lett., 8, 1103-1106, 1981.

Fujii, R., and T. Iijima, Control of the ionospheric conductivities on large-scale Birkeland current intensities under geomagnetic quiet conditions, J. Geophys. Res. 92, 4505-4513, 1987.

Fuller-Rowell, T. J., and D. S. Evans, Height-integrated Pedersen and Hall conductivity patterns inferred from the TIROS-NOAA satellite data, J. Geophys. Res., 92, 7606-7618, 1987.

Gustafsson, G., Corrected geomagnetic coordinates for epoch 1980, in Magnetospheric Currents, edited by T. A. Potemra, pp. 276-283, AGU, Washington, DC, 1984.

Hairston, M. R., and R. A. Heelis, Model of the high-latitude ionospheric convection pattern during southward interplanetary magnetic field using DE 2 data, J. Geophys. Res., 95, 2333-2343, 1990.

Hardy, D. A., M. S. Gussenhoven, and R. Raistrick, Statistical and functional representations of the pattern of auroral energy flux, number flux, and conductivity, J. Geophys. Res., 92, 12,275-12,294, 1987.

Heelis, R. A., J. D. Winningham, W. B. Hanson, and J. L. Burch, The relationships between high-latitude convection reversals and the energetic particle morphology observed by Atmospheric Explorer, J. Geophys. Res., 85, 3315-3324, 1980.

Heelis, R. A., J. K. Lowell, and R. W. Spiro, A model of the high-latitude ionospheric convection pattern, J. Geophys. Res., 87, 6339-6345, 1982.

Heppner, J. P., Empirical models of high-latitude electric fields, J. Geophys. Res., 82, 1115-1125, 1977.

Heppner, J. P., and N. C. Maynard, Empirical high-latitude electric field models, J. Geophys. Res., 92, 4467-4489, 1987.

Holt, J. M., R. H. Wand, J. V. Evans, and W. L. Oliver, Empirical models for the plasma convection at high latitudes from Millstone Hill Observations, J. Geophys. Res., 92, 203-212, 1987.

Iijima, T., and T. A. Potemra, The amplitude distribution of field-aligned currents at northern high latitudes observed by Triad, J. Geophys. Res., 81, 2165-2174, 1976.

Iijima, T., and T. A. Potemra, Large-scale characteristics of field-aligned currents associated with substorms, J. Geophys. Res., 83, 599-615, 1978.

Kamide, Y., The auroral electrojets: relative importance of ionospheric conductivities and electric fields, in Auroral Physics, edited by C. -I. Meng, M. J. Rycroft, and L. A. Frank, p. 385-399, Cambridge UP, 1991.

Kan, J. R., Y. Kamide, Electrodynamics of the westward traveling surge, J. Geophys. Res., 90, 7615-7619, 1985.

Kan, J. R., L. Zhu, and S.-I. Akasofu, A theory of substorms: onset and subsidence, J. Geophys. Res., 93, 5624-5640, 1988.

Kelly, M. C., The Earth's Ionosphere, Academic Press, San Diego, 1989.

Lockwood, M., S. W. H. Cowley, and M. P. Freeman, The excitation of plasma convection in the high-latitude ionosphere, J. Geophys. Res., 95, 7961-7972, 1990.

Lockwood, M., On flow reversal boundaries and transpolar voltage in average models of high-latitude convection, Planet. Space Sci., 39, 397-409, 1991.

Lu, G., P. H. Reiff, M. R. Hairston, R. A. Heelis, and J. L. Karty, Distribution of convection potential around the polar cap boundary as a function of the interplanetary magnetic field, J. Geophys. Res., 94, 13,447-13,461, 1989.

Marklund, G. T, L. G. Blomberg, K. Stasiewicz, J. S. Murphree, R. Pottelette, L. J. Zanetti, T. A. Potemra, D. A. Hardy, and F. J. Rich, Snapshots of high-latitude electrodynamics using Viking and DMSP F7 observations, J. Geophys. Res., 93, 14,479-14,492, 1988.

Maynard, N. C., Electric field measurements across the Harang discontinuity, J. Geophys. Res., 79, 4620-4631, 1974.

Maynard, N. C., E. A. Bielecki, and H. F. Burdick, Instrumentation for vector electric field measurements from DE-B, Space Sci. Instrum., 5, 523-534, 1981.

Meng, C. -I., and K. Makita, Dynamic variations of the polar cap, in Solar Wind-Magnetosphere Coupling, edited by Y. Kamide and J. A. Slavin, p. 605-631, Terra Scientific, Tokyo, 1986.

Moses, J. J., G. L. Siscoe, N. U. Crooker, and D. J. Gorney, IMF B_y and day-night conductivity effects in the expanding polar cap convection model, J. Geophys. Res., 92, 1193-1198, 1987.

Moses, J. J., G. L. Siscoe, R. A. Heelis, and J. D. Winningham, A model for multiple throat structures in the polar cap flow entry region, J. Geophys. Res., 93, 9785-9790, 1988.

Moses, J. J., G. L. Siscoe, R. A. Heelis, and J. D. Winningham, Polar cap deflation during magnetospheric substorms, J. Geophys. Res., 94, 3785-3789, 1989.

Newell, P. T., and C.-I. Meng, Hemispherical asymmetry in cusp precipitation near solstices, J. Geophys. Res., 93, 2643-2648, 1988.

Nopper, R. W., Jr., and R. L. Carovillano, On the orientation of the polar cap electric field, J. Geophys. Res., 84, 6489-6492, 1979.

Rasmussen C. E., and R. W. Schunk, Ionospheric convection driven by NBZ currents, J. Geophys. Res., 92, 4491-4504, 1987.

Rasmussen, C. E., R. W. Schunk, and V. B. Wickwar, A photochemical equilibrium model for ionospheric conductivity, J. Geophys. Res., 93, 9831-9840, 1988.

Reiff, P. H., J. L. Burch, and R. A. Heelis, Dayside auroral arcs and convection, Geophys. Res. Lett., 5, 391, 1978.

Reiff, P. H., R. W. Spiro, and T. W. Hill, Dependence of polar cap potential drop on interplanetary parameters, J. Geophys. Res., 86, 7639-7648, 1981.

Reiff, P. H., and J. L. Burch, IMF B_y-dependent plasma flow and Birkeland currents in the dayside magnetosphere, 2. A global model for northward and southward IMF, J. Geophys. Res., 90, 1595-1609, 1985.

Reiff, P. H., and J. G. Luhmann, Solar wind control of the polar-cap voltage, in Solar Wind-Magnetosphere Coupling, edited by Y. Kamide and J. A. Slavin, p. 453-476, D. Reidel, 1986.

Rich, F. J., and N. C. Maynard, Consequences of using simple analytical functions for the high-latitude convection electric field, J. Geophys. Res., 94, 3687-3701, 1989.

Robinson, R. M., and R. R. Vondrak, Measurements of E region ionization and conductivity produced by solar illumination at high latitudes, J. Geophys. Res., 89, 3951-3956, 1984.

Robinson, R. M., R. R. Vondrak, and T. A. Potemra, Auroral zone conductivities within the field-aligned current sheets, J. Geophys. Res., 90, 9688-9696, 1985.

Robinson, R. M., R. R. Vondrak, K. Miller, T. Dabbs, and D. A. Hardy, On calculating ionospheric conductivities from the flux and energy of precipitating electrons, J. Geophys. Res., 92, 2565-2569, 1987.

Roble, R. G., E. C. Ridley, A. D. Richmond, and R. E. Dickinson, A coupled thermosphere/ionosphere general circulation model, Geophys. Res. Lett., 15, 1325-1328, 1988.

Russell, C. T., Geophysical coordinate transformations, Cosmic Electrodynamics, 2, 184-196, 1971.

Siscoe, G. L., Polar cap size and potential: a predicted relationship, Geophys. Res. Lett., 9, 672-675, 1982.

Siscoe, G. L., and T. S. Huang, Polar cap inflation and deflation, J. Geophys. Res., 90, 543-547, 1985.

Siscoe, G. L., and N. C. Maynard, Distributed two-dimensional region 1 and region 2 currents: model results and data comparisons, J. Geophys. Res., 96, 21,071-21,085, 1991.

Siscoe, G. L., What determines the size of the auroral oval?, in Auroral Physics, edited by C. -I. Meng, M. J. Rycorft, and L. A. Frank, p. 159-175, Cambridge UP, 1991.

Smiddy, M., W. J. Burke, M. C. Kelley, N. A. Saflekos, M. S. Gussenhoven, D. A. Hardy, and F. J. Rich, Effects of high-latitude conductivity on observed convection electric fields and Birkeland currents, J. Geophys. Res., 85, 6811-6818, 1980.

Sojka, J. J., C. E. Rasmussen, and R. W. Schunk, An interplanetary magnetic field dependent model of the ionospheric convection electric field, J. Geophys. Res., 91, 11,281-11,290, 1986.

Strobel, D. F., C. B. Opal, and R. R. Meier, Photoionization rates in the night-time *E*- and *F*-region ionosphere, Planet. Space Sci., 28, 1027-1033, 1980.

Vickrey, J. F., R. R. Vondrak, and S. J. Matthews, The diurnal and latitudinal variation of auroral zone ionospheric conductivity, J. Geophys. Res., 86, 65-75, 1981.

Wallis, D. D., and E. E. Budzinski, Empirical models of height integrated conductivities, J. Geophys. Res., 86, 125-137, 1981.

Weimer, D. R., N. C. Maynard, W. J. Burke, and C. Liebrecht, Polar cap potentials and the auroral electrojet indices, Planet. Space Sci., 38, 1207-1222, 1990a.

Weimer, D. R., L. A. Reinleitner, J. R. Kan, L. Zhu, and S.-I. Akasofu, Saturation of the auroral electrojet current and the polar cap potential, J. Geophys. Res., 95, 18,981-18,987, 1990b.

Weimer, D. R., J. R. Kan, and S.-I. Akasofu, Variations of the polar cap potential measured during magnetospheric substorms, J. Geophys. Res., 97, 3945-3951, 1992.

Weimer, D. R., Substorm time constants, J. Geophys. Res., in press, 1993.

Wygant, J. R., R. B. Torbert, and F. S. Mozer, Comparison of S3-3 polar cap potential drops with the interplanetary magnetic field and models of magnetopause reconnection, J. Geophys. Res., 88, 5727-5735, 1983.

Yasuhara, F., R. Greenwald, and S.-I. Akasofu, On the rotation of the polar cap potential pattern and associated polar phenomena, J. Geophys. Res., 88, 5773-5777, 1983.